

**NEAR- AND FAR-FIELD THERMAL RADIATION IN  
METAMATERIALS AND THE DEVELOPMENT OF  
*NF-RT-FDTD* ALGORITHM**

A Dissertation

by

Azadeh Didari

Submitted to the  
Graduate School of Sciences and Engineering  
In Partial Fulfilment of the Requirements for  
the Degree of

Doctor of Philosophy

in the  
Department of Electrical and Electronics Engineering

Özyeğin University

June 2016

Copyright© 2016 by Azadeh Didari

**NEAR- AND FAR-FIELD THERMAL RADIATION IN  
METAMATERIALS AND THE DEVELOPMENT OF  
*NF-RT-FDTD* ALGORITHM**

Approved by:

---

Professor M. Pinar Mengüç, Advisor  
Department of Mechanical  
Engineering  
*Özyeğin University*

---

Assoc. Prof. Güray Erkol  
Department of Natural and  
Mathematical Sciences  
*Özyeğin University*

---

Assoc. Prof. Göksenin Yaralıođlu,  
Department of Electrical and  
Electronics Engineering  
*Özyeğin University*

---

Assoc. Prof. Kürşat Şendur,  
Department of Mechatronic  
Engineering  
*Sabancı University*

---

Assoc. Prof. Hakan Ertürk,  
Department of Mechanical  
Engineering  
*Boğaziçi University*

Date Approved: 15 June 2016

# DEDICATION



*To my Mother*

## ABSTRACT

In this dissertation, analysis of near-field regime of thermal radiative transfer in metamaterials supporting surface phonon polaritons (SPhPs) is given. Solutions of electromagnetic fields at subwavelength distances are studied where combined effects of surface waves and total internal reflection, result in enhancement of thermal radiation by orders of magnitude when compared against far-field regime of thermal radiation which is obtainable through Planck's blackbody law. We have developed Near Field Radiative Transfer Finite Difference Time Domain (*NF-RT-FDTD*) algorithm which is developed based on Finite Difference Time Domain (FDTD) method specifically designed to provide full solutions to near-field radiative transfer problems by solving Maxwell's equations combined with fluctuation-dissipation theory. We have extensively investigated the near- and far-field thermal emission and heat flux profiles in different geometries with corrugations and porosities of various size and shapes and report on our findings which reveals a high degree of accuracy is attainable by *NF-RT-FDTD* method in complex geometries. We have compared our results against solutions of effective medium theory which makes effective medium theory's ability to provide accurate solutions highly questionable. *NF-RT-FDTD* could be used to provide solutions for complex geometries with different applications, including energy harvesting with near-field thermophotovoltaics, radiative cooling, thermal sensing, nano manufacturing and medical diagnostics.

## ÖZET

Bu doktora tezinde, yüzey fonon polaritonlarını (SPhP) destekleyen metamalzemeler içerisinde yakın alanda gerçekleşen ışınım ısı transferi incelenmiştir. Işınım ısı transferinde Plank'ın siyah cisim ışınımı ile tanımlanan uzak alan ışınımına kıyasla, yüzey dalgaları (surface waves) ve toplam iç yansımının (total internal reflection) etkileşim etkileri nedeniyle mertebeler ölçüsünde artış gösteren ışınım dalga boyundan daha küçük mesafelerdeki elektromanyetik alanların çözümlenmesi kullanılmıştır. Yakın alan ışınımının çözümlenmesinde; özellikle Maxwell denklemlerinin dalgalanmalı dağılım teorisi (fluctuation dissipation theory) ile birlikte çözümü sonucu elektromanyetik ve ısı çözümleri elde etmeyi mümkün kılacak şekilde tasarlanmış sayısal bir yöntem olan Zaman Ortamında Sonlu Farklar Yöntemi (FDTD) temelli sayısal bir yöntem olarak *NF-RT-FDTD* (Near Field Radiative Transfer Finite Difference Time Domain) algoritması geliştirilmiştir. Çeşitli boyut ve şekillerde oluklar ve gözenekler içeren farklı geometriler için yakın ve uzak alan emisyonu ve ısı akısı profilleri kapsamlı olarak incelenmiş ve bu karmaşık geometrilerin çözümlenmesinde *NF-RT-FDTD* yönteminin kullanımı ile yüksek doğrulukla sonuç elde edilebildiği saptanmıştır. *NF-RT-FDTD* yöntemi ile elde edilen sonuçlar, etkin ortam kuramının (effective medium theory) çözümleri ile karşılaştırılmış ve etkin ortam kuramı ile elde edilen sonuçların tartışmaya açık olduğu belirlenmiştir. Sonuç olarak, *NF-RT-FDTD* yöntemi, yakın alanda termofotovoltaik uygulamalar, ışınımla soğutma, ısı algılama, nano ölçekte üretim ve tıbbi tanılama gibi uygulamalarda kullanılabilecek karmaşık geometriler için sonuçlar elde etmede kullanılabileceği gösterilmiştir.

## ACKNOWLEDGEMENTS

It all started on August 9<sup>th</sup>, 2011 when I received a reply to the email that I had sent asking for an appointment. The email said ‘how about in 20 mints at 3:30?’. Little did I know, that moment was the beginning of my real graduate education and that my life was changed then forever. The earlier days of that summer were not the easiest of days and as I desperately needed to find a PhD supervisor whose research interest would match mine, as the head of Mechanical Engineering Department, Professor Mengüç agreed to send my CV to all the faculty members and see if anyone was willing to take a new PhD student. No one was! and that was exactly the best thing that happened to me! Two weeks later, I was very fortunate to become his PhD student and I have truly enjoyed every minute of the experience ever since. He is an extremely hardworking scientist whose ability in seeing things through to the end is unimaginable. He is always brimming with ideas and is never afraid of new challenges. Whenever I was stuck in my research and feeling discouraged, a trip to his office made all the difference. He would see it all, all the angles, possible approaches and barriers. He is profoundly capable of finding connections between disparate subjects. I would always walk out with more solutions to my problem than I could ever imagine. His ‘*Radiative Heat Transfer*’ course remains my most favorite class of all times. It opened up my eyes to the real science behind my research and that is when I learned to look for the bigger picture, almost always! I learned that I should always set the right boundaries both in computational electromagnetics and in experimental life.

Professor Mengüç is an extraordinary mentor, advisor and friend. The one who has set the bar for my own professional career. For taking me as a student that summer day, salvaging my academic career and turning me in to the researcher I am today, for

supporting me every step of the way, for showing me the right path to walk on, for pushing me to never give up and for believing in me, I will remain grateful to Professor Mengüç forever.

I would like to express my deepest gratitude to Professor Güray Erkol for all the fruitful discussions that we had and also the guidance and support that I received from him when I most needed it. I will always remember them.

This work has not been possible without the support of many people in my life. Words will never be sufficient to express how each and every one of these people has made it possible for me to go on every step of the way.

First, I would like to express my heartfelt gratitude to my dearest friend Hande for befriending me in the first few days that I arrived in Istanbul and then becoming my unbiological sister. Knowing that she exists in my life, has been enough assurance that everything will always be fine! For telling me that “*Life is like a continuous sinusoidal wave and when you are standing on its minima you should know that there will always be a maxima next*”, for being my “*to go to person*”, and for many other things, I can’t possibly thank her enough. She has a special place in my heart.

I am grateful to my friend Hatef for all the help in *probability and statistics* course, for staying up till morning in the library with me so that I would not be alone while working and for all the time and memories we have made together which made life much more fun outside the school.

I am very grateful to my beloved Dilek for making my life brighter with her friendship and for all the practical help that she has given me, all the long discussions that we have had about *life* and for the time we have spent together.

I am grateful to my very kind and supportive friend and colleague Begüm for helping me with the translation of the abstract of the dissertation to Turkish. I could have never done that myself.

I would also like to thank my dear friend Dimitri for many things that I cannot possibly talk about them all. I am a stronger person because of his existence in my life. His guidance and wisdom has walked me through the toughest phases of my life in the past few years. Without him, I would not have been where I am today.

Last but not the least, I would like to thank my very loving family for all these years of support and love and for believing in me even when I doubted myself. I would like to specially thank my mother who has been the strongest woman I know in the world. For being my rock and my friend, for scarifying all the years that we could have spent together for my education and also for everything else that she has done for me, I will forever be indebted to her.

I gratefully acknowledge the reception of financial support for this PhD work by the Scientific and Technological Research Council of Turkey (TUBITAK) under (Grant No. 109M170) and (Grant No.214M308) and also FP-7-PEOPLE-IRG-2008 (Grant No.239382 NF-RAD) at the Center for Energy, Environment and Economy (CEEE) of Özyeğin University, İstanbul, Turkey.

It has been a beautiful fulfilling experience. I look back and smile, the best is yet to come...



# TABLE OF CONTENTS

|  |     |
|--|-----|
| <b>ABSTRACT</b> .....  | iii |
| <b>ÖZET</b> .....  | iv  |
| <b>ACKNOWLEDGEMENTS</b> .....  | v   |
| <b>LIST OF TABLES</b> .....  | xi  |
| <b>LIST OF FIGURES</b> .....   | xii |
| <b>NOMENCLATURE</b> .....  | xvi |
| <b>INTRODUCTION</b> .....  | 1   |
| 1.1 Classical Electromagnetics Theory and Radiative Heat Transfer.....                 | 1   |
| 1.1.1 Litreture Review For Near-Field Thermal Radiation .....                          | 3   |
| 1.1.2 Organization of the Dissertation .....   | 6   |
| <b>FUNDAMENTALS AND FORMULATIONS OF</b> .....  | 9   |
| <b>NEAR-FIELD RADIATIVE TRANSFER</b> .....   | 9   |
| 2.1 Definitions of Surface phonon and plasmon polaritons.....                          | 9   |
| 2.1.1 Polaritons .....   | 9   |
| 2.1.2 Phonons.....   | 9   |
| 2.1.3 Plasmons .....   | 10  |
| 2.1.4 Surface Plasmon/Phonon Polaritons .....  | 10  |
| 2.2 Radiative Heat Transfer in Materials supporting Surface Phonon<br>Polaritons ..... | 11  |
| 2.3 The Maxwell Equations .....  | 13  |

|   |           |
|---|-----------|
| 2.4 FDTD Algorithm For LDOS .....   | 16        |
| 2.4.1 Iterative Algorithm .....   | 16        |
| 2.4.2 Source Implementation .....   | 18        |
| 2.4.3 Numerical Dispersion and Stability .....  | 21        |
| 2.4.4 Boundary Conditions .....   | 21        |
| 2.5 Derivation of LDOS Using the Dyadic Green's Function.....                                   | 23        |
| 2.6 NF-RT-FDTD Algorithm.....   | 27        |
| <b>NEAR-FIELD THERMAL EMISSION IN THIN FILMS .....</b>  | <b>29</b> |
| 3.1 Boundary Conditions .....   | 29        |
| 3.1.1 Boundary Conditions investigation .....   | 30        |
| 3.2 The Permittivity Model.....   | 35        |
| 3.3 Local Density of Electromagnetic States In Thin Films Seperated By<br>Vaccum Nano-gaps..... | 38        |
| 3.4 Dispersion Relation of SPhPs In Thin Films .....  | 40        |
| 3.5 Concluding Remarks.....   | 42        |
| <b>NEAR-FIELD THERMAL EMISSION IN CORRUGATED SURFACES<br/>SEPARATED BY NANO-GAPS.....</b>       | <b>45</b> |
| 4.1 LDOS Profiles in Corrugated Thin Films .....  | 45        |
| 4.2 Heat Flux Profiles in Corrugated Thin Films .....   | 49        |
| 4.3 Concluding Remarks.....   | 51        |

|   |           |
|---|-----------|
| <b>NEAR- TO FAR-FIELD COHERENT THERMAL EMISSION BY CORRUGATED SURFACES AND THE EVALUATION OF EFFECTIVE MEDIUM THEORY.....</b> | <b>53</b> |
| 5.1 Near-To Far-Field LDOS Above a Single Layer and a Corrugated Layer .....  | 55        |
| 5.2 Near-To Far-Field LDOS evaluation by Effective Medium Theory .....  | 57        |
| 5.3 Concluding Remarks.....   | 61        |
| <b>NEAR-FIELD THERMAL RADIATION TRANSFER BY MESOPOROUS METAMATERIALS .....</b>  | <b>62</b> |
| 6.1 Near-Field Thermal Emission in Mesoporous SiC Layers .....  | 63        |
| 6.2 Concluding Remarks.....   | 70        |
| <b>SPECTRALLY SELECTIVE THERMAL EMISSION BY STRUCTURED SiC-BN MESOPOROUS METAMATERIALS.....</b>                               | <b>72</b> |
| 7.1 LDOS in Double Layered Mesoporous SiC-BN Structures .....   | 72        |
| 7.2 Concluding Remarks.....   | 78        |
| <b>EXTENSION OF THE SOLUTION PROCEDURE TO 3D FDTD .....</b>   | <b>79</b> |
| 8.1 The Challenges.....   | 79        |
| 8.2 The Approach.....   | 80        |
| <b>CONCLUSIONS AND FUTURE WORK.....</b>   | <b>82</b> |
| 9.1 Concluding remarks .....  | 82        |
| 9.2 Future Work .....   | 86        |
| <b>BIBLIOGRAPHY .....</b>   | <b>88</b> |

## LIST OF TABLES

|   |    |
|---|----|
| <b>Table 3.1</b> Summary of the optical constants $\omega_{TO}$ and $\omega_{LO}$ , $\epsilon_{\infty}$ and $\Gamma$ of Drude-Lorentz permittivity model for a few materials..... | 37 |
|---|----|



# LIST OF FIGURES

|  |    |
|--|----|
| <b>Figure 1.1</b> Methods of solving near-field thermal radiation problems.....  | 3  |
| <b>Figure 1.2</b> Schematic description of photovoltaics, thermophotovoltaics and near-field thermophotovoltaics.....  | 4  |
| <b>Figure 1.3</b> The geometry: (a) realistic model, (b) Benchmark model, and (c) corrugated thin films model.....   | 7  |
| <b>Figure 2.1:</b> Schematic of the frequency dependent dielectric function $\epsilon(\omega)$ for the frequency range $\omega_{TO} < \omega < \omega_{LO}$ (shaded area) where the surface waves exists. .... | 11 |
| <b>Figure 2.2</b> wave behaviour travelling at the interface between two mediums. ....   | 12 |
| <b>Figure 2.3</b> Ricker wavelet in time. ....   | 20 |
| <b>Figure 2.4</b> Ricker wavelet in frequency. ....  | 20 |
| <b>Figure 2.5.</b> FDTD computational domain with ABCs. ....   | 23 |
| <b>Figure 2.6.</b> Flow-chart for the <i>NF-RT-FDTD algorithm</i> .....  | 28 |
| <b>Figure 3.1.</b> Comparison of LDOS for Mie-Fang +Mur, PML, CPML boundary conditions versus the angular frequency. ....  | 34 |
| <b>Figure 3.2.</b> Comparison of error% for Mie-Fang+Mur, PML, CPML boundary conditions versus the angular frequency. ....   | 34 |
| <b>Figure 3.3</b> Real and Imaginary parts of analytical and FDTD Drude-Lorentz permittivity model. ....   | 36 |
| <b>Figure 3.4</b> Real part of frequency dependent dielectric function for SiC. ....   | 37 |
| <b>Figure 3.5</b> Comparison of FDTD and analytical results of LDOS in vacuum environment. ....  | 38 |
| <b>Figure 3.6</b> LDOS profile for $\Delta = 50$ nm ( $d = 100$ nm), $t_1=100$ nm and $t_3=10$ nm.....   | 39 |

|   |    |
|---|----|
| <b>Figure 3.7</b> LDOS profile for $\Delta = 50$ nm ( $d = 100$ nm), $t_1=100$ nm and $t_3=100$ nm.....   | 39 |
| <b>Figure 3.8</b> The effect of gap size on the LDOS profile.....   | 40 |
| <b>Figure 3.9</b> Dispersion relation of SPhPs for single $t_1 = 100$ and $t_1 = 10$ thick SiC films at the interface with vacuum.....  | 41 |
| <b>Figure 3.10</b> Dispersion relation of SPhPs for $t_1 = 100$ and $t_3 = 10$ thick SiC films in vacuum and separated by a gap 100 nm.....   | 42 |
| <b>Figure 4.1</b> Corrugated Thin Films.....  | 46 |
| <b>Figure 4.2</b> LDOS profile vs. frequency for A, B, C, D configurations.....   | 47 |
| <b>Figure 4.3</b> Enhancement Factor vs Periodicity for SiC elliptic nano-particles.....  | 49 |
| <b>Figure 4.4</b> Near-field heat flux calculation at 300, 600 and 1000 K at presence of elliptic nanoparticles vs the benchmark scenario where no NP are present at the surface of the emitting layer..... | 50 |
| <b>Figure 4.5</b> Enhancement of heat flux at the presence of NPs (over benchmark scenario) vs different shapes of nano-gratings.....   | 51 |
| <b>Figure 5.1(a)</b> Perfectly flat thin SiC film. <b>(b)</b> Spherical NPs placed on the emitting film. ....   | 56 |
| <b>Figure 5.2</b> Comparison of spectral LDOS profiles for the benchmark scenario against corrugated SiC layer.....   | 57 |
| <b>Figure 5.3</b> Comparison of results for LDOS for a single film, in the presence of NPs of diameter of 350 nm and the corresponding EMT. ....  | 58 |
| <b>Figure 5.4</b> Magnified LDOS profile results over near visible spectrum.....  | 59 |
| <b>Figure 5.5</b> Comparison of results found for LDOS for a single film, in the presence of rectangles of $w=h=200$ nm and with EMT.....   | 60 |

|  |    |
|--|----|
| <b>Figure 5.6</b> Comparison of results for radiative flux vs. wavelength for a single film, in the presence of rectangles with $w=h=200$ nm and those based on the EMT. The inset shows an enlarged version of these comparisons for wavelength range of 0.4-0.7 $\mu$ m..... | 60 |
| <b>Figure 6.1</b> Schematics of top view of a typical mesoporous material in which the radius of the pore is $1 \text{ nm} < r < 50 \text{ nm}$ . .....  | 63 |
| <b>Figure 6.2</b> Mesoporous SiC Layers. ....  | 64 |
| <b>Figure 6.3</b> Comparison of LDOS profile for benchmark scenario found through FDTD and EMT analysis for porous SiC emitting layer against corrugated porous emitting layer having $D_{eq}=10$ nm. ....   | 67 |
| <b>Figure 6.4</b> Comparison of normalized LDOS profiles for benchmark scenario for porous SiC emitting layer against corrugated porous emitting layer having $D_{eq}=37$ nm as obtained from the FDTD and the EMT simulations. ....   | 68 |
| <b>Figure 6.5</b> Comparisons of the normalized LDOS profiles for the benchmark case and that for the corrugated porous emitting SiC layer with $D_{eq}=57$ nm as obtained from the FDTD and the EMT simulations. ....   | 69 |
| <b>Figure 6.6</b> Comparison of normalized heat flux profiles for the benchmark case against that for the corrugated porous SiC emitting layer with $D_{eq}=37$ nm. ....   | 69 |
| <b>Figure 6.7</b> Impact of horizontal pore spacing on normalized heat flux profile ( $D_{eq}=37$ nm). ..  | 70 |
| <b>Figure 7.1 a)</b> Perfectly flat thin double-layer film of SiC-BN. <b>b)</b> Porous SiC-BN double-layer film. <b>c)</b> Corrugated porous SiC-BN double-layer composition with SiC NPs. ....  | 74 |
| <b>Figure 7.2</b> Heat flux profile obtained at different observation points above the emitting layer, for benchmark, porous and corrugated porous SiC-BN layers. ....   | 77 |
| <b>Figure 7.3</b> LDOS profile obtained at different observation points above the emitting layer, for benchmark, porous and corrugated porous SiC-BN layers. ....  | 77 |

**Figure 8.1** 3D schematics of corrugated bulk emitting layer separated from a thin non-emitting layer..... 81

**Figure 8.2** 3D schematics of emitting layers with rectangular nanoparticles separated from a thin non-emitting layer..... 81





## NOMENCLATURE

|                      |   |
|----------------------|---|
| $d$                  | spacing between the films, m                                |
| $\mathbf{D}$         | flux density vector, $\text{Cm}^{-2}$                       |
| $\varepsilon$        | electric permittivity, $\text{C}^2\text{N}^{-1}\text{m}$    |
| $\varepsilon_r$      | dielectric constant ( $\varepsilon_r' + i\varepsilon_r''$ ) |
| $\varepsilon_\infty$ | high frequency dielectric constant                          |
| $\mathbf{E}$         | electric field vector, $\text{Vm}^{-1}$                     |
| $\mathbf{H}$         | magnetic field vector, $\text{Am}^{-1}$                     |
| $\mathbb{F}$         | Fourier Transform   |
| $\Gamma$             | damping factor, $\text{rad s}^{-1}$                         |
| $\bar{\mathbf{G}}$   | Green's function tensor, $\text{m}^{-1}$                    |
| $\lambda$            | wavelength, m   |
| $\mu$                | magnetic permeability, $\text{NA}^{-2}$                     |
| $i$                  | complex constant, $(-1)^{1/2}$                              |
| $\rho$               | local density of state                                      |
| $\text{Im}$          | imaginary part  |
| $\Theta$             | mean energy of a Planck oscillator, J                       |
| $\mathbf{J}$         | current density vector, $\text{Am}^{-2}$                    |
| $\omega$             | angular frequency, $\text{rad s}^{-1}$                      |
| $k$                  | wavevector, $\text{rad m}^{-1}$                             |
| $\Delta$             | Where LDOS/Heat flux is calculated                          |
| $q$                  | radiative heat flux, $\text{Wm}^{-2}$                       |
| *                    | complex conjugate   |

|              |                                  |
|--------------|----------------------------------|
| $\mathbf{r}$ | position vector, m               |
| '            | source point                     |
| Re           | real part                        |
| $E$          | electric                         |
| $t$          | time, s or film thickness, m     |
| $H$          | magnetic                         |
| $T$          | temperature, K                   |
| $n$          | time step counter                |
| $v$          | speed of light, $\text{ms}^{-1}$ |
| $v$          | vacuum                           |
| $V$          | volume, $\text{m}^3$             |
| $\omega$     | monochromatic                    |
| $u$          | energy density                   |
| $LO$         | longitudinal optical             |
| $x, y, z$    | Cartesian coordinates            |
| $TO$         | transverse optical               |
| $n$          | complex refractive index         |
| $d_n$        | distance of nanoparticles, m     |
| $h$          | height of nanoparticles, m       |
| $w$          | width of nanoparticles, m        |
| $a_x$        | unit axis in X direction         |
| $a_y$        | unit axis in Y direction         |
| $a_z$        | unit axis in Z direction         |

# CHAPTER I

## INTRODUCTION

### *1.1 Classical Electromagnetics Theory and Radiative Heat Transfer*

The outstanding works of many great scientists such as Weber [1] and Kirchhoff [2] resulted in the understanding that light is indeed an electromagnetic phenomenon by Maxwell [3] and Ampere [4]. These studies built the grounds for understanding that thermal radiation is an electromagnetic phenomenon as well. Stefan [5] and Boltzmann [6] suggested the dependency of the intensity of radiation to temperature. By employing statistical thermodynamics and the Maxwell's radiation pressure, Boltzmann theoretically obtained, the  $T^4$  dependency of the energy density and intensity of radiation from a blackbody at temperature  $T$ . Wien's [7] showed that if the spectral energy density at a certain temperature is given, the spectral energy density for all the other temperatures could as well be obtained. This is now known as displacement law. These studies, built the foundation for Max Planck [8] who in 1900 empirically found Planck's law of blackbody radiation, which correctly gave the spectral distribution of a blackbody radiator  $E_{bb}(\nu, T) = (8\pi\nu^2 / c^3) \times (h\nu / \exp(h\nu / k_B T) - 1)$  over the entire spectral range, at frequency  $\nu$  and temperature  $T$  where  $k_B$  is the Boltzmann constant and  $c$  is the speed of light with  $h = 6.63 \times 10^{-34}$  Kg/s as Planck's constant. In order to explain Planck distribution from quantum optics point of view, one may consider an enclosure at uniform temperature  $T$ . Inside the enclosure, the electromagnetic field can be described by an ensemble of photons [9] forming standing waves with frequency  $\omega$  and energy  $E$  given

by  $E(\omega) = \hbar\omega$ . The spectral mode density  $D(\omega)$  or free space density of states (DOS) of photon states in the enclosure is given by  $D(\omega) = \omega^2 / \pi^2 c^3$ .

Later in 1906, in his seminal book '*The Theory of Heat Radiation (1906)*', Planck presented a clear argument (*"Throughout the following discussion it will be assumed that the linear dimensions of all parts of space considered, as well as the radii of curvature of all surfaces under consideration, are large compared with the wavelengths of the rays considered"*). This clearly states that the dimensions of the surfaces and geometries in the classical approach are always large compared to the primary wavelength of radiation considered in the analysis which is valid for the far-field, at distances several times longer than Wien's wavelength of emission.

While Planck's blackbody model provides an excellent description of the spectral behaviour of far-field thermal radiation, it is incapable of providing the right perception of the near-field regime. When the geometric sizes are less than the thermal wavelength of radiation, a model which takes care of near-field effects is required. In such scenarios, the density of states at the vicinity of a surface becomes much greater than DOS of free space.

This would result in the enhancement of thermal radiation by orders of magnitude at the near-field regime between two media.

The radiative heat transfer between two surfaces can be obtained based on fluctuational electrodynamics which was shown by Rytov in 1953 [10]. In 1971, the first investigation of the radiative heat transfer between arbitrary media based on Fluctuation-Dissipation theorem was made by Polder and Van Hove [11].

### 1.1.1 Literature Review For Near-Field Thermal Radiation

In general, near-field thermal radiation problems could be studied through mathematical analysis, experimental observations and numerical simulations as presented in Figure 1.1.

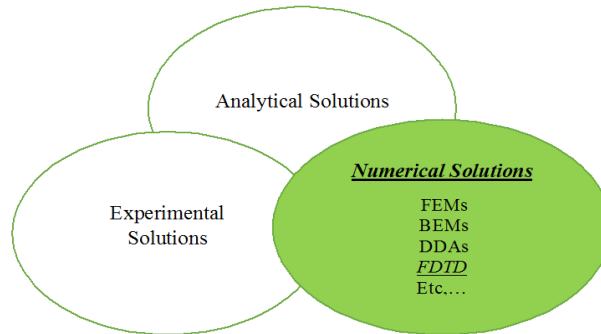


**Figure 1.1** Investigation techniques in near-field thermal radiation.

Over the years, different groups have shown interest in near-field thermal radiation and various theoretical, numerical and experimental works have been done [12-14].

The first experimental investigation on Nano-TPV (NTPVs) power generators was published in 2001 by DiMatteo et al. [15]. Their work provided the potential benefits of radiation tunneling on NTPV devices qualitatively, yet no quantitative data were presented. In 2005, Kittel et al. [16] presented They presented the near-field thermal radiation between a tip and a surface. Their work showed a good agreement with the existing data in the literature.

A schematic description of photovoltaics, thermophotovoltaics and near-field thermophotovoltaics is depicted in Figure 1.2.

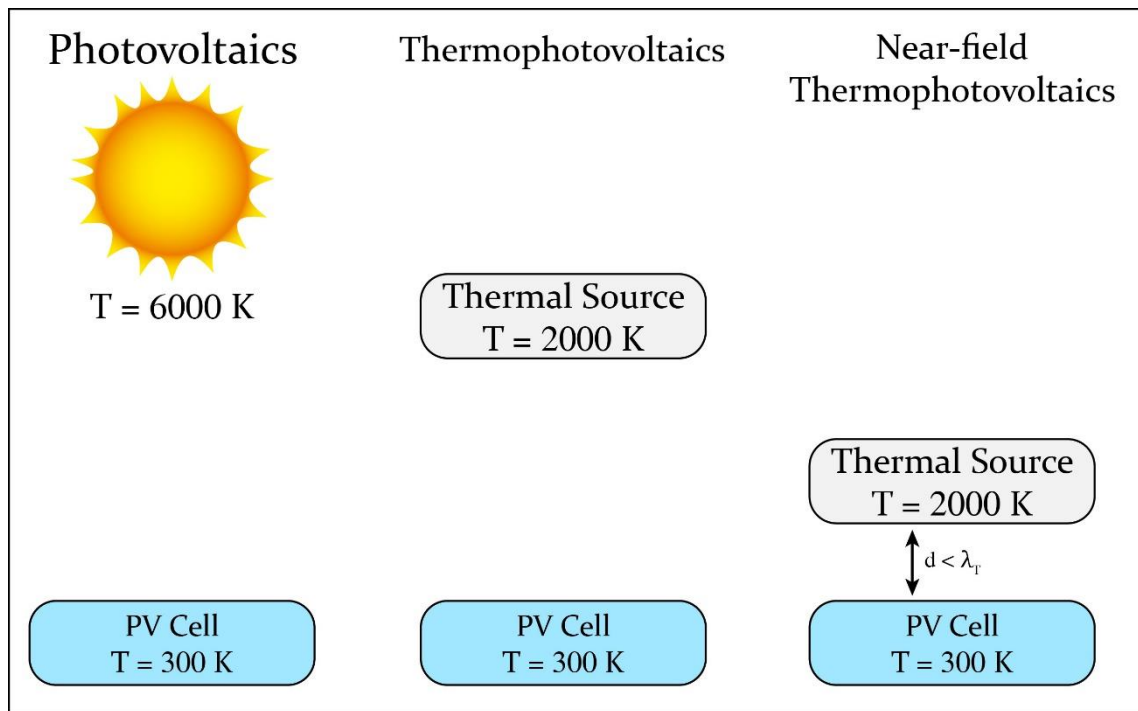


**Figure 1.2** Schematic description of photovoltaics, thermophotovoltaics and near-field thermophotovoltaics.

Hu et al. [17] presented the experimental data for glass to glass plates where the gap was maintained by micron size particles and showed that the heat flux in the small gap between the surfaces could surpass Planck’s far field predictions.

Shen et al. [18] presented experimental observations for a micron size sphere and a flat surface which revealed that surface phonon polaritons (SPhPs) can increase the radiative energy transfer at nanogaps (down to 30 nm). A detailed discussion on these experiments are also reported [19]. Similar experiments were carried out by Gang Chen’s group where experimental analysis for Silica micron-size sphere and a flat surface as well as two parallel surfaces were performed where it was found that radiative heat transfer can enhance the Planck limit in the near-field regime [20]. Additionally, Rousseau et al. [21] provided further experimental evidence of near-field radiative heat transfer between a microsphere and a plate in where the separation gaps varies between 2.5 μm to 30 nm.

The results showed an excellent match with theoretical predictions and they were presented in [22] and [23].

Some of the theoretical analysis of near-field thermal radiation at subwavelength regime has been presented [24-26]. Among these works are some very interesting recent theoretical predictions [24-27] in which the resonant enhancement of the near-field spectral energy density is discussed. However, experimental analysis of the spectral distribution of the electromagnetic thermal near-field are still difficult due to the evanescent nature of the waves in this regime [28-33].

Francoeur et al. [34] presented a model for nano-thermophotovoltaics (nano-TPVs) in which the influence of thermal effects on the performance of these systems were evaluated. They reported on the possibility of tuning near-field thermal emission based on the geometric variations and material properties.

Near field radiation transfer calculations can be carried out using several techniques. One of the most useful tools is the photonic Green's function,  $G(\mathbf{r}, \mathbf{r}'; \omega)$  [35]. The Green's function describes the propagation of energy carriers of angular frequency,  $\omega$ , from the source point  $\mathbf{r}'$ , to the sensor point  $\mathbf{r}$ . It accounts for all possible scattering parameters and depicts the likelihood that a photon will arrive at a particular location from a given excitation source. Green's function is used for calculations of local density of electromagnetic states (LDOS) which is necessary to obtain radiation heat flux in near field thermal radiation related problems.

Advances in nanotechnology and nanophotonics have been inextricably linked with the need and the development of reliable new computational algorithms to be adapted as design tools. These modeling tools are essential for the development of devices and advanced chips towards different applications such as energy harvesting, radiative cooling, nanolithography, nano-scale manufacturing, among others. The required

algorithms are used to quantify the interaction of electromagnetic waves with the matter, and to calculate the required absorption, scattering transmission, and emission profiles of different structures. Among those, we can list Finite Difference Time Domain (FDTD) method [36-39], Finite Element Methods (FEMs) [40,41], Boundary Element Methods (BEMs) [42-45], Transfer Matrix (TM) approach [46], Rigorous Coupled Wave Analysis (RCWA) [47,48], Discrete Dipole Approximations (DDA)[49] and its extensions: Discrete Dipole Approximation-Surface Interactions (DDA-SI) [50] and (DDA-SI-v) [51,52] and also the recent work on surface interaction intergrated implementation of DDA [53] and Thermal Discrete Dipole Approximation (TDDA) [54,55].

### **1.1.2 Organization of the Dissertation**

In this dissertation, we have chosen to adapt the FDTD method for the calculations of near-field radiative transfer problems since one can collect scattering parameters for almost any arbitrary shape geometry with the FDTD approach and obtain a broadband frequency response just with a single run.

Our first objective here is to show that FDTD method is capable of accounting for all the near-field thermal radiation non-equilibrium effects, which are commonly neglected by other methods, when dealing with nano-size geometries whose sizes are less than the wavelength of interest, regardless of the shape of those geometries. We present the Near-Field Radiative Transfer FDTD (*NF-RT-FDTD*) algorithm with the Drude-Lorentz permittivity formulations for materials with negative refractive index (NRI). Figure 1.3 represents (a) a realistic model, (b) a model considered throughout this dissertation as the benchmark model and (c) corrugated emitting and non-emitting thin films separated by a vacuum gap which is a model studied in later Chapters.



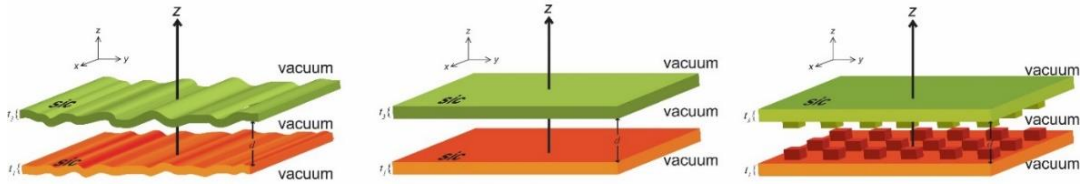


**Figure 1.3** The geometry: (a) realistic model, (b) benchmark model, and (c) corrugated thin films model.

Here we confirm that FDTD can be used for nano-geometries and, inevitably, after reviewing the fundamentals of near-field thermal radiations in Chapter 2, a problem that has a known analytical solution is used intentionally in Chapter 3, in order to provide a reliable point of reference. Throughout this dissertation, thin nano-size films made of metamaterials at different temperatures are separated by a vacuum nano-size gap. The near-field thermal emission (LDOS) and radiation (heat flux) are calculated at different points within the vacuum gap and the outcomes are compared with the analytical solutions for the same problem.

In Chapter 4, corrugated thin films with nano-particles of different sizes, shapes and separation distances (periodicities) are studied and scenarios in which maximum spectral enhancement near-field thermal emission/heat flux could be achieved are discussed.

In Chapter 5, near- to far-field coherent thermal emission by surfaces coated by nanoparticles is investigated and an evaluation of effective medium theory (EMT) is carried out. It is shown that when studying such systems, EMT's predictions could be highly questionable.

In Chapter 6, Near-field thermal radiation transfer by mesoporous metamaterials is studied and the effects of combination of different factors such as nanoparticles and mesopores of different size, shapes and periodicities on enhancement rate of near-field thermal emission and radiation are investigated.

In Chapter 7, Near- to far-field thermal emission and heat flux profiles in a double layer mesoporous metamaterials is studied and the effects of combination of different factors such as nanoparticles and mesopores of different size, shapes and periodicities are investigated.

In Chapter 8, the extension of *NF-RT-FDTD* algorithm to 3D models is discussed and challenges and possible approaches to overcome them are addressed.

In Chapter 9, we present our concluding remarks and thoughts for further developments.



## CHAPTER II

# FUNDAMENTALS AND FORMULATIONS OF NEAR-FIELD RADIATIVE TRANSFER

In this Chapter, we will review the fundamentals of near-field radiative transfer and after establishing the related definitions, we provide the formulations of LDOS and heat flux in the near-field regime which is followed by the formulations of *NF-RT-FDTD* algorithm's step by step development procedure.

### ***2.1 Definitions of Surface phonon and plasmon polaritons***

To establish the fundamentals of near-field radiative transfer, the definitions of polaritons, phonons and plasmons are first given in this section.

#### **2.1.1 Polaritons**

Every coupled state consisting of an elementary excitation of a crystal and an electromagnetic radiation field is called a *polariton* [56]. The existence of polaritons was first predicted by Huang in 1951 in an isotropic diatomic ionic crystal [57-58].

#### **2.1.2 Phonons**

Quantum mechanical principles state that the energy of each lattice wave is discrete and must be a multiple of  $h\nu$  ( $h$  is the Planck constant and  $\nu$  is the frequency of the lattice wave). The minimum energy  $h\nu$  of a quantized lattice wave is called a *phonon* [59].

### 2.1.3 Plasmons

In metals, at optical frequencies the free electrons can sustain surface and volume charge density oscillations which are called *plasmons*.

### 2.1.4 Surface Plasmon/Phonon Polaritons

Surface Polaritons (sometimes called surface waves) are hybrid modes that arise from the coupling of a radiative field and the mechanical vibrations of the lattice within a medium.

Surface waves, which are evanescent waves decaying exponentially, may be categorized into two different classes: Surface waves in metals and those in polar materials. The former are classified as *Surface Plasmon Polaritons (SPP)* which are Surface Polaritons occurring at the interface between a metal and a lossy dielectric. The latter are known as *Surface Phonon Polaritons (SPhP)* and occur at the interface between a polar material and a lossy dielectric.

In this dissertation, the focus of attention is given to Surface Phonon Polaritons. However, Surface Plasmons could also be used in a similar way, usually at higher frequencies but we have not considered them here.

In materials supporting SPhPs, the interaction of light with matter could be described by a frequency-dependent dielectric function  $\varepsilon(\omega)$ . The poles and zeros of  $\varepsilon(\omega)$  correspond to the transverse  $\omega_{TO}$  and longitudinal  $\omega_{LO}$  optical vibrations of the lattice, respectively. It is in the range of  $\omega_{TO} < \omega < \omega_{LO}$  that  $\varepsilon(\omega)$  is negative and it is this region that will be of special interest to us henceforth. In metamaterials, when the permittivity of a material is negative, the surface waves exist at the interface between the material and vacuum. The existence of surface waves results in the resonance of heat transfer around the region where the frequency dependent dielectric function of materials,  $\varepsilon(\omega) \leq 0$ . Later in this Chapter, we will revisit the characteristics of dielectric functions

in different mediums and devote an entire section to detailed discussions on this matter. However, for the time being, we are just presenting the area of interest (shaded area) in materials supporting SPhPs for which the dielectric function is negative as depicted in Figure 2.1.

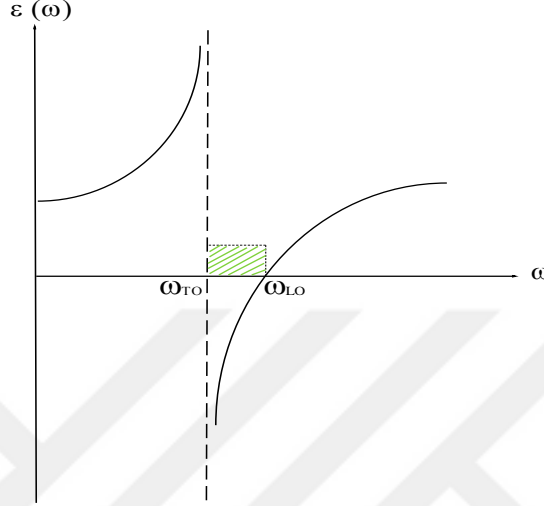


**Figure 2.1:** Schematic of the frequency dependent dielectric function  $\epsilon(\omega)$  for the frequency range  $\omega_{TO} < \omega < \omega_{LO}$  (shaded area) where the surface waves exists.

## ***2.2 Radiative Heat Transfer in Materials supporting Surface Phonon Polaritons***

Radiative heat transfer could be classified in two regimes. The far-field radiative heat transfer exists when propagating waves are the dominant carriers of energy between surfaces separated by gaps greater than Wien's thermal wavelength. The near-field regime of radiative heat transfer occurs between surfaces separated by distances comparable to or shorter than the Wien's wavelength of thermal radiation, which is known to exceed the Planck's law of the blackbody radiation. In this regime, evanescent waves are the dominant energy carriers and they appear due to Total Internal Reflection (TIR) and also due to existence of surface waves. TIR occurs when light travels from a denser medium to a less dense medium. Based on Snell's law if the angle of incidence is

greater than the critical angle, which is the angle of incidence above which the total internal reflection occurs, the light is totally reflected back into the denser medium. Yet, an evanescent wave is created and propagates at the interface between the two mediums, while being confined normal to that interface with the field exponentially decaying in the less dense medium. If another surface is brought close enough to the evanescent wave field of the emitting material, although evanescent waves do not propagate to the far-field, energy transfer through these modes can occur. In the context of surface waves, the waves, which are of evanescent nature travelling along the material–vacuum interfaces can extensively increase the number of available energy states as a results of which near-field radiative heat transfer at nanogaps can be spectrally enhanced.

Figure 2.2 depicts the wave behaviour travelling at the interface between two mediums separated by a vacuum gap (left panel). In the middle panel, total internal reflection occurs and evanescent waves are created. In the right panel, when two surfaces are brought close enough to each other, the evanescent waves can propagate through to the second surface.

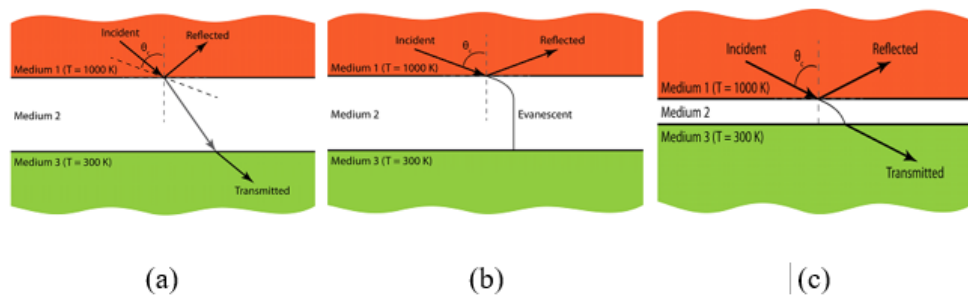


**Figure 2.2** Wave behaviour travelling at the interface between two mediums. (a) the wave behaviour travelling at the interface between two mediums separated by a vacuum gap. (b) when total internal reflection happens and evanescent waves are created. (c) when two surfaces are brought close enough to each other so that the evanescent waves can propagate through the second surface.

Thermal radiation comes from fluctuating dipoles caused by the chaotic motion of electrons and atoms in the emitting medium from which the electromagnetic fields are generated. These fluctuations which could be described by Fluctuation-Dissipation theorem result in the excitation of both propagating and evanescent waves which are the energy carriers between the cold and hot mediums. In order to solve near-field thermal radiation problems, one needs to combine Maxwell's equations and Fluctuation-Dissipation formulations to obtain the full solutions to thermal emission and heat flux at near-field. In the next section, we will give a description of these formulations in more detail.

### ***2.3 The Maxwell Equations***

When a system is changing with respect to time, the governing Maxwell's equations in differential form consist of two curl and two divergence equations as given in Equations (1-4).

$$\nabla \cdot D = \rho_v \quad (1)$$

$$\nabla \cdot B = 0 \quad (2)$$

$$\nabla \times E = -\frac{\partial \bar{B}}{\partial t} \quad (3)$$

$$\nabla \times \bar{H} = \bar{J} + \frac{\partial \bar{D}}{\partial t} \quad (4)$$

For a linear and isotropic (not necessarily homogenous) media,  $\bar{E}$  and  $\bar{D}$  are related by the constitutive relation :  $\bar{D} = \epsilon \bar{E}$  and the constitutive relation for  $\bar{H}$  and  $\bar{B}$  in linear and isotropic media is  $\bar{H} = \frac{1}{\mu} \bar{B}$ .

In Cartesian coordinate systems,  $\nabla \times \bar{E}$  and  $\nabla \times \bar{H}$  are defined as shown in equations (5-6).

$$\nabla \times \bar{E} = \begin{vmatrix} a_x & a_y & a_z \\ \frac{\partial}{\partial x} & \frac{\partial}{\partial y} & \frac{\partial}{\partial z} \\ E_x & E_y & E_z \end{vmatrix} = a_x \left( \frac{\partial E_z}{\partial y} - \frac{\partial E_y}{\partial z} \right) - a_y \left( \frac{\partial E_z}{\partial x} - \frac{\partial E_x}{\partial z} \right) + a_z \left( \frac{\partial E_y}{\partial x} - \frac{\partial E_x}{\partial y} \right) \quad (5)$$

$$\nabla \times \bar{H} = \begin{vmatrix} a_x & a_y & a_z \\ \frac{\partial}{\partial x} & \frac{\partial}{\partial y} & \frac{\partial}{\partial z} \\ H_x & H_y & H_z \end{vmatrix} = a_x \left( \frac{\partial H_z}{\partial y} - \frac{\partial H_y}{\partial z} \right) - a_y \left( \frac{\partial H_z}{\partial x} - \frac{\partial H_x}{\partial z} \right) + a_z \left( \frac{\partial H_y}{\partial x} - \frac{\partial H_x}{\partial y} \right) \quad (6)$$

For a 2D, Transverse Magnetic (TM) wave, the Maxwell's equations in terms of the electrical displacement and magnetic fields  $D_x$ ,  $D_z$  and  $H_y$  are given as (7-11) in which the only non-zero component of magnetic field is  $H_y$ , i.e. propagation along the  $z$  axis.

$$\frac{\partial D_x}{\partial t} = -\frac{\partial H_y}{\partial z} \quad (7)$$

$$\frac{\partial D_z}{\partial t} = \frac{\partial H_y}{\partial x} \quad (8)$$

The collective effect of all the dipoles of free electrons would generate a macroscopic polarization defined as  $P(\omega) = \varepsilon_0 \chi_e(\omega) E(\omega)$  in which  $\varepsilon_0$  is the dielectric constant of vacuum,  $\chi_e(\omega)$  is the electric susceptibility which is a dimensionless proportionality constant that indicates the degree of polarization of a dielectric material in response to an applied electric field and  $E(\omega)$  is the electric field. The electrical displacement  $D(\omega) = \varepsilon_0 E(\omega) + P(\omega)$ , from which we derive  $D(\omega) = \varepsilon_0 \varepsilon_r(\omega) E(\omega)$  and  $\varepsilon_r(\omega) = 1 + \chi_e(\omega)$  where  $\varepsilon_r(\omega)$  is the relative permittivity of the dielectric function.

$$D_x(\omega) = \varepsilon_0 \varepsilon_r(\omega) E_x(\omega) \quad (9)$$

$$D_z(\omega) = \varepsilon_0 \varepsilon_r(\omega) E_z(\omega) \quad (10)$$



$$\frac{\partial H_y}{\partial t} = \frac{1}{\mu_0} \left( \frac{\partial E_z}{\partial x} - \frac{\partial E_x}{\partial z} \right) \quad (11)$$

In the  $xz$  plane of interest, the one-dimensional wave equation could be written as:

$$\left( \frac{\partial}{\partial x} - \frac{1}{v} \frac{\partial}{\partial t} \right) E_z = 0 \quad (12.a)$$

$$\left( \frac{\partial}{\partial z} - \frac{1}{v} \frac{\partial}{\partial t} \right) E_x = 0 \quad (12.b)$$

In order to solve near-field thermal radiation problems, we use FDTD method to obtain solutions of Maxwell's equations. The FDTD method is a full-wave technique used to solve electromagnetic problems. It was first proposed by Kane Yee in 1966 and it employs second-order central differences method [6]. He proposed “spatially staggering the vector components of the E-field and H-field about unit cells of a Cartesian computational grid so that each E-field vector component is located midway between a pair of H-field vector components, and vice versa”. After the results of Maxwell's equations are obtained, a combination of FDT and stochastic Maxwell's equations gives us the required information to study the near-field thermal radiation [60]. The equations can be easily discretized using only the field components on, or just inside the mesh wall, yielding an explicit finite difference equation as illustrated below at time step  $n + 1$ .

$$E_{z_{1,k+1/2}}^{n+1} = E_{z_{2,k+1/2}}^n + \frac{v\Delta t - \Delta x}{v\Delta t + \Delta x} (E_{z_{2,k+1/2}}^{n+1} - E_{z_{1,k+1/2}}^n) \quad (13.a)$$

$$E_{x_{i+1/2,1}}^{n+1} = E_{x_{i+1/2,2}}^n + \frac{v\Delta t - \Delta z}{v\Delta t + \Delta z} (E_{x_{i+1/2,2}}^{n+1} - E_{x_{i+1/2,1}}^n) \quad (13.b)$$

where  $E_{z_{i,k+1/2}}^n$  and  $E_{x_{i+1/2,k}}^n$  respectively refer to the  $i$ ,  $k^{th}$  electric component of Yee cell [60,61] in  $z$  and  $x$  direction. Throughout this work, it is assumed that the geometries are homogeneous, isotropic, nonmagnetic, and described by a frequency-dependent dielectric function given by Drude-Lorentz permittivity model, given as in [62]

$$\varepsilon_r(\omega) = \varepsilon_\infty \frac{\omega^2 - \omega_{LO}^2 + i\Gamma\omega}{\omega^2 - \omega_{TO}^2 + i\Gamma\omega} \quad (14)$$

where for silicon carbide  $\varepsilon_\infty = 6.7$ ,  $\omega_{LO} = 1.825 \times 10^{14}$  rad/s,  $\omega_{TO} = 1.494 \times 10^{14}$  rad/s, and  $\Gamma = 8.966 \times 10^{11}$  rad/s. As SiC displays a negative Real  $\varepsilon_r(\omega)$  between its transverse  $\omega_{TO}$  and longitudinal  $\omega_{LO}$  optical phonon resonance frequencies, we focus on this frequency range for the simulations. The numerical algorithm for Maxwell's curl equations requires that the time increment  $\Delta t$  have a specific bound relative to the space increments  $\Delta x$ ,  $\Delta y$  and  $\Delta z$ . The time increment has to obey the following bound, known as Courant-Freidrichs-Lewy (CFL) stability criterion [36] is given as

$$\Delta t \leq \min \left\{ \left( c \sqrt{\frac{1}{(\Delta x)^2} + \frac{1}{(\Delta y)^2} + \frac{1}{(\Delta z)^2}} \right)^{-1} \right\} \quad (15)$$

## 2.4 FDTD Algorithm For LDOS

In this Chapter, we highlight the FDTD algorithm used for the solution of the LDOS formulation as well as both the frequency and the time domain implementation of Drude-Lorentz permittivity model. In order to obtain the required Green's function tensor, we introduce the source of excitation after taking all aspects of the FDTD method discussed above into consideration.

### 2.4.1 Iterative Algorithm

The first order finite difference representation of fields in. Eqs. (1), (2) and (5) is written in discrete time domain as

$$\frac{D_{x_{i+1/2,k}}^{n+1/2} - D_{x_{i+1/2,k}}^{n-1/2}}{\Delta t} = - \frac{H_{y_{i+1/2,k+1/2}}^n - H_{y_{i+1/2,k-1/2}}^n}{\Delta z} \quad (16)$$

$$\frac{D_{z_{i,k+1/2}}^{n+1/2} - D_{z_{i,k+1/2}}^{n-1/2}}{\Delta t} = -\frac{H_{y_{i+1/2,k+1/2}}^n - H_{y_{i-1/2,k+1/2}}^n}{\Delta x} \quad (17)$$

$$\frac{H_{y_{i+1/2,k+1/2}}^{n+1} - H_{y_{i+1/2,k+1/2}}^n}{\Delta t} = \frac{E_{z_{i+1,k+1/2}}^{n+1/2} - E_{z_{i,k+1/2}}^{n+1/2}}{\mu_0 \Delta x} - \frac{E_{x_{i+1/2,k+1}}^{n+1/2} - E_{x_{i+1/2,k}}^{n+1/2}}{\mu_0 \Delta z} \quad (18)$$

It is worth mentioning that if the Yee cell size is kept small, the central differences are said to have second-order accuracy or second-order behavior ( $\Delta x^2$  terms can be ignored) [8]. Furthermore, we can re-write Eqs. (16), (17), and (18) as

$$D_{x_{i+1/2,k}}^{n+1/2}(k) = D_{x_{i+1/2,k}}^{n-1/2}(k) - \frac{\Delta t}{\Delta z} \left[ H_{y_{i+1/2,k+1/2}}^n - H_{y_{i+1/2,k-1/2}}^n \right] \quad (19)$$

$$D_{z_{i,k+1/2}}^{n+1/2}(k) = D_{z_{i,k+1/2}}^{n-1/2}(k) - \frac{\Delta t}{\Delta x} \left[ H_{y_{i+1/2,k+1/2}}^n - H_{y_{i-1/2,k+1/2}}^n \right] \quad (20)$$

$$H_{y_{i+1/2,k+1/2}}^{n+1} = H_{y_{i+1/2,k+1/2}}^n + \frac{\Delta t}{\mu_0 \Delta x} \left[ E_{z_{i+1,k+1/2}}^{n+1/2} - E_{z_{i,k+1/2}}^{n+1/2} \right] - \frac{\Delta t}{\mu_0 \Delta z} \left[ E_{x_{i+1/2,k+1}}^{n+1/2} - E_{x_{i+1/2,k}}^{n+1/2} \right] \quad (21)$$

which is the iterative algorithm of computing the fields in FDTD method. In Eq. (21), the electric field for the cells inside the vacuum gap is found by  $E_x^n = D_x^n / \varepsilon_0$ . For the SiC layers with relative electric permittivity of  $\varepsilon_r(\omega)$  we need to obtain the discrete time domain representation of the Drude-Lorentz permittivity model [62]. By replacing Eq. (8) in Eq. (3) we have

$$D_x(\omega) = \varepsilon_0 \varepsilon_\infty \frac{\omega^2 - \omega_{LO}^2 + i\Gamma\omega}{\omega^2 - \omega_{TO}^2 + i\Gamma\omega} E_x(\omega) \quad (22)$$

which can be simplified as

$$D_x(\omega) = \varepsilon_0 \varepsilon_\infty E_x(\omega) + \varepsilon_0 \varepsilon_\infty \frac{\omega_{TO}^2 - \omega_{LO}^2}{\omega^2 - \omega_{TO}^2 + i\Gamma\omega} E_x(\omega) \quad (23)$$

Let us further define

$$S(\omega) = \varepsilon_0 \varepsilon_\infty \frac{\omega_{TO}^2 - \omega_{LO}^2}{\omega^2 - \omega_{TO}^2 + i\Gamma\omega} E_x(\omega) \quad (24)$$

By using properties of inverse Fourier transforms, an equivalent recursive expression of Eq. (24) in the time domain can be obtained as

$$S^n = 2e^{-\alpha\Delta t} \cos(\beta\Delta t) S^{n-1} - e^{-2\alpha\Delta t} S^{n-2} + Ae^{-\alpha\Delta t} \sin(\beta\Delta t) E_x^{n-1} \quad (25)$$

where  $\alpha = \Gamma/2$ ,  $\beta = \sqrt{\omega_{TO}^2 - \Gamma^2/4}$ , and  $A = \varepsilon_0 \varepsilon_\infty (\omega_{LO}^2 - \omega_{TO}^2) / \sqrt{\omega_{TO}^2 - \Gamma^2/4}$ .

Considering Eqs. (23) and (24),  $E_x^n$  can be found using  $D_x^n$  and  $S^n$  given by

$E_x^n = (D_x^n - S^n) / \varepsilon_0 \varepsilon_\infty$ . The other component of electric field,  $E_z^n$ , can be found similarly.

## 2.4.2 Source Implementation

In order to find the Green's function tensor, we excite the system by a unit dipole source at location  $\mathbf{r}'$ , i.e.  $\mathbf{J}(\mathbf{r}, \omega) = \mathbf{J}(\omega) \delta(\mathbf{r} - \mathbf{r}')$  where  $\mathbf{J}$  is the current density. Modeling a source of excitation that would cover a wide band of frequency with a single run and would function as a Dirac delta function, was found to be a particularly challenging task. Generally, FDTD technique is not used to model DC fields, which are due to charges that stand in the grid. At a grid point, where charges exist, the average of the electric field over time is non-zero. Since we apply the excitation at a grid by varying the electric field, if the average of excitation is non-zero (i.e. DC component), it introduces a non-physical artifact in the form of a charge, located in the grid and influencing the simulation. We found that although using a pulsed source (Gaussian pulse) rather than a harmonic one seemed to be an appropriate choice of excitation, its DC component was likely to introduce artifacts which are not physical. In order to be able to both benefit from having a pulsed source and at the same time not to have to deal with the complications that a DC component brings into our computational solutions, we decided to use another pulsed

source, called the Ricker wavelet [64] which is the second derivative of the Gaussian pulse. This has no DC component and allows us to set its most energetic frequency to whatever desired frequency or grid discretization we choose. The formulation for the Ricker wavelet is as follows

$$f_r(t) = \left(1 - 2\{\pi f_p [t - d_r]\}^2\right) \exp\left(-\{\pi f_p [t - d_r]\}^2\right) \quad (26)$$

where  $f_p$  is the peak frequency (highest energy),  $d_r$  is the temporal delay and is defined as  $d_r = M_d / f_p$ , and  $M_d$  is the delay multiplier. The Ricker wavelet showed a great impact on the calculated fields, helping to establish a path to determine the right LDOS profile. We apply the source to the system and we observe the field components. By taking the Fourier transform of the fields, a component of the Green function tensor is obtained in (21) where,  $i, j \in \{X, Y, Z\}$ .

$$G_{ij}^E(\mathbf{r}, \mathbf{r}', \omega) = \frac{E_i(\mathbf{r}, \omega)}{J_j(\omega)} = \frac{\mathbb{F}[E_i(\mathbf{r}, t)]}{\mathbb{F}[J_j(t)]} \quad (27)$$

Where  $\mathbb{F}$  indicates the Fourier transform. By applying the excitation source in all three directions of  $X$ ,  $Y$ ,  $Z$  and computing the electric and magnetic fields in a specific point, all components of the Green tensor function are present, which later will be used in calculation of LDOS.

In Figure 2.3 and 2.4, Ricker wavelet in time and frequency are depicted respectively.

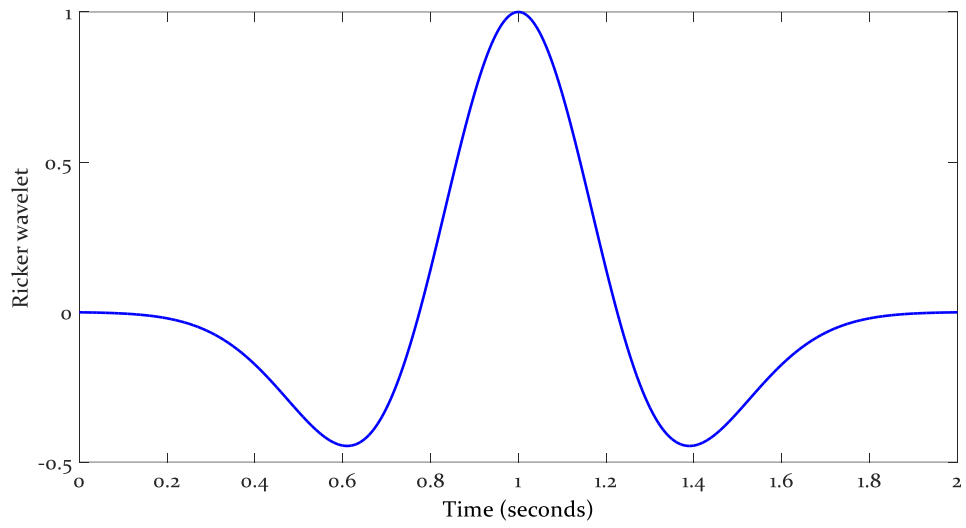


**Figure 2.3** Ricker wavelet in time.

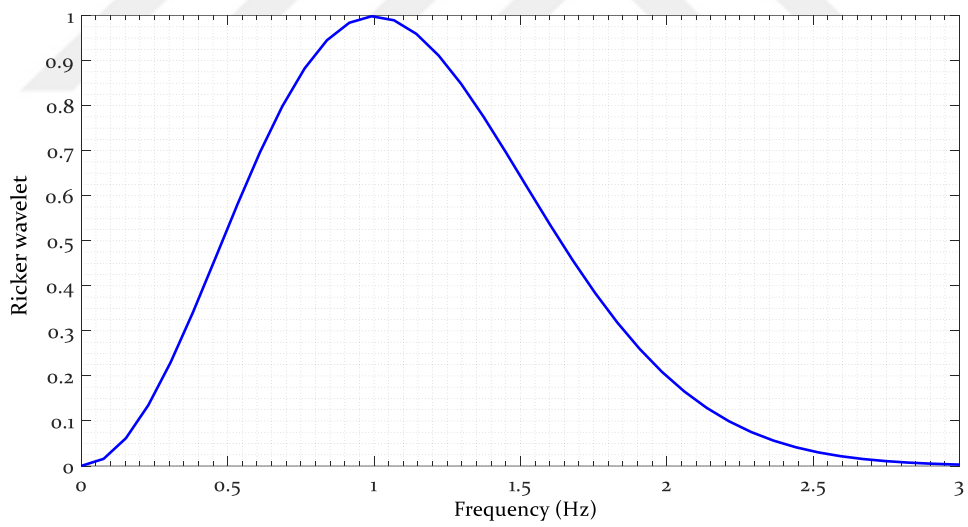


**Figure 2.4** Ricker wavelet in frequency.

### 2.4.3 Numerical Dispersion and Stability

In the numerical solution of any differential equations, numerical dispersion is always a cause of concern and should be minimized or, better still, eliminated. In order to minimize the possible numerical dispersion in a FDTD analysis, the size of each cell is required to be at least ten times smaller than the shortest wavelength of propagation [8]. The numerical dispersion could be reduced even more if the size of the cell would be chosen even smaller than the abovementioned limit. However using a cell size which is too small increases the number of cells that are needed to fill the computational domain and hence makes the problem computationally very expensive. The numerical dispersion associated with our numerical method of choice obligates us to have  $\Delta z \leq \lambda_{\min} / 10$ . Considering  $\lambda = \lambda_0 / n$ , where  $\lambda_0$  is the wavelength of vacuum and  $n$  is the refractive index equivalent to the real part of the  $\sqrt{\varepsilon_r(\omega)}$ , the smallest wavelength was found to be  $2.17 \times 10^{-6}$   $\mu\text{m}$ , which is larger than the model geometry itself.

### 2.4.4 Boundary Conditions

FDTD simulations must be carried out within a finite volume of space terminated with definite boundary conditions. Setting the boundary conditions in a correct and efficient way is essential in the success of FDTD algorithms. The reason for this is that the computational domain is always finite, yet the wave propagation to be considered continues beyond the bounds of the computational domain. To attenuate the reflection of energy back into the computational grid, we need to choose the right boundary conditions. Perfectly Matched Layer (PML) which was originally proposed by J.-P. Berenger in 1994, is rather an artificial absorbing medium than an absorbing boundary condition, which is widely used to truncate computational domains for simulating wave

propagations, and is designed to make sure that no additional reflections exist in the medium of interest [63]. PML is generally considered the state-of-the-art for the termination of FDTD grids. However, when a PML is implemented in FDTD, there are almost always some reflections back to the medium. Berenger proposed technique consists of splitting each field component into two individual parts and the actual field components are the sum of these two parts. In this way, by splitting the field, Berenger could create an anisotropic medium with the required phase velocity and conductivity to remove reflections at the interface between a PML and non-PML region. In the works that were followed later by others, they have proposed PML based techniques using different approaches such as the complex coordinate-stretching technique put forward by Chew and Weedon, also in 1994 [66]. Possibly, the best PML formulation is the Convolutional-PML (CPML). A CPML is the PML formed from an anisotropic, dispersive material and it does not require the fields to be split; therefore, it can be implemented in a relatively straightforward manner and it also said to make the simulations faster. For this reasons, we have employed the CPML method when developing *NF-RT-FDTD* algorithm which is proved to provide optimum elimination of unwanted reflections when working with NFRT problems. The details of investigation of boundary conditions is given in the next Chapter. Figure 2.5 shows the schematic of the computational domain of the geometry considered throughout this dissertation.



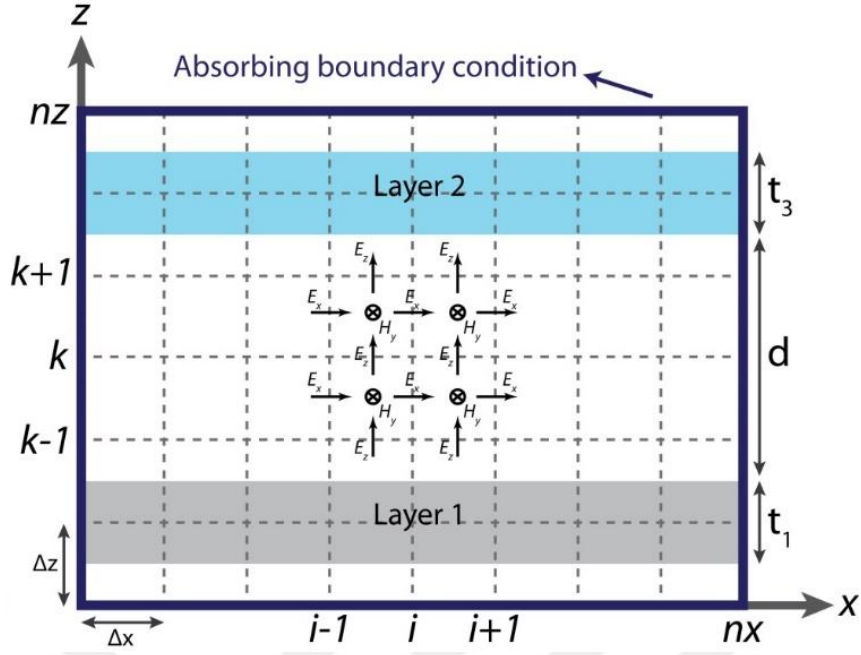


**Figure 2.5.** FDTD computational domain with Absorbing Boundary Conditions (ABCs).

## 2.5 Derivation of LDOS Using the Dyadic Green's Function

Below, the formula of LDOS is derived based on the Green's tensor function. Using the method of potentials, the electric and magnetic fields can be expressed as in [62]

$$\mathbf{E}(\mathbf{r}, \omega) = i\omega\mu_0 \int_{V'} dV' \overline{\overline{\mathbf{G}}^E}(\mathbf{r}, \mathbf{r}', \omega) \mathbf{J}^r(\mathbf{r}', \omega) \quad (28)$$

$$\mathbf{H}(\mathbf{r}, \omega) = \int_{V'} dV' \overline{\overline{\mathbf{G}}^H}(\mathbf{r}, \mathbf{r}', \omega) \mathbf{J}^r(\mathbf{r}', \omega) \quad (29)$$

where  $\overline{\overline{\mathbf{G}}^E}(\mathbf{r}, \mathbf{r}', \omega)$  and  $\overline{\overline{\mathbf{G}}^H}(\mathbf{r}, \mathbf{r}', \omega)$  are the electric and magnetic Green tensors given

by

$$\overline{\overline{\mathbf{G}}^E} = \begin{pmatrix} G_{XX}^E & G_{XY}^E & G_{XZ}^E \\ G_{YX}^E & G_{YY}^E & G_{YZ}^E \\ G_{ZX}^E & G_{ZY}^E & G_{ZZ}^E \end{pmatrix} \quad \text{and} \quad \overline{\overline{\mathbf{G}}^H} = \begin{pmatrix} G_{XX}^H & G_{XY}^H & G_{XZ}^H \\ G_{YX}^H & G_{YY}^H & G_{YZ}^H \\ G_{ZX}^H & G_{ZY}^H & G_{ZZ}^H \end{pmatrix} \quad (30)$$

In Eqs. (28) and (29),  $\mathbf{J}^r$  is a random fluctuating variable defined as  $\mathbf{J}^r = [J_X^r \ J_Y^r \ J_Z^r]^T$  where  $[\cdot]^T$  denote the transpose of the vector. The components of electric and magnetic fields in Cartesian coordinates are given by

$$E_j = i\omega\mu_0 \int_{V'} dV' (G_{jX}^E J_X^r + G_{jY}^E J_Y^r + G_{jZ}^E J_Z^r) = i\omega\mu_0 \int_{V'} dV' \mathbf{G}_j^E \mathbf{J}^r \quad (31.a)$$

$$H_j = \int_{V'} dV' (G_{jX}^H J_X^r + G_{jY}^H J_Y^r + G_{jZ}^H J_Z^r) = \int_{V'} dV' \mathbf{G}_j^H \mathbf{J}^r \quad (31.b)$$

where  $j \in \{X, Y, Z\}$ . The energy density is calculated as the sum of the electric and magnetic energies given by

$$\langle \mathbf{u}_\omega(\mathbf{r}, \omega, T) \rangle = 4 \times \frac{1}{4} \left[ \varepsilon_0 \langle |\mathbf{E}(\mathbf{r}, \omega)|^2 \rangle + \mu_0 \langle |\mathbf{H}(\mathbf{r}, \omega)|^2 \rangle \right] \quad (32)$$

In Eq. (32),  $\langle |\mathbf{E}(\mathbf{r}, \omega)|^2 \rangle$  and  $\langle |\mathbf{H}(\mathbf{r}, \omega)|^2 \rangle$  in terms of their components can be written as

$$\langle |\mathbf{E}(\mathbf{r}, \omega)|^2 \rangle = \langle E_X E_X^* \rangle + \langle E_Y E_Y^* \rangle + \langle E_Z E_Z^* \rangle \quad (33.a)$$

$$\langle |\mathbf{H}(\mathbf{r}, \omega)|^2 \rangle = \langle H_X H_X^* \rangle + \langle H_Y H_Y^* \rangle + \langle H_Z H_Z^* \rangle \quad (33.b)$$

where  $E_x^*$  denotes complex conjugate of  $E_x$ . In the following discussion, we explain the derivation of  $\langle E_X E_X^* \rangle$  only. By applying the same methodology, the other terms can also be found. By replacing Eq. (31.a) in  $\langle E_X E_X^* \rangle$ , it can be written as

$$\begin{aligned} \langle E_X E_X^* \rangle &= \left\langle \left( i\omega\mu_0 \int_{V'} dV' \mathbf{G}_X^E(\mathbf{r}, \mathbf{r}', \omega) \mathbf{J}^r(\mathbf{r}', \omega) \right) \left( -i\omega\mu_0 \int_{V''} dV'' \mathbf{J}^{r*}(\mathbf{r}', \omega) \mathbf{G}_X^{E*}(\mathbf{r}, \mathbf{r}'', \omega) \right) \right\rangle \\ &= \omega^2 \mu_0^2 \int_{V'} dV' \int_{V''} dV'' \mathbf{G}_X^E(\mathbf{r}, \mathbf{r}', \omega) \langle \mathbf{J}^r(\mathbf{r}', \omega) \mathbf{J}^{r*}(\mathbf{r}'', \omega) \rangle \mathbf{G}_X^{E*}(\mathbf{r}, \mathbf{r}'', \omega) \end{aligned} \quad (34)$$

Note that in Eq. (34),  $\mathbf{J}^r(\mathbf{r}', \omega) \mathbf{J}^{r*}(\mathbf{r}'', \omega)$  is a 3-by-3 matrix and

$\mathbf{G}_X^E(\mathbf{r}, \mathbf{r}', \omega) = \begin{bmatrix} \mathbf{G}_{XX}^E & \mathbf{G}_{XY}^E & \mathbf{G}_{XZ}^E \end{bmatrix}$ . According to fluctuation-dissipation theorem (FDT), we have

$$\langle J_\alpha^r(\mathbf{r}', \omega) J_\beta^{r*}(\mathbf{r}'', \omega') \rangle = \frac{\omega \varepsilon_0 \varepsilon_r''(\omega)}{\pi} \Theta(\omega, T) \delta(\mathbf{r}' - \mathbf{r}'') \delta(\omega - \omega') \delta_{\alpha\beta} \quad (35)$$

where the subscripts  $\alpha$  and  $\beta$  refer to orthogonal components (i.e.  $X, Y, Z$ ) indicating the state of polarization of the source and  $\delta_{\alpha\beta}$  accounts for the assumption of isotropic media.  $\varepsilon_r''(\omega)$  is the imaginary part of the relative permittivity of the emitting layer. The term  $\Theta(\omega, T)$  is the mean energy of a Planck oscillator in thermal equilibrium at frequency  $\omega$  and temperature  $T$  given as

$$\Theta(\omega, T) = \frac{\hbar \omega}{\exp(\hbar \omega / k_b T) - 1} \quad (36)$$

Going back to Eq. (34) and using FDT in Eq. (34),  $\langle \mathbf{J}^r(\mathbf{r}', \omega) \mathbf{J}^{r*}(\mathbf{r}'', \omega) \rangle$  would be obtained as

$$\langle \mathbf{J}^r(\mathbf{r}', \omega) \mathbf{J}^{r*}(\mathbf{r}'', \omega) \rangle = \frac{\omega \varepsilon_0 \varepsilon_r''(\omega)}{\pi} \Theta(\omega, T) \delta(\mathbf{r}' - \mathbf{r}'') \mathbf{I}_3 \quad (37)$$

where  $\mathbf{I}_3$  is 3-by-3 unitary matrix. By replacing Eq. (31) in Eq. (34), it will be simplified as

$$\begin{aligned} \langle E_X E_X^* \rangle &= \frac{\omega^3 \mu_0^2 \varepsilon_0 \varepsilon_r''(\omega)}{\pi} \Theta(\omega, T) \int_{V'} dV' \mathbf{G}_X^E(\mathbf{r}, \mathbf{r}', \omega) \mathbf{G}_X^{E*}(\mathbf{r}, \mathbf{r}', \omega) \\ &= \frac{\omega^3 \mu_0^2 \varepsilon_0 \varepsilon_r''(\omega)}{\pi} \Theta(\omega, T) \int_{V'} dV' \left( |G_{XX}^E|^2 + |G_{XY}^E|^2 + |G_{XZ}^E|^2 \right) \end{aligned} \quad (38)$$

Likewise,  $\langle E_Y E_Y^* \rangle$  and  $\langle E_Z E_Z^* \rangle$  can be found in the same way and  $\langle |\mathbf{E}(\mathbf{r}, \omega)|^2 \rangle$  is given by

$$\langle |\mathbf{E}(\mathbf{r}, \omega)|^2 \rangle = \frac{\omega^3 \mu_0^2 \varepsilon_0 \varepsilon_r''(\omega)}{\pi} \Theta(\omega, T) \int_{V'} dV' \begin{pmatrix} |G_{XX}^E|^2 + |G_{XY}^E|^2 + |G_{XZ}^E|^2 \\ + |G_{YX}^E|^2 + |G_{YY}^E|^2 + |G_{YZ}^E|^2 \\ + |G_{ZX}^E|^2 + |G_{ZY}^E|^2 + |G_{ZZ}^E|^2 \end{pmatrix} \quad (39)$$

In the same manner,  $\langle |\mathbf{H}(\mathbf{r}, \omega)|^2 \rangle$  is given by

$$\langle |\mathbf{H}(\mathbf{r}, \omega)|^2 \rangle = \frac{\omega \varepsilon_0 \varepsilon_r''(\omega)}{\pi} \Theta(\omega, T) \int_{V'} dV' \begin{pmatrix} |G_{XX}^H|^2 + |G_{XY}^H|^2 + |G_{XZ}^H|^2 \\ + |G_{YX}^H|^2 + |G_{YY}^H|^2 + |G_{YZ}^H|^2 \\ + |G_{ZX}^H|^2 + |G_{ZY}^H|^2 + |G_{ZZ}^H|^2 \end{pmatrix} \quad (40)$$

The LDOS,  $\rho_\omega(\mathbf{r})$ , in the near-field is calculated by dividing the energy density in Eq. (26) by  $\Theta(\omega, T)$ , i.e.,

$$\rho_\omega(\mathbf{r}) = \frac{\langle \mathbf{u}_\omega(\mathbf{r}, \omega, T) \rangle}{\Theta(\omega, T)} = \frac{\varepsilon_0 \langle |\mathbf{E}(\mathbf{r}, \omega)|^2 \rangle + \mu_0 \langle |\mathbf{H}(\mathbf{r}, \omega)|^2 \rangle}{\Theta(\omega, T)} \quad (41)$$

Replacing Eqs. (36) and (37) in Eq. (38) and defining  $k_v = \omega / c_0$  ( $c_0$  light speed) as the magnitude of the wave vector in vacuum, LDOS can be found as

$$\rho_\omega(\mathbf{r}) = \frac{\omega \varepsilon_r''(\omega)}{\pi c_0^2} \left\{ k_v^2 \int_{V'} dV' \begin{pmatrix} |G_{XX}^E|^2 + |G_{XY}^E|^2 + |G_{XZ}^E|^2 \\ + |G_{YX}^E|^2 + |G_{YY}^E|^2 + |G_{YZ}^E|^2 \\ + |G_{ZX}^E|^2 + |G_{ZY}^E|^2 + |G_{ZZ}^E|^2 \end{pmatrix} + \int_{V'} dV' \begin{pmatrix} |G_{XX}^H|^2 + |G_{XY}^H|^2 + |G_{XZ}^H|^2 \\ + |G_{YX}^H|^2 + |G_{YY}^H|^2 + |G_{YZ}^H|^2 \\ + |G_{ZX}^H|^2 + |G_{ZY}^H|^2 + |G_{ZZ}^H|^2 \end{pmatrix} \right\} \quad (42)$$

Calculation of the TM evanescent component of monochromatic LDOS can be found through the following expression

$$\rho_\omega(\mathbf{r}) = \frac{\omega \varepsilon_r''(\omega)}{\pi c_0^2} \left\{ k_v^2 \int_{V'} dV' \left( |G_{XX}^E|^2 + |G_{XZ}^E|^2 + |G_{ZX}^E|^2 + |G_{ZZ}^E|^2 \right) + \int_{V'} dV' \left( |G_{YX}^H|^2 + |G_{YZ}^H|^2 \right) \right\} \quad (43)$$

Note that this expression is given in the literature for the first time. Green's function tensor will be computed using FDTD algorithm and by replacing it in Eq. (43) LDOS can be calculated. The monochromatic radiative heat flux along the z-direction also is given in terms of Green's function tensor as [62]

$$q_\omega(\mathbf{r}) = \frac{2k_0^2 \Theta(\omega, T)}{\pi} \operatorname{Re} \left\{ i \varepsilon_r''(\omega) \int_{V'} dV' \begin{bmatrix} G_{XX}^E G_{YX}^{H*} - G_{YX}^E G_{XX}^{H*} \\ G_{XY}^E G_{YY}^{H*} - G_{YY}^E G_{XY}^{H*} \\ G_{XZ}^E G_{YZ}^{H*} - G_{YZ}^E G_{XZ}^{H*} \end{bmatrix} \right\} \quad (44)$$

where for TM-polarized waves, the monochromatic radiative heat flux will be simplified as

$$q_\omega(\mathbf{r}) = \frac{2k_0^2 \Theta(\omega, T)}{\pi} \operatorname{Re} \left\{ i \varepsilon_r''(\omega) \int_{V'} dV' \left[ G_{XX}^E G_{YX}^{H*} + G_{XZ}^E G_{YZ}^{H*} \right] \right\} \quad (45)$$

## 2.6 NF-RT-FDTD Algorithm

The structure depicted in Figure 2.6 describes the general approach to solving near-field thermal emission and heat flux for any arbitrary geometry. It consists of four main steps. In the first step (initialization of the problem) the geometry properties such as grid size, optical constants of the material for the chosen permittivity model and frequency range are defined. In the second step (discretization), the specifications of the boundary condition are defined. Then, the source of excitation is defined. The inverse Fourier transform of the permittivity model is obtained and the electric and magnetic fields are discretized in time and space. In the third step (the combination of Maxwell's equations and fluctuation dissipation theorem) the Green's functions of electric and magnetic fields are evaluated and FDT is found. In step four (finalization) LDOS and heat flux are

determined based the Green's functions and the program checks to see if the fields are solved for the entire duration, if they are then the algorithm is finalised. Otherwise, it continues.

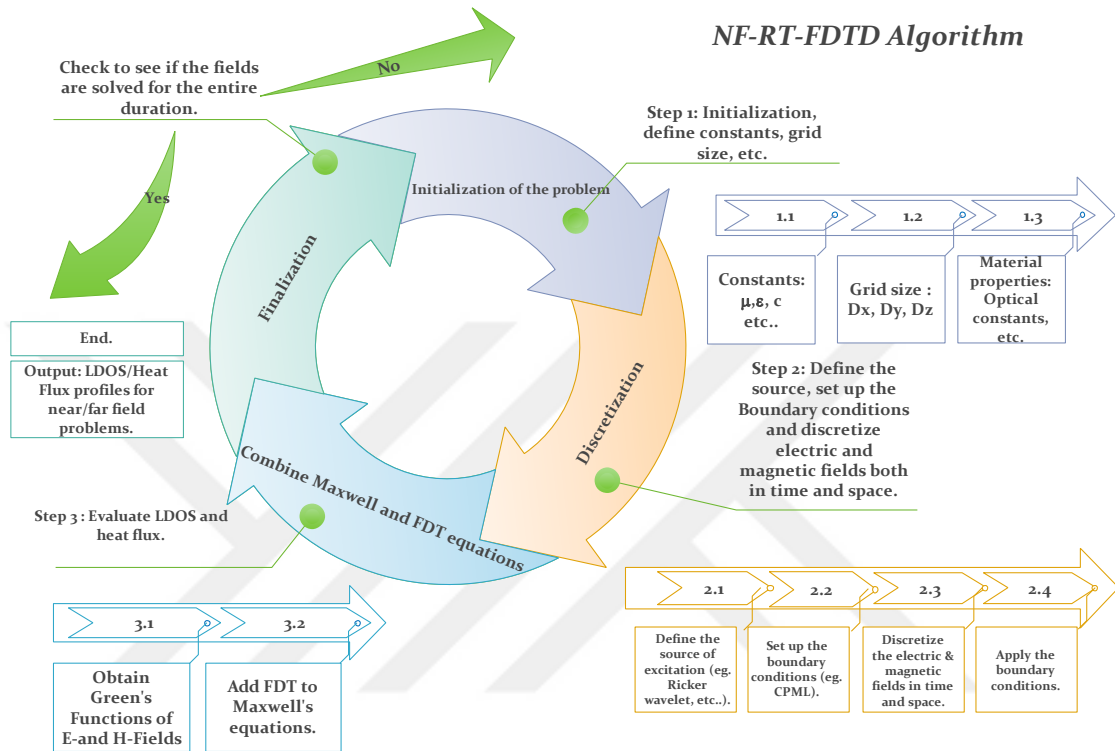


**Figure 2.6.** Structure of the *NF-RT-FDTD algorithm*.

## CHAPTER III

### NEAR-FIELD THERMAL EMISSION IN THIN FILMS

In this section, the details of investigations of the most suitable boundary conditions in near-field radiative transfer problems are given and followed by the comparison of the different boundary conditions. Next, the results for the benchmark model for which an analytical solution is available are given. This problem was chosen to test the capability of *NF-RT-FDTD* algorithm in providing accurate results. In the following Chapters, we will extend this problem to more complex ones.

Some of the contents of this Chapter were published in the *Journal of Quantitative Spectroscopy and Radiative Transfer* in 2014 [87].

#### ***3.1 Boundary Conditions***

As stated in Chapter 2, we chose to work with FDTD because of its well documented advantages for computational electrodynamics [36]. Through FDTD calculations, which can incorporate the effects of reflection and emission (which are commonly neglected by other methods), modelling wave propagation in complex media, such as time-varying, anisotropic, lossy, dispersive and non-linear media is possible. However, FDTD simulations suffer from high memory requirements and simulation time. In order to reduce the memory requirements, one solution is to reduce the number of grid cells in the geometry by selecting the right boundary conditions such that absorption of the unwanted reflections from the boundary walls, which terminate the computational domain would not require the layers of boundary conditions to be placed far away from the domain of physical interest. Setting the boundary conditions in a correct and efficient way is

essential in the success of FDTD methods. The reason for this is that the computational domain is finite but wave propagation can continue beyond the bounds of this domain. To attenuate the reflection of energy back into the computational grid, we need to consider some form of Absorbing Boundary Condition (ABC) which has the effect of simulating infinite or open boundary geometry.

In the early stages of this work, we explored different ABCs such as Mur's first order boundary condition [65], combined with Mei-Fang's 'superabsorption' method [66], Perfectly Matched Layer (PML) [67] and Convolutional PML. We will review these investigations in the next section.

### 3.1.1 Investigation of Boundary Conditions

One typical geometry for our problem is an emitting Silicon Carbide (SiC) film with a thickness of 100 nm, separated by a vacuum gap of 100 nm from a non-emitting SiC film of 10 nm thickness. We calculate thermal emission in the angular frequency range of  $1.5 \times 10^{14} - 1.9 \times 10^{14}$  rad/s within which the resonance frequency of the SiC occurs. In this system, we set  $\Delta x = 60$  nm,  $\Delta z = 2$  nm with  $n_x = 101$  grids in the  $X$  direction and  $n_z = 206$  grids in the  $Z$  direction. We chose to neglect variations in the  $Y$  direction since this is a symmetric 2D TM case.

By taking into consideration that  $\Delta z$  is much smaller than  $\Delta x$ , then the Courant criteria in Equation (15) could be met if we choose  $\Delta t = S_c \Delta z / c_0$ , where the Courant factor,  $S_c = 1/\sqrt{2}$ . With the configuration mentioned above,  $\Delta t$  is found to be  $4.717 \times 10^{-18}$  sec. Furthermore, based on the Nyquist theorem which states that at least two samples per wave period are needed to define a periodic wave, the maximum frequency of the system is given by  $f_{\max} = 1/(2 \times \Delta t) \approx 10^{17}$  Hz. Moreover, if we choose to have, say, 150 frequency 'buckets' for our spectral analysis, we calculate the frequency



resolution  $\Delta f$  as  $\Delta f = (1.9 \times 10^{14} / 2\pi - 1.4 \times 10^{14} / 2\pi) / 150 = 4.25 \times 10^{10}$  Hz. The number of iterations then can be found from  $N = 2f_{\max} / \Delta f$  where the required number of time steps is approximately  $5 \times 10^6$  which can make the FDTD simulation computationally expensive if the number of grids is large. This fact results in a tradeoff between high accuracy (larger number of grids) and computational expense. Here the choice of right ABC plays an important role in increasing the accuracy but not the number of grids.

We outline below the steps that need to be taken to identify the right boundary conditions when considering geometries that are smaller than the wavelengths of interest. In this case, the dominant waves are strictly evanescent and their exponential decay will require several wavelengths before their energy content becomes negligible. Consequently, they will reach the edges of the computational grid before they have decayed enough not to cause significant reflections back into the grid. For these reasons, it is necessary to take the penetration depth of evanescent waves, which is a measure of how deep evanescent waves travel into vacuum, into consideration. Evanescent waves are due to both the Total Internal Reflection (TIR) and SPhPs of SiC.

When considering open boundary problems using a computational method such as FDTD, the computational space is finite and needs to be truncated by the right boundary conditions. In 1981, Mur formulated the Absorbing Boundary Conditions (ABCs) for the FDTD approximations of the time-domain electromagnetic-field equations [65]. Mur's first order ABC is a good absorber for normally incident waves travelling at a single speed, however when a wave is propagating through a dispersive medium, where the relative permittivity is frequency-dependent for a range of frequencies, the wave is associated with a range of velocities. Under these conditions, the medium is no longer as good an absorber as it was initially.

We initially used Mur's first order ABCs in our problem, having to work with evanescent waves. We found out that for Mur's first order ABCs to act as good absorbers of evanescent waves we needed to make them sufficiently distant from the computational domain of interest. Placing the ABCs at a far distance from the problem domain so that the evanescent waves would fully decay before reaching the boundaries, the geometry had to be made much larger in both the  $X$  and  $Z$  directions. This would make the problem computationally very expensive. Considering the long penetration depth, we concluded that this ABC was not a good choice of boundary conditions for this problem.

In 1988 and 1992, Mie and Fang [66] developed a super-absorbing algorithm in which they apply a boundary condition to both  $E$  and  $H$  fields at the boundaries. We applied this method to our problem and have seen improvements in the results, which are depicted in Figure 3.1; yet, these improvements were not deemed satisfactory.

In 1994, Berenger [67] proposed another boundary condition, called the Perfectly Matched Layer (PML) technique to be used with Maxwell's equations; it is widely recognized that PML, in its various formulations, provides a superior and extremely robust absorbing boundary condition. However, in the nano-scale geometries for which emission and heat flux are to be computed, the attenuation of evanescent waves is not dealt adequately with PML since PML cannot effectively absorb evanescent waves. As a result, PML must be placed sufficiently far away from the geometry so that the evanescent waves would propagate and significantly decay. This would result in an increase in the required number of cells, memory and time in a FDTD simulation. A form of the PML which is referred to as the Complex Frequency Shifted PML (CFS-PML) was developed in 1996 by Kuzuoglu and Mittra [68]. It was shown that the CFS-PML was highly effective at absorbing evanescent waves and signals with a long time signature. A modified implementation of the CFS-PML was introduced in 1998 by Gedney [69]. This

method is known as Convolutional-PML (CPML). It is faster than the original PML method and the implementation is efficient and powerful in the sense that it will absorb waves in isotropic and homogeneous media, as well as in inhomogeneous, lossy, dispersive, anisotropic or non-linear media. Furthermore, for general media, the number of additional unknowns that are required for the CPML formulation is the same as in the most effective techniques proposed for the original split-field and uniaxial PML expressions. Hence, given the fact that this method can significantly absorb evanescent waves, great memory savings can be achieved by placing the absorbing layers much closer to the computational domain.

The FDTD results for LDOS calculations with PML boundary conditions are presented in Figure 3.1. They depict considerable improvement in comparison with the Mie-Fang super-absorption boundary condition. As it is clearly seen, CPML boundary condition gives us the closest FDTD results of LDOS profile when compared with the analytical solution.

In Figure 3.2, we have shown the error calculations when different boundary conditions were applied to the medium and the FDTD and analytical solutions were compared. The results show that the maximum error (around 90%) occurs around angular resonance frequency at  $\omega_{res} = 1.786 \times 10^{14}$  rad/s and when Mur's first order ABC is combined with Mie-Fang ABC. The error is reduced to 60% for PML boundary conditions. The minimum error (around 10%) is found for the CPML boundary conditions. The 80% reduction of error through using CPML boundary conditions makes CPML the best candidate for absorbing boundary conditions when considering near-field calculations in dispersive and inhomogeneous nano-scale geometries. We expect that the error could be reduced even more, by using a combination of appropriate Graphics Processing Units (GPUs) and multiple CPU cores which would allow finer gridding

without making the problem extremely expensive. At this stage of the work the required simulation time varies between 2-6 hours depending on the specifications of the computer that users work with.

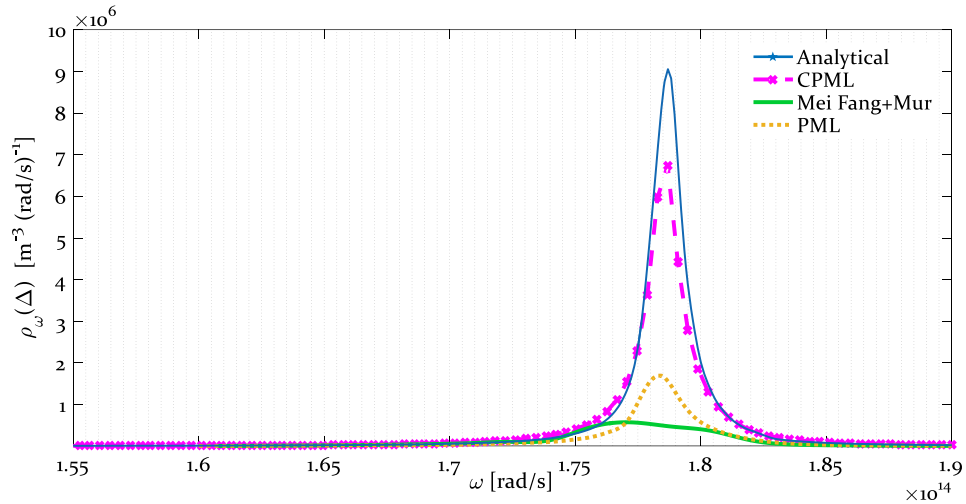


**Figure 3.1.** Comparison of LDOS for Mie-Fang +Mur, PML, CPML boundary conditions versus the angular frequency.

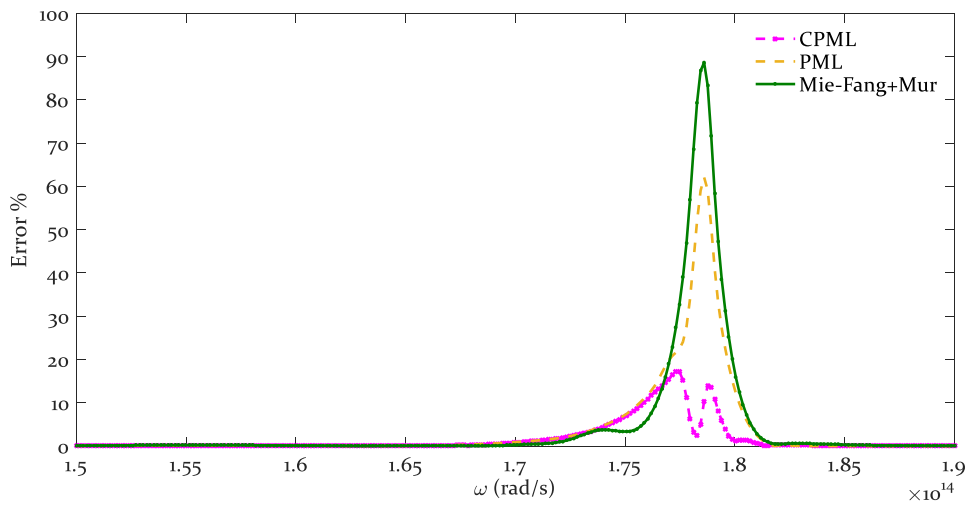


**Figure 3.2.** Comparison of error% for Mie-Fang+Mur, PML, CPML boundary conditions versus the angular frequency.

### 3.2 The Permittivity Model

The next challenging problem in FDTD modeling is the permittivity model whose derivation has been earlier carried out in the time domain. It should be understood that the FDTD method is a time domain based method while a permittivity model such as Drude-Lorentz permittivity is frequency based. In order to simulate the permittivity model since there is no known time domain function we would need to use an appropriate approximation for this purpose. We have used a time domain equivalent recursive expression as given in Eq. (25) in which a large enough number of iterations needs to be considered in order to reduce both the numerical error and at the same time prevent the simulations from becoming very costly. In order to increase the accuracy of Drude-Lorentz approximation, a mesh size refinement could be used in order to take care of convergence of the solutions and it would also reduce the simulation time, hence making it a less expensive approach. Adaptive Mesh Refinement (AMR) [70] technique could be used in order to reduce the mesh size in layers where we have the utmost sensitivity to the Drude-Lorentz permittivity model especially at the borders of the layers where there is discontinuity.

In Figure 3.3, a comparison between the analytical formulation of Drude-Lorentz permittivity model in Eq. (14) and its computational results based on Eq. (25) is calculated in the considered range of frequency of  $1.5 \times 10^{14}$  to  $1.9 \times 10^{14}$  rad/s. The optical constants for silicon carbide are given as  $\epsilon_{\infty} = 6.7$ ,  $\omega_{LO} = 1.825 \times 10^{14}$  rad/s,  $\omega_{TO} = 1.494 \times 10^{14}$  rad/s and  $\Gamma = 8.966 \times 10^{11}$  rad/s. As SiC displays a negative Real  $\epsilon_r(\omega)$  between its transverse  $\omega_{TO}$  and longitudinal  $\omega_{LO}$  optical phonon resonance frequencies, we focus on this frequency range for the simulations. Both the real and

imaginary parts of  $\epsilon_r(\omega)$  are depicted in the Figure 3.3 where a good agreement between the results of FDTD analysis and analytical solutions could be observed.

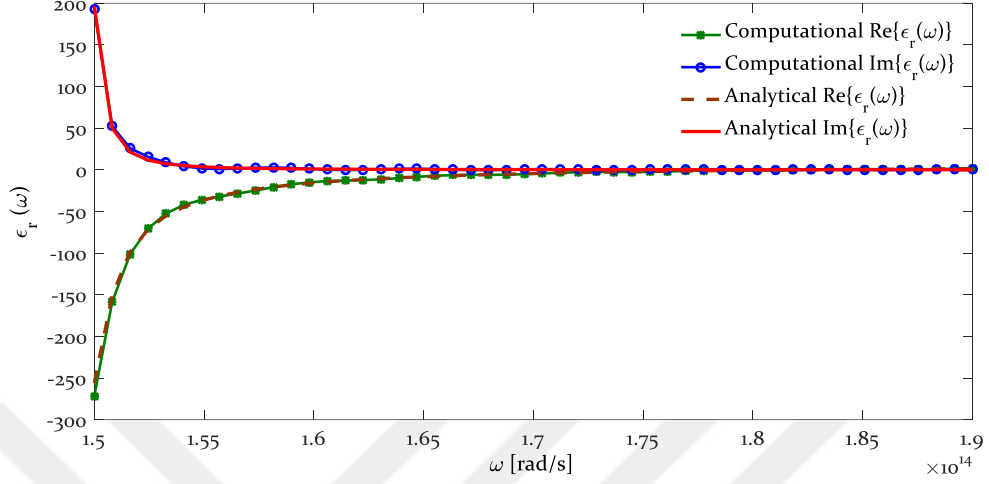


**Figure 3.3** Real and Imaginary parts of analytical and FDTD Drude-Lorentz permittivity model.

Between the poles and zeros of the dielectric function which correspond to  $\omega_{TO}$  and  $\omega_{LO}$ , respectively, the real part of the permittivity model reaches the value of  $\epsilon(\omega) = -1$  at the interface of the material and vacuum and remains less than -1 in that range. When  $\epsilon(\omega) = -1$ , the resonance frequency of the SPhPs occurs and in that range between  $\omega_{TO}$  and  $\omega_{LO}$ , the surface waves exist, which have an evanescent nature. This is the region of interest in the near-field thermal radiation transfer. The contribution of the SPhPs at far-field is of very little and almost ignorable significance. However, in this region, they contribute significantly to the enhancement of near-field thermal radiation. In the case of a material like SiC, there exists only one atom per unit cell in its crystal and hence the dielectric function has only one pole. In case of crystals with more atoms per unit cells, number of poles of the dielectric function is increased accordingly and so is the number of surface polariton branches. The resonance frequency of SPhPs can be

calculated as  $\omega_{res} = \sqrt{(\epsilon_{\infty}\omega_{LO}^2 + \omega_{TO}^2)/(1 + \epsilon_{\infty})}$ . By introducing  $\epsilon_{\infty}$ , the permittivity model takes care of high frequency dielectric constant caused by the system of valence electrons which is measured in the visible and NIR spectral range [71]. Figure 3.4 depicts the real part of the frequency dependent permittivity function of SiC, where  $\omega_{TO}$  and  $\omega_{LO}$ , resonance frequency as well as the region of interest are presented.

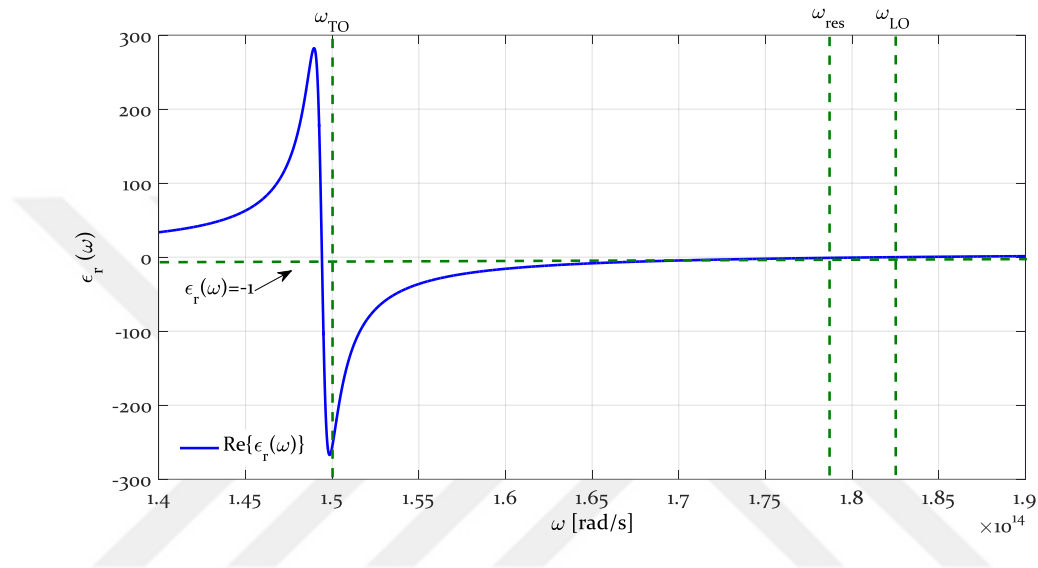


**Figure 3.4** Real part of frequency dependent dielectric function for SiC.

**Table 3.1** summarises the optical constants  $\omega_{TO}$  and  $\omega_{LO}$ ,  $\epsilon_{\infty}$  and  $\Gamma$  of Drude-Lorentz permittivity model for a few materials.

|                  | $\omega_{TO}$ (rad/s)  | $\omega_{LO}$ (rad/s)  | $\Gamma$ (rad/s)       | $\epsilon_{\infty}$ |
|------------------|------------------------|------------------------|------------------------|---------------------|
| SiC              | $1.494 \times 10^{14}$ | $1.825 \times 10^{14}$ | $8.966 \times 10^{11}$ | 6.7                 |
| cBN              | $1.985 \times 10^{14}$ | $2.451 \times 10^{14}$ | $6.241 \times 10^{12}$ | 4.46                |
| hBN <sup>1</sup> | $2.575 \times 10^{14}$ | $3.032 \times 10^{14}$ | $1.001 \times 10^{12}$ | 4.88                |
| hBN <sup>2</sup> | $2.844 \times 10^{14}$ | $3.005 \times 10^{14}$ | $1.507 \times 10^{13}$ | 3.9                 |
| GaN              | $106 \times 10^{12}$   | $141 \times 10^{12}$   | $1.52 \times 10^{12}$  | 5.35                |
| BC               | $2.054 \times 10^{14}$ | $2.976 \times 10^{14}$ | n/a                    | n/a                 |

<sup>1</sup> Electric Field is perpendicular to the optical axis.

<sup>2</sup> Electric Field is parallel to the optical axis.

n/a Not available

### 3.3 Local Density of Electromagnetic States In Thin Films Separated By Vacuum Nano-gaps

In Figure 3.5, analytically obtained LDOS are compared against FDTD analysis of LDOS, obtained within a vacuum space in the absence of the silicon carbide layers. Analytical formulation of LDOS within a vacuum is given as  $\rho_{\omega} = \omega^2 / (\pi^2 c_0^3)$  [14]. The results were obtained at 100 nm above the excitation point. For the case of vacuum, perfect match between the results is observed. The numerical dispersion and stability have been satisfied by assuming  $\Delta x = \Delta y = \Delta z = 1$  nm and  $\Delta t = 2 \times 10^{-18}$  seconds in the vacuum environment.

In Figures 3.6 and 3.7, the LDOS is calculated in the vacuum gap at distance  $\Delta$  above the emitting layer with presence of a non-emitting layer. Outcomes are compared with the analytical results. The near-field thermal radiation is strongly dependent on  $\Delta$  (the local point where the results are observed at),  $d$  (gap between the films), and thicknesses of the films. To analyze the influence of thickness of the layers on the LDOS, we study the cases of  $\Delta = 50$  nm ( $d = 100$  nm),  $t_1 = 100$  nm and  $t_3 = 10$  nm and compare it with the case where  $t_1 = 100$  nm and  $t_3 = 100$  nm.

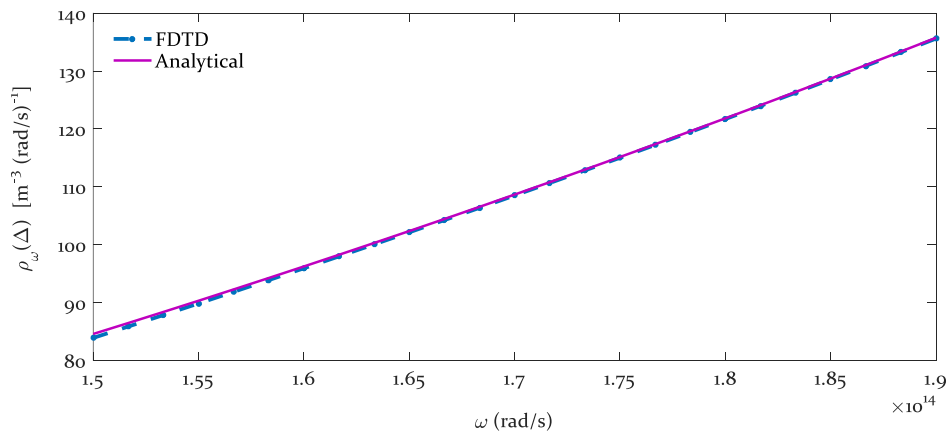


**Figure 3.5** Comparison of FDTD and analytical results of LDOS in vacuum environment.



Comparison of Figures 3.6 and 3.7 shows the impact of an increase in the thickness of the non-emitting layer from 10 nm to 100 nm which results in an increase in the magnitude of LDOS value around  $\omega_{res}$ . It is worth mentioning that the presence of the non-emitting layer starts to modify the LDOS values when the thickness of the non-emitting layer  $t_3 > (d/2)$  as discussed in [72].

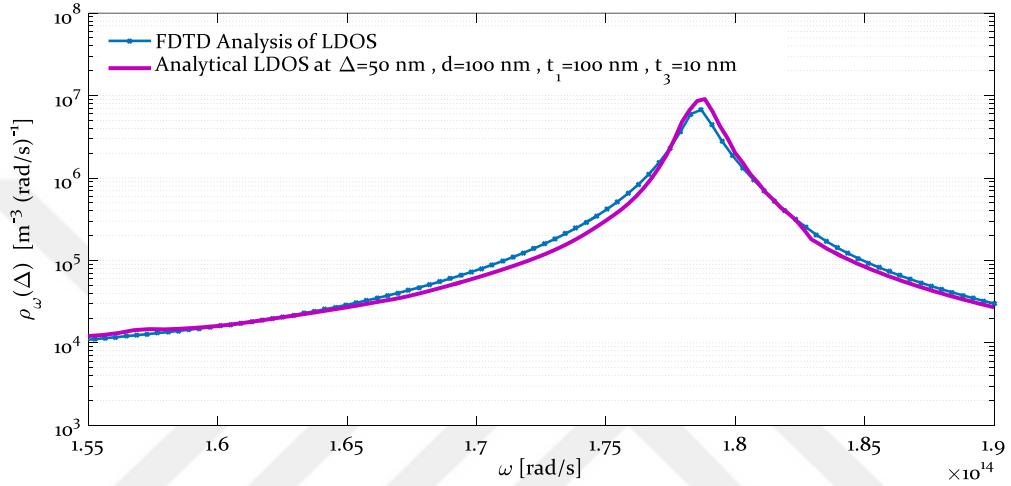


**Figure 3.6** LDOS profile for  $\Delta = 50$  nm ( $d = 100$  nm),  $t_1 = 100$  nm and  $t_3 = 10$  nm.

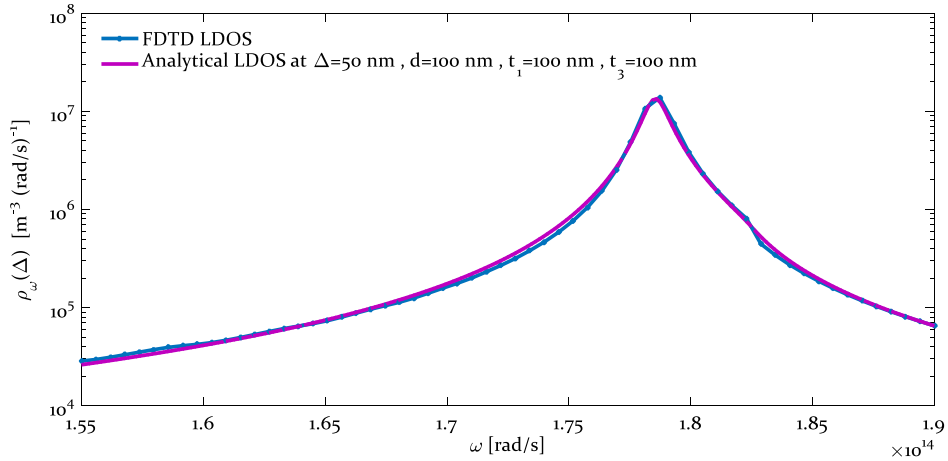


**Figure 3.7** LDOS profile for  $\Delta = 50$  nm ( $d = 100$  nm),  $t_1 = 100$  nm and  $t_3 = 100$  nm.

Next, we analyzed the effect of gap size,  $d$ , on LDOS behaviour. For this purpose, we study the case of  $\Delta = 50$ ,  $d = 500$  nm. It is shown that in the case of  $d$  increasing from 100 to 500 nm, surface phonon polariton coupling between the films decreases and consequently the enhancement of LDOS around  $\omega_{res}$ , decreases. Further more, if we increase the distance from 500 nm to 1000 nm, we see a clear decrease of three orders of magnitude in the LDOS and even an increase in the thickness of the layers would no longer be able to make up for the falloff of the LDOS values. The results of this study is depicted in Figure 3.8.

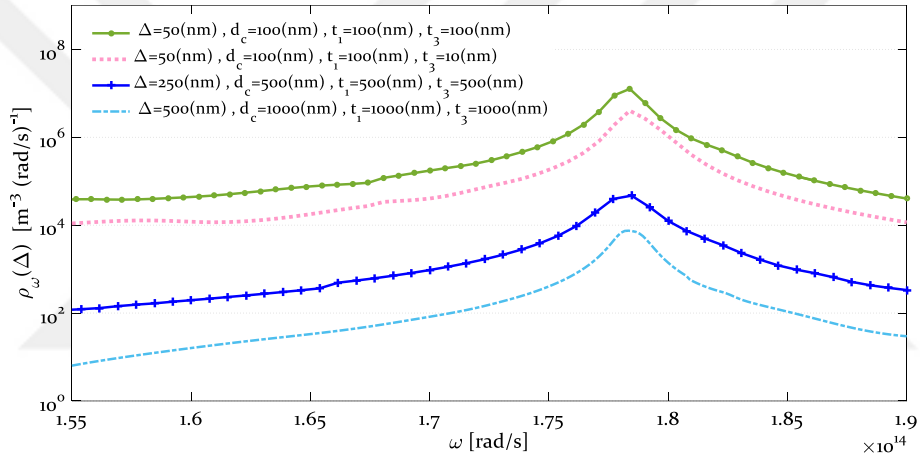


**Figure 3.8** The effect of gap size on the LDOS profile.

### 3.4 Dispersion Relation of SPhPs in Thin Films

The dispersion relation is the relationship between the periodicity of the wave in time and its periodicity in space. In thin films, the evanescent field of SPhPs associated with each interface can interact with each other, thus leading to a splitting of the SPhP dispersion relation into antisymmetric  $\omega^+$  (high frequency) and symmetric  $\omega^-$  (low frequency) modes. Comparison of the dispersion relations for 10 nm and 100 nm thick single SiC films in vacuum reveals that as the thickness of the film decreases, the resonance

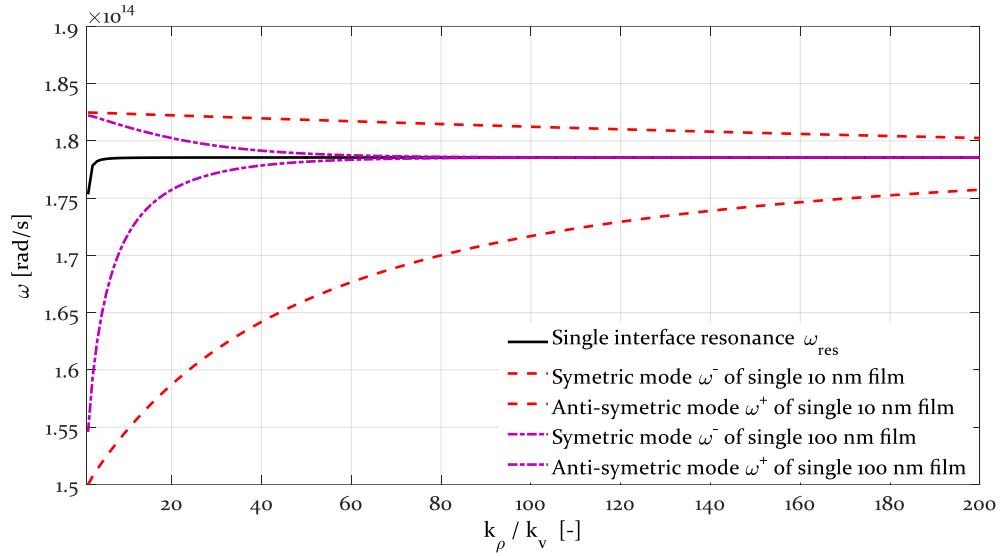


**Figure 3.9** Dispersion relation of SPhPs for single  $t_1 = 100$  and  $t_1 = 10$  thick SiC films at the interface with vacuum.

drastically splits in to the symmetric and anti-symmetric modes. Dispersion relations of SPhPs for a single SiC layers of 10 nm thickness and 100 nm is given in Figure 3.9.

When two films supporting SPhPs are placed in close proximity, further coupling takes place, and the dispersion relation splits into four branches showing anti-symmetric and symmetric resonances for each film and for the entire structure. For the case of  $t_1 = 100$  and  $t_3 = 10$  thick SiC films in vacuum and separated by a gap 100 nm, the dispersion relation is given in Figure 3.10 and the results are compared with the dispersion relations of a single SiC-vacuum interface.

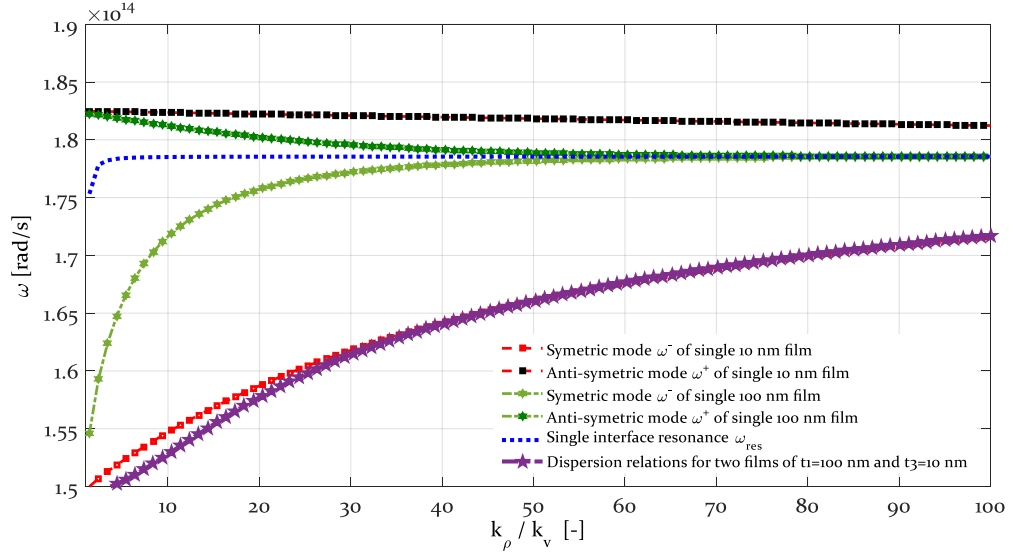


**Figure 3.10** Dispersion relation of SPhPs for  $t_1 = 100$  and  $t_3 = 10$  thick SiC films in vacuum and separated by a gap 100 nm.

### 3.5 Concluding Remarks

A methodology of finite difference time domain analysis (FDTD) for the calculation of the polariton-enhanced near-field thermal radiation emission based on the local density of electromagnetic states (LDOS) is presented. The geometry and the methodology are discussed, and the limitations and advantages of the FDTD method are explained.

Based on the results, we are now confident that the *NF-RT-FDTD* algorithm can deliver results for more complex geometries, such as using layers with non-ideal (rough) surfaces or with nano-particles placed on them. From our literature serch, we know that there may not be any accurate analytical solution to describe the radiative heat transfer using irregular or rough surfaces.

We have shown that the Green tensor function can be obtained using the FDTD method and the LDOS expression can be derived from the Green tensor function. During the course of this work it was confirmed that the Ricker wavelet is more appropriate as an excitation source than a Gaussian pulse when simulating a Dirac Delta Function.

When dealing with surface phonon polaritons, a time domain computational method such as FDTD needs to deliver for numerical dispersion, absorbing boundary conditions and an accurate permittivity model, hence making the simulations very expensive and sometimes impossible. Yet, it is possible to overcome these difficulties.

We observed that when working with plasmonic materials, the permittivity of the material not only had an effect inside the material but also on the grid points adjacent to the material itself. Hence, handling the grid sizes as well as the boundaries in a multilayer structure as the one presented in this work are of vital importance for the robustness of the solution methodology. Comparisons made between the analytical and current FDTD analysis of the Drude-Lorentz permittivity model show an excellent agreement.

Results presented here suggest that the CPML is the optimum boundary condition in using the FDTD method to analyze more complex geometries (e.g. analysis of near field thermal radiation between a tip and a sphere) for which an analytical solution may not be achievable. This boundary condition hence allows more streamlined simulations to be carried out when working with sub-wavelength structures. The diversity of geometries considered and the physical systems analyzed will be significantly increased with this approach, allowing a clearer impact to the development of novel nano-diagnostics and nano-manufacturing modalities

The exact size of the CPML layers, as well as the CPML parameters, for the different geometries (SiC layer and gap thicknesses) can only be found empirically at this stage. Further work will be carried out to identify the causes of the small high-pass/ low-pass discrepancies of the LDOS response around the resonance frequency.

The results for the FDTD analysis of LDOS in vacuum are also presented. We calculated LDOS at  $\Delta = 50$  nm when the thickness of both SiC layers is  $t_1 = t_3 = 100$  nm and the interfilm vacuum gap is  $d = 100$  nm,  $d = 500$  nm and  $d = 1000$  nm. The results

of simulation for the case where  $t_1 = 100$  nm and  $t_3 = 10$  nm were also presented, with LDOS being calculated for  $\Delta = 50$  nm, and a comprehensive study of the results was given. The results showed a clear enhancement of LDOS profile by three orders of magnitude when the distance between films are less than 500nm. It is worth mentioning that simulation time at the final stage of this work was reduced from 48 hours to an average time of 2-6 hours. This shows the positive effect of the various changes that were applied to our FDTD code described above. To the best of our knowledge, the accuracy of the results found in this work has not yet been surpassed by any computational methods presently known which provides a great hope for future use of FDTD method on near-field thermal calculations with any arbitrary geometries.

## CHAPTER IV

### NEAR-FIELD THERMAL EMISSION IN CORRUGATED SURFACES SEPARATED BY NANO-GAPS

Near-field thermal radiation with its many potential applications in different fields requires a thorough understanding for the development of new devices. In this Chapter, we report that near-field thermal emission between two parallel SiC thin films separated by a nano-gap, supporting surface phonon polaritons, as modelled via Finite Difference Time Domain Method (FDTD), can be enhanced when structured nanoparticles of different shapes and sizes are present on the surface of the emitting films. In this Chapter, we compare different nano-particle shapes and discuss the configurations which have the highest impact on the enhancement of near-field thermal emission and on the near-field heat flux.

Some of the contents of this Chapter were published in the *Journal of Quantitative Spectroscopy and Radiative Transfer* in 2015 [88].

#### ***4.1 LDOS Profiles in Corrugated Thin Films***

Near-field thermal radiation between thin films where the emitting layer has surface corrugations in the form of nanoparticles is investigated through calculation of Transverse Magnetic (TM) evanescent component of Local Density Of Electromagnetic States (LDOS) within the vacuum nano-gap separating the films.

The origin of the coherent emission lies in the diffraction of surface-phonon polaritons (surface waves) by the grating. Surface modes have a wavevector larger than  $2\pi/\lambda$  so that they are evanescent and their effects are not seen in the far-field. However,

by ruling a grating on the interface, we are able to couple these surface modes to propagating modes. Thus, by modifying the characteristics of the surface profile, it is possible to modify the direction and the value of the emissivity of the surface at a given spectrum at distances several wavelengths above the surface.

Figure 4.1 depicts flat SiC layers separated by a vacuum gap in the benchmark scenario (a) and scenarios when nanoparticles of different shapes are added to the surface of the emitting layer (b-d). The change in the characteristics of the near-field thermal emission is expected to be significant and measurable compared against the benchmark result. Width and height of the nanoparticles is shown in Figure 4.1 with  $w$  and  $h$  respectively. The distance of nanoparticles is shown with ' $d_n$ ' and NPs stands for nanoparticles from hereon. In this scenario, nano-structured gratings of arbitrary shape (e.g. ellipses, triangles, squares, etc.) are placed upon the emitting layer and have perfect contact with it. We then evaluate the impact of the following factors on the results: I-the periodicity of the nano-gratings, II-the shape of nano-gratings and III-the size of the nano-gratings.

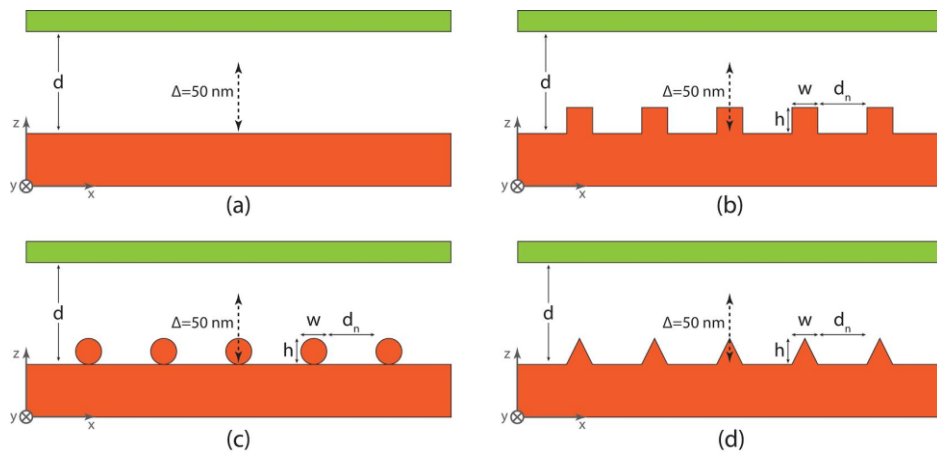


**Figure 4.1** Geometries considered for Corrugated Thin Films. **a)** Perfectly flat parallel films separated by nano-gap. (emitting layer at the bottom, non-emitting layer on top). LDOS/Flux is calculated at 50 nm above the emitting layer in all configurations. **b)** Rectangular nanoparticles placed on the emitting film separated by nano-gap from non-emitting film. **c)** Ellipsoidal nanoparticles placed on the emitting film separated by nano-gap from non-emitting film. **d)** Triangular nanoparticles placed on the emitting film separated by nano-gap from non-emitting film.



We have modeled a 2D geometry, i.e. with no propagation in the Y direction. Therefore, the nanoparticles are rectangles, ellipses and triangles rather than rectangular parallelepipeds, ellipsoids or pyramids. The emitting and non-emitting layers are finite in the Z-direction and infinite in X. As the computational space is by necessity finite, Convolutional Perfectly Matched Layer (CPML) boundary conditions are used to eliminate reflections from the physical edges into the problem space [62]. A detailed study on the choice of boundary condition is given in Section 3.1.

In Figure 4.2 the comparison of four different scenarios is given. In A, the benchmark results in which no NPs where present is given. Scenario B shows no change in the LDOS profile when 2 SiC gratings of  $w=600$  nm and  $h=20$  nm are placed by  $d_n=1200$  nm apart from each other on top of emitting layer. In scenario C, 6 NPs, each having  $h=20$  nm and  $w=600$  nm were placed by  $d_n=600$  nm apart from each other on top of the emitting layer and a slight change in the LDOS profile was observed. However, the magnitude of the LDOS at the resonance frequency stayed the same. In scenario D, we have repeated scenario C, only this time with 11 NPs of the same size. The results show a clear increase of about 70% in the magnitude of the LDOS at resonance frequency.

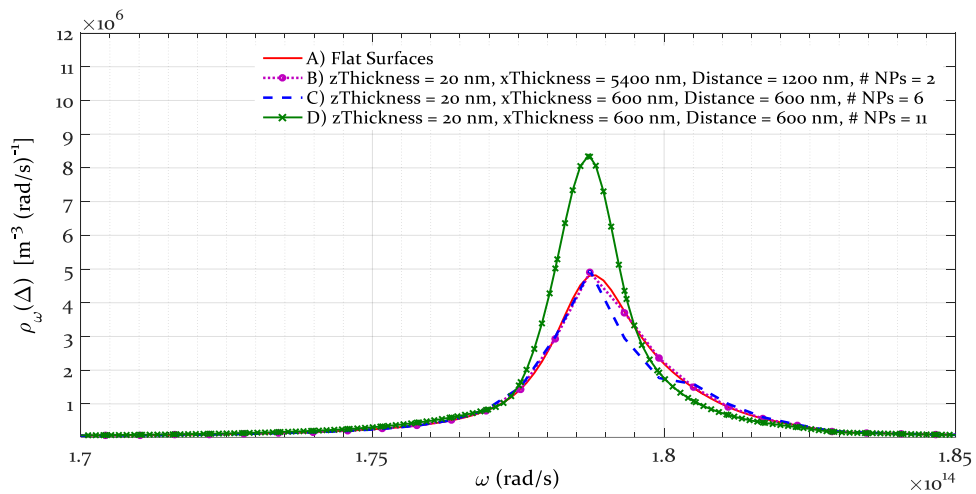


**Figure 4.2** LDOS profile vs. frequency for A, B, C, D configurations.

We have next evaluated the impact of periodicity of elliptic nano-structured gratings placed on the emitting layer. We have compared the results of separate scenarios in which 2, 5, 10, 15, 20 and 25 SiC elliptic nano-gratings were placed in perfect contact with the emitting layer. The size of ellipses was kept fixed and only the impact of periodicity of the gratings was observed. Each ellipse has a  $w=600$  nm and  $h=20$  nm. Here,  $w$  is chosen based on the fact that the thin layers are assumed to be very long in X-direction for these FDTD simulations. Hence,  $w$  has to be both small compared to the total length of the layers and yet not too small to make the simulation computationally too expensive. The distances between 2, 5, 10, 15, 20 and 25 nano-gratings were 14700, 3180, 1080, 480, 180, and 60 nm, respectively. We kept the X axis dimension and the width of CPML layers fixed across all simulations. Within this constraint, we could only fit up to 25 nanoparticles across. This provided adequate scope for a robust proof of concept. The results which are depicted in Figure 4.3 show that the enhancement factor of LDOS profile is directly proportional to periodicity of nano-particles. In the case of 25 NPs each 60nm apart from each other, 71% enhancement was observed when compared with the benchmark scenario in which no NPs were present at the surface of the emitting layer. We can observe that when  $d_n < 0.005\lambda$  ( $\lambda = 1059$  nm) we obtain maximum enhancement of LDOS.

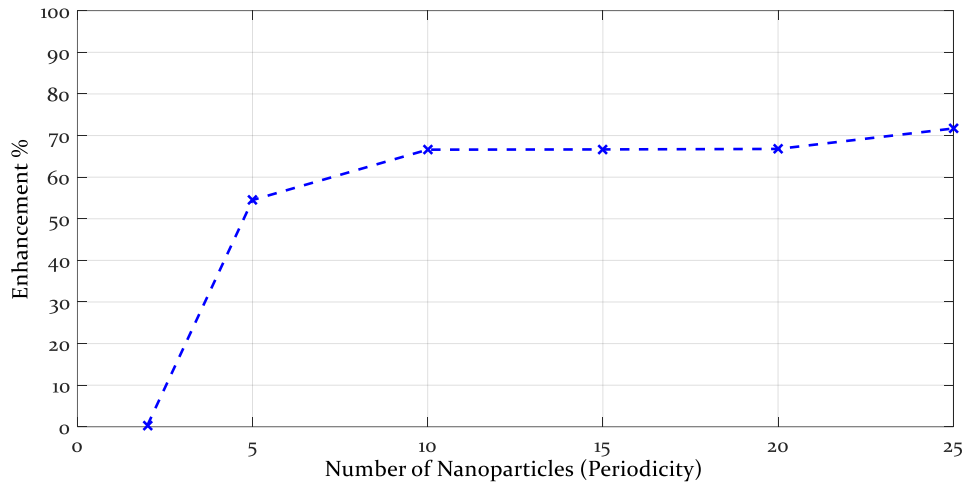


**Figure 4.3** Enhancement Factor vs Periodicity for SiC elliptic nano-particles.

## ***4.2 Heat Flux Profiles in Corrugated Thin Films***

In this section, we have studied the effect of different shapes of nanoparticles in near-field heat flux. Rectangular nano-particles show the greatest impact on enhancement of near-field heat flux when placed on the emitting layer and compared against elliptical and triangular nanoparticles. In Figure 4.4 we have compared the results of near-field flux found at 300, 600 and 1000 K when 25 elliptic NPs were placed on top of the emitting layer against the benchmark results in which there were no NPs present. The results are normalized to the peak value of the benchmark scenario. Enhancement of near-field flux at different temperatures due to the presence of the NPs can be clearly seen. In Figure 8 we have compared the results of near-field flux found at 300, 600 and 1000 K when 25 elliptic NPs were placed on top of the emitting layer against the benchmark results in which there were no NPs present. The results are normalized to the peak value of the benchmark scenario. Enhancement of near-field flux at different temperatures due to the

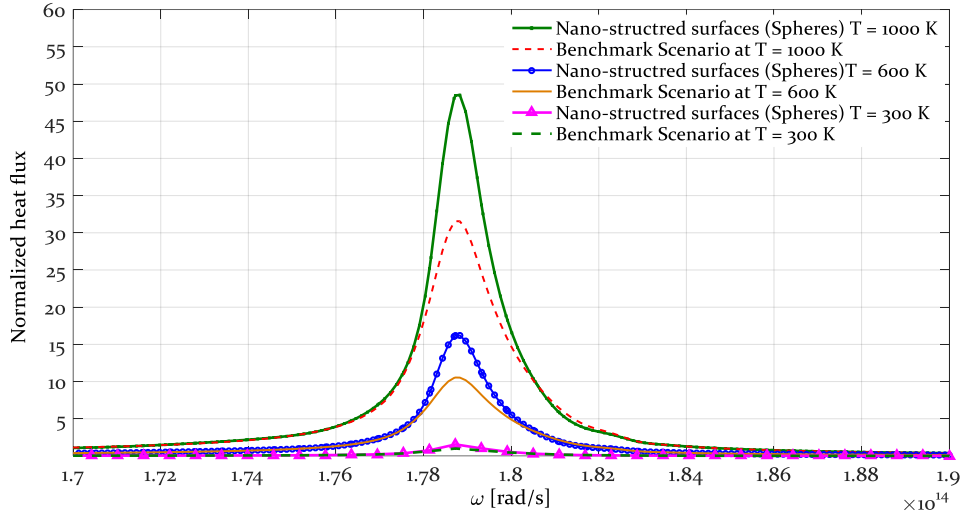


**Figure 4.4** Near-field heat flux calculation at 300, 600 and 1000 K at presence of elliptic nanoparticles vs the benchmark scenario where no NP are present at the surface of the emitting layer.

presence of the NPs can be clearly seen. The root cause of the enhancement can be found by examining the dielectric properties of the material and the physical interpretation of the behavior is based on arguments from solid-state physics.

In the next step, we have compared the Flux profile found for 10, same size nano-gratings placed on the emitting layer with different shapes. Results for rectangles, ellipses and triangles are compared with each other in Figure 4.5. It was observed that rectangles and ellipses show a similar impact on enhancement of flux when compared against triangles, with a slightly higher enhancement observed for rectangles. Nano-gratings were set to have  $w=600$  nm and  $h=20$  nm and  $d_n=1080$  nm ( $d_n = 0.1\lambda$ ).

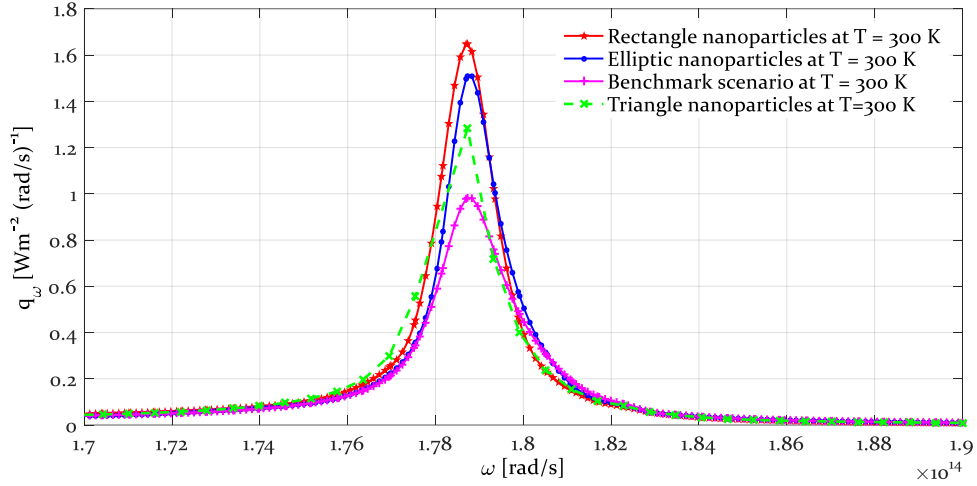


**Figure 4.5** Enhancement of heat flux at the presence of NPs (over benchmark scenario) vs different shapes of nano-gratings.

### 4.3 Concluding Remarks

Near-field thermal radiation has broad range of applications in areas including nano-manufacturing, nano-imaging, thermal rectification and energy harvesting with applications in thermophotovoltaics. Usually the practical systems have complex geometries, for which analytical solutions cannot be used readily. Having a computational technique such as FDTD that can model complex electromagnetic geometries, in dispersive, anisotropic mediums is critical for the advances in the field. We have developed *NF-RT-FDTD* to model arbitrary shape nanoparticles and have evaluated their impact on LDOS as well as in heat flux profile. The results show an increase in the magnitude of LDOS with an increase in the periodicity of the nano-gratings, when the distance between the gratings is much smaller than the wavelength of interest. In the case of 25 elliptical NPs each 60 nm apart from each other when each ellipse had a  $w=600$  nm and  $h=20$  nm, 71% enhancement was observed when compared with the benchmark scenario in which no NPs were present at the surface of the emitting layer. We also

observed that when  $d_n < 0.005\lambda$  ( $\lambda = 1059$  nm) the maximum enhancement of LDOS is achieved.

We evaluated the impact of the arbitrary shape nano-gratings and observed that rectangles showed the greatest impact on enhancement of LDOS and heat flux value when compared against ellipses and triangles of the same sizes. Enhancement of near-field flux at different temperatures due to the presence of the elliptic NPs could be clearly seen when compared against the benchmark scenario in which no NPs were present.

In this Chapter, we extended the FDTD computational approach to describe near-field radiative transfer between corrugated surfaces separated by nano-scale gaps. The premise of these calculations is that LDOS varies both in normal and lateral directions, making the problem a two, or more correctly, a three-dimensional one even for one-dimensional near-field calculations. This means that LDOS profiles above nanostructure varies along with LDOS profiles to the right or the left of a structure. Depending on the size and shape of the structures the local near field radiative transfer is bound to change. This is expected, as due to the wave nature of the EM energy exchange, interference effects are to come into picture. The results show that depending on the particle configurations, periodicity, shape and size we see both enhancement and decrease in the local flux profiles.

The methodology presented here to determine near field radiative transfer between two corrugated surfaces is much more fundamental than a simple use of an effective medium theory, which is questionable at nano-resolutions and is investigated in Chapter 5.

With the observations from this study and the insight gained from these modeling efforts, we should be able to define more complicated functions for the corrugated geometries based on near-field enhancements or annihilations.

## CHAPTER V

### **NEAR- TO FAR-FIELD COHERENT THERMAL EMISSION BY CORRUGATED SURFACES AND THE EVALUATION OF EFFECTIVE MEDIUM THEORY**

With the ever increasing human population and with their insatiable thirst for energy, the world is facing a double challenge of climbing energy demand and a threat for energy security. Along with energy efficiency measures, the development of new ideas and devices for energy harvesting from all kinds of high temperature sources are more pressing than before. Both of these areas can benefit potential solutions from new and innovative ideas, particularly with the use of new materials, and different chemical and/or physical (geometric) configurations. Nanotechnology-based techniques have been investigated widely in the past decade with the intention of further developing Negative-index (NIM), double-negative index (DNI) and Hyperbolic Metamaterials (HMMs) due to their unusual characteristics when interacting with light [74–79]. The Effective Medium Theory (EMT) based on field averaging technique has been extensively used when working with these metamaterials to investigate the far-field radiative transfer [76,80]. Agreement of EMT with computational techniques, such as FDTD, could be good when the unit cell dimension of the considered geometries is much less than the wavelength of incident wave [80,81].

Liu and Shen [82] investigated the near-field radiative heat flux between a SiC film and metal nanowire arrays at small gap distances using the Wiener Chaos expansion method and reported that that EMT will overestimate the near-field radiative heat flux.

Tschikin et al. [83] indicated that EMT may cease to evaluate the radiative transfer at small distances when surface waves exist between the layers on both sides of

the vacuum gap. In general, for the EMT to be valid, the gap size between mediums should be much greater than the period of the unit cell of the geometry considered [84].

Metamaterials based multilayered structures consist of large working surface area compared structures such as plane-tip configurations, hence they are considered more promising for efficient thermal control and near-field TPV devices.

Liu et al. [85] reported the applicability of EMT to accurately evaluate near-field radiative heat flux by comparison with exact solutions for multilayered metamaterials, where it was shown that EMT could predict the s-polarized radiative heat flux for metal-dielectric configurations at any gap distance, however some discrepancies exist for metal-metal and dielectric-dielectric configurations. For p-polarized waves, the cut-off wave vectors were quantitatively acquired for surface and hyperbolic modes and a criterion was obtained so that EMT can reliably predict the near-field radiative heat flux. However, the extension of the methodology's shows the validity condition of EMT for other types of metamaterials, such as nanowires and corrugations which were not explored.

Near-field thermal radiation may play significant role in the enhancement of energy harvesting and radiative cooling by new types of designer materials, which in turn can be crucial in the development of future devices.

In this Chapter, we present a case study to explore near- to far-field thermal emission and radiative flux from a thin polar SiC film coated by nanoparticles of different size and shape. The same geometry with nano-particles is also considered as a layered medium, which is analyzed using EMT. A significant enhancement of emission, particularly at the far infrared, is observed when nanoparticles are placed on the surface of a SiC film with certain periodicities, which shows potential use of these structures for radiative cooling applications. Yet, these enhancements are not observed when the EMT



approach is adapted, which makes EMT questionable for its accuracy of predicting near-to-far field transition regime of radiation transfer from corrugated surfaces.

Some of the contents of this Chapter were published in *Optics Express* in 2015 [100].

### ***5.1 Near-To Far-Field LDOS Above a Single Layer and a Corrugated Layer***

We here present the effects of different shape and size Nanoparticles (NPs) on near- to far-field emission, absorption and the spectral radiative flux extended from the far-infrared region to the start of visible spectrum, corresponding to the wavelengths of 400 nm to 100  $\mu\text{m}$ . We compare the results found for different size and shape SiC NPs placed on the surface of a thin SiC film. In addition, we show results obtained with the Effective Medium Theory (EMT), where the structures are assumed to form a thin layer over the original substrate as it will be discussed below, then we conclude that EMT's accuracy in providing the effect of presence of nanoparticles on surfaces in calculations of emission and absorption is highly questionable.

The configuration considered here is a single thin SiC film either perfectly flat (benchmark) or coated with SiC NPs on it, as shown in Figure 5.1. The simulations were carried out to determine the profiles of LDOS and the radiative flux. The emitting film is assumed to have a temperature of 1000 K and a thickness of 100 nm. We first studied the LDOS profile 50 nm above the single SiC film and then compared it with the values found for heights at 3  $\mu\text{m}$ , 20  $\mu\text{m}$ , 30  $\mu\text{m}$  and 100  $\mu\text{m}$ . Furthermore, we considered different size of NPs of spherical, elliptical, rectangular and triangular shapes in perfect contact with the emitting film and compared the LDOS results against the initial benchmark results. Finally, we compared the latter results against those obtained using the EMT.

Width and height of the NPs is shown in Fig. 5.1 with ' $w$ ' and ' $h$ ', respectively and the distance of NPs is shown with ' $d$ '.

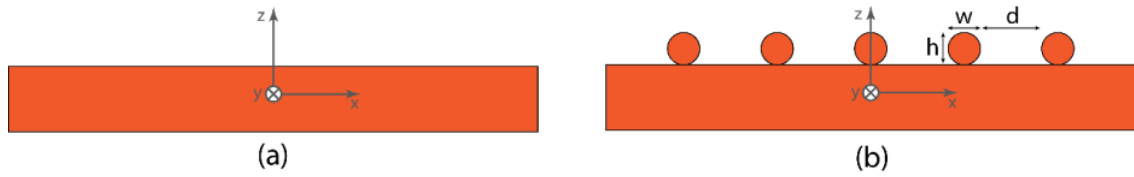


**Figure 5.1**(a) Perfectly flat thin SiC film. (b) Spherical NPs placed on the emitting film.

Our main objective is to identify the most important factors when tailoring the nanostructures in order to obtain enhancement or annihilation of NF thermal emission and radiative flux for different applications. For this purpose, we considered employing nanospheres of different sizes placed on the surface of emitting layer in the proposed configuration. For the first set of analyses, the NPs are assumed to have diameters of  $w=h=350$  nm. The scenario in which LDOS is calculated for a single thin layer SiC film and found at a distance  $\Delta=100$   $\mu\text{m}$  above the emitting layer is compared against the same scenario when nanospheres are sitting upon the surface of the film. These are shown in Figure 5.2. We observed two orders of magnitude increase in the magnitude of LDOS after the NPs are placed on the surface. The magnitude of LDOS started to show much higher values at frequencies near the visible spectrum when compared against the single thin film case. A similar computational observation was previously reported [86] for near infrared spectrum. However, the effect of different sizes of NPs in a comparative study against the case of a single thin film as well as the EMT calculations over the infrared spectrum are reported here the very first time.

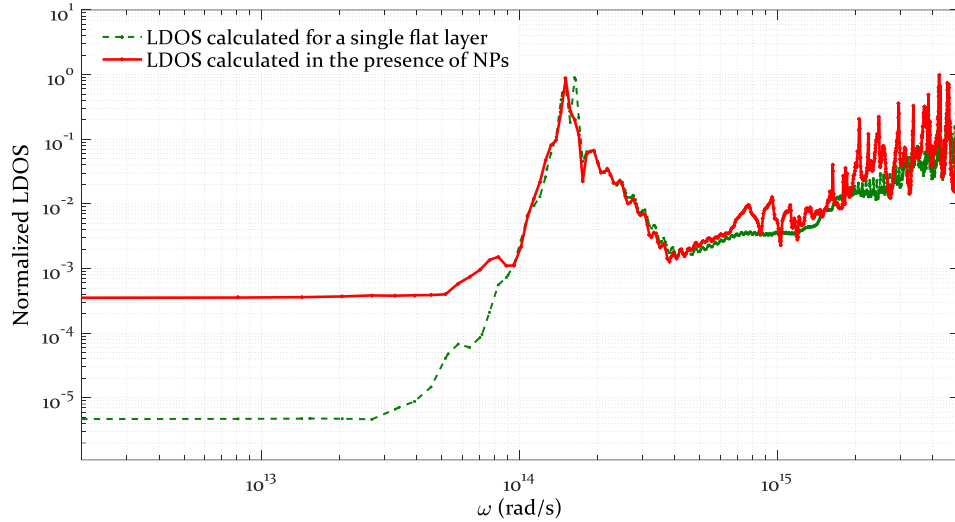


**Figure 5.2** Comparison of spectral LDOS profiles for the benchmark scenario against corrugated SiC layer.

### ***5.2 Near-To Far-Field LDOS evaluation by Effective Medium Theory***

Next, we compared the results we obtained in Figure 5.2 against those obtained using EMT. Figure 5.3 depicts the comparison of the LDOS profiles obtained for (a) a single film, (b) a corrugated single layer and (c) LDOS calculated with EMT through volume fraction studies of NPs. We observe that solutions of conventional EMT which can be obtained through knowing the relative volume fraction and permittivity of the constituent media for Near-Field Radiative Transfer (NFRT) problems dealing with corrugated surfaces may depend on a number of factors among which is the size of NPs and the observation point at which LDOS/heat flux profiles are obtained which effects the dimensions of the numerical problem under the study. Also, the method adopted for EMT calculations are among these factors. Our results are based on the EMT studies that were performed through volume fraction studies of NPs where 2D-EMT was applied by calculating the total area (in cells) occupied by NPs. Next, we adjusted the height of emitting layer so that its own total area is increased by the area calculated for NPs; then the simulation is run without NPs. From the results, it might be concluded that the

discrepancy between FDTD and EMT method predictions is due to the fact that the conventional EMT is incapable of describing systems where the change in dielectric permittivity from layer to layer is large. This usually happens when the medium is made of a metamaterial adjacent to any other medium with a much different permittivity. i.e. vacuum. Also, when the overall physical size of the geometry is smaller than the wavelength of interest, EMT's results seem to be highly questionable.

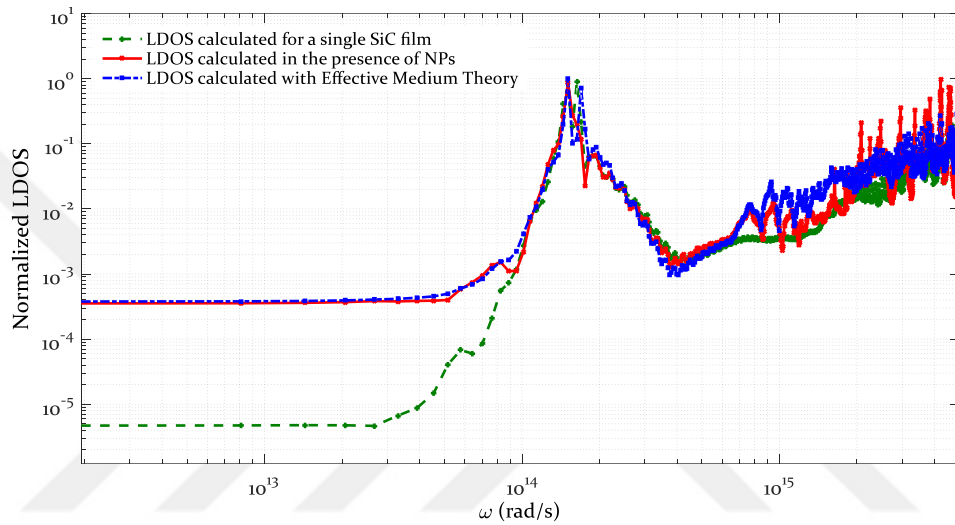


**Figure 5.3** Comparison of results for LDOS for a single film, in the presence of NPs of diameter of 350 nm and the corresponding EMT.

In Figure 5.4 we have magnified the results shown in Figure 5.3 over the frequencies near visible range with the purpose of a clearer exploration of the results.

In addition, we considered an array of SiC rectangles with  $w=h=200$  nm on SiC emitting layer, at  $T=1000$  K. Results for coherent thermal emission and radiative flux at a distance  $\Delta=30$   $\mu\text{m}$  above the emitting layer are depicted in Figure 5.5 which shows the results obtained for (a) the benchmark scenario, (b) LDOS profile in the presence of rectangular-shaped NPs, and (c) results obtained from EMT. The results are normalized to the peak of benchmark scenario. Furthermore, the radiative flux profiles from FDTD simulations were compared against those obtained for EMT, as shown in Figure 5.6. An enlarged

version of these comparisons are also included in Figure 5.6. Note that near-field thermal flux could be evaluated based on LDOS calculations as explained in detail in [87]. We compared the predictions for thermal emission and the radiative flux obtained for corrugated surfaces against those for the flat surfaces and observed a clear enhancement by several orders of magnitude at a number of spectral bands. This enhancement is due to coherent coupling between the resonant modes generated by surface phonon polaritons. We have also observed that there is a discrepancy between results found for LDOS and the radiative flux in the presence of nano-particles and those corresponding to the EMT calculations, for the cases studied here as well elsewhere [88]. Therefore, we conclude that the use of the EMT approach for sub-wavelength metamaterial nanostructures seems highly questionable over the infrared frequencies, particularly near the visible region.

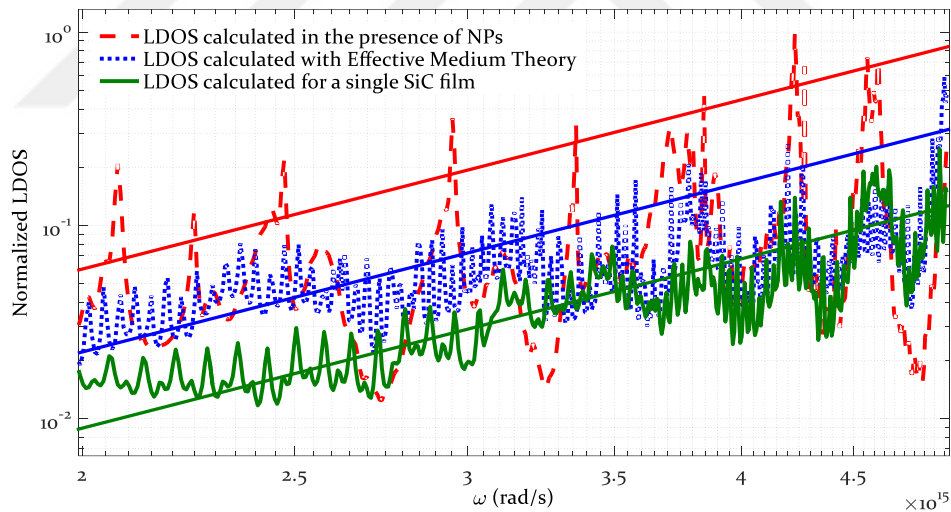


**Figure 5.4** Magnified LDOS profile results over near visible spectrum.

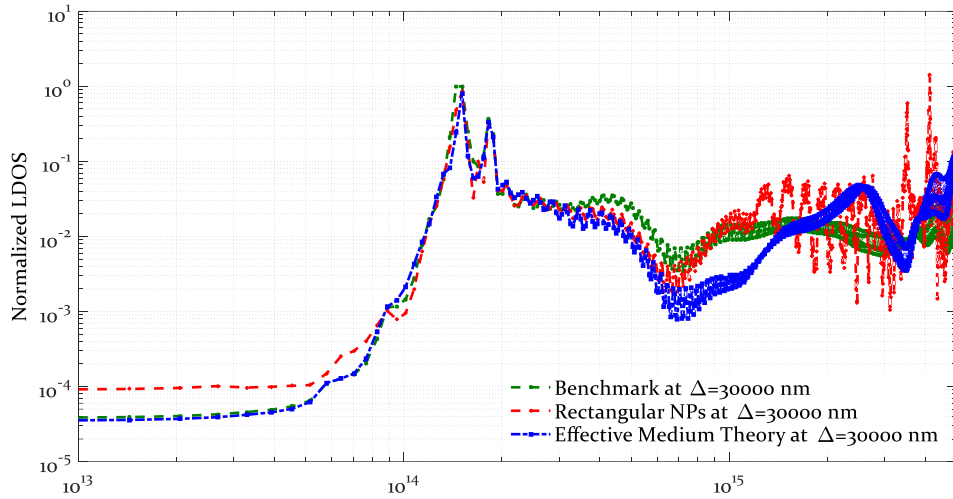


**Figure 5.5** Comparison of results found for LDOS for a single film, in the presence of rectangles of  $w=h=200$  nm and with EMT.

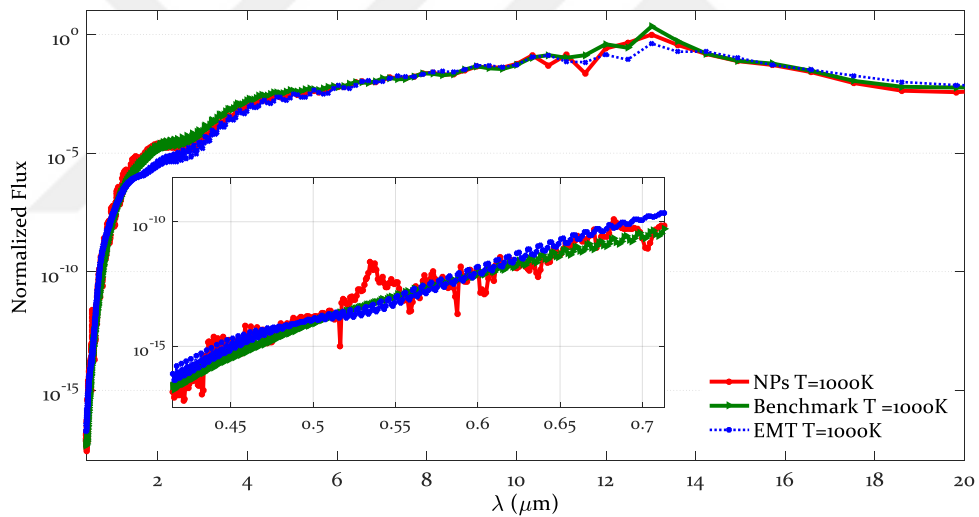


**Figure 5.6** Comparison of results for radiative flux vs. wavelength for a single film, in the presence of rectangles with  $w=h=200$  nm and those based on the EMT. The inset shows an enlarged version of these comparisons for wavelength range of  $0.4\text{-}0.7\mu\text{m}$ .

### ***5.3 Concluding Remarks***

The results presented in this Chapter showed that the presence of NPs on the surface of an emitting layer increases the magnitude of LDOS and the radiative flux, within specific spectral bands, by several orders of magnitude. A noticeable amount of discrepancy was also observed when the results obtained with EMT were compared against those obtained with *NF-RT-FDTD* in the presence of the NPs. Note that the methodology presented here to determine NFRT between corrugated surfaces is much more fundamental than a simpler EMT, which does not seem to be accurate at nano-resolutions. With the insight gained from these modeling efforts, we should be able to define more interesting functions for corrugated geometries, specifically targeting near-field enhancements or annihilations.

## CHAPTER VI

### NEAR-FIELD THERMAL RADIATION TRANSFER BY MESOPOROUS METAMATERIALS

In the recent years, there has been a dramatic increase in the literature dealing with design, characterization and property evaluation of the mesoporous materials such as Silica for catalysis [89,90], adsorption [91,92] and separation [93–95]. Studies have shown that near-field thermal radiative transfer could be enhanced by orders of magnitude in porous materials when compared with non-porous materials in identical configurations.

The two important studies which discuss the effects of pores on the near-field radiation transfer are those by Biehs et al. [96] and Li et al. [97]. In [96], Biehs et al. reported the heat flux between nanoporous materials through an EMT calculation where both layers were air filled porous SiC [96]. In [97] Li et al. showed experimentally that when mesoporous Silica material was used for pore sizes between 2-50 nm, the near-field heat flux was enhanced by orders of magnitude when compared with non-porous Silica.

In this Chapter, we investigate the impact of nano-scale pores within structured metamaterials on spectral near-field radiative transfer. The radiative heat transfer across a pore is calculated by using fluctuation-dissipation theorem and dyadic Green's functions to compute the Poynting vector. We consider uniform and corrugated SiC substrates filled with rectangular nano-scale vacuum inclusions and we report appearance of the secondary and tertiary resonance peaks at different frequencies as a function of changing pore diameter, which cannot be predicted if an Effective Medium Theory approximation is used. Figure 6.1 depicts the top view of a typical mesoporous material.

Some of the contents of this Chapter were published in *Optics Express* in 2015 [101].



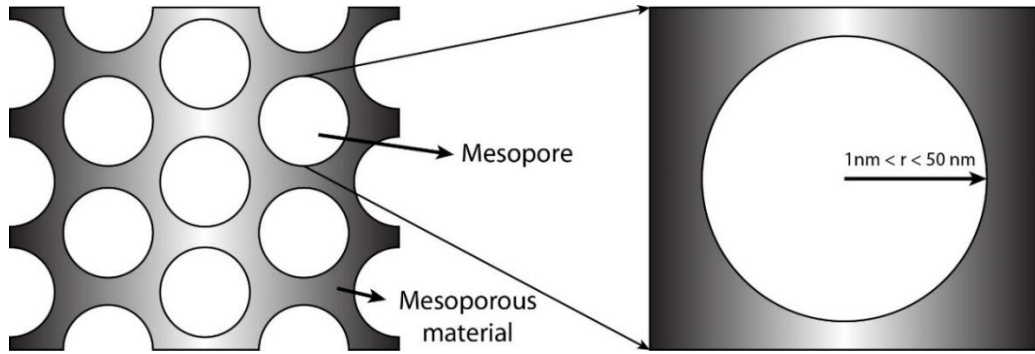


**Figure 6.1** Schematics of top view of a typical mesoporous material in which the radius of the pore is  $1 \text{ nm} < r < 50 \text{ nm}$ .

### ***6.1 Near-Field Thermal Emission in Mesoporous SiC Layers.***

Here, we explore the near-field radiative heat transfer in porous metamaterials of thin films, which are considered to be either uniform or having nano-structures on them; they may also contain uniformly distributed nano-size pores within (see Figure 6.2). For simulations, the emitting and non-emitting layers are assumed to be 100 nm and 10 nm thick SiC films with a separating vacuum gap of 100 nm. The width and height of nanoparticles (NPs) on the emitting layer are designated as ‘ $w$ ’ and ‘ $h$ ’ respectively.

In the simulations, the values of  $w=500 \text{ nm}$  and  $h=20 \text{ nm}$  are used and the horizontal spacing between them is kept at 50 nm. We designate the equivalent diameter of the pores as  $D_{eq}$  and they are considered as rectangles in the simulations, where the width  $P_w=50 \text{ nm}$  and the height  $P_h=30 \text{ nm}$  are chosen. Here, the equivalent diameter is defined as  $D_{eq} = 2 \times (P_w \times P_h) / (P_w + P_h)$ . The horizontal spacing between the pores is set to 50 nm and the vertical spacing is 2 nm. The emitting layer is assumed to have temperature of  $T=1000 \text{ K}$  and the non-emitting layer is kept at  $T=0 \text{ K}$ .

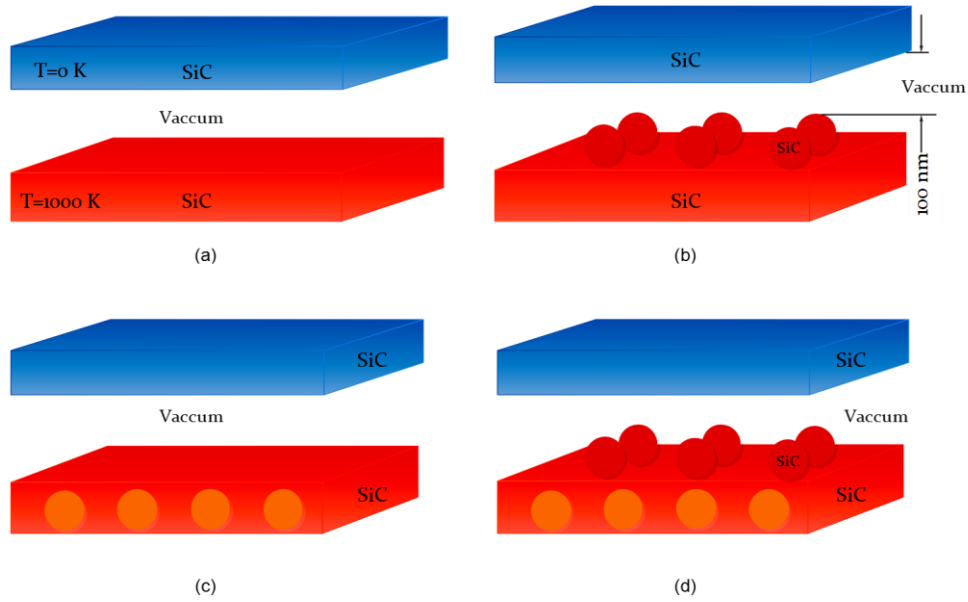


**Figure 6.2** Mesoporous SiC Layers. **a)** Perfectly-flat parallel thin films separated by nano-gap (emitting layer at the bottom, non-emitting layer on top). **b)** Rectangular nanoparticles placed on the emitting film separated by nano-gap from non-emitting film. **c)** Porous SiC emitting layer separated by a vacuum gap from non-porous SiC non-emitting layer. **d)** Corrugated porous SiC emitting layer separated by a vacuum gap from non-porous SiC non-emitting layer.

First, we present the results for the Local Density of Electromagnetic States (LDOS) for different configurations. We then report the near-field emission and near-field heat flux profiles for different scenarios. Then, we identify the profiles in which maximum rate of radiative heat transfer is obtained. The comparisons between FDTD and EMT analysis are made afterwards which accentuates the possible weaknesses of EMT in providing accurate results when dealing with porous metamaterials. After obtaining the results for the benchmark scenario in which both layers are non-porous SiC thin layers separated by the vacuum gap, we provide a comparison between the benchmark scenario against the scenario in which the emitting layer is a porous SiC filled with vacuum inclusions with different equivalent diameters. Particular emphasis is to be given to the appearance of the additional resonance peaks obtained when there are nano-pores within the emitting layer.

Here, we thoroughly investigate the behaviour of near-field thermal emission/radiation of a porous SiC emitting layer having pores with the equivalent diameters of 10, 37 and 57 nm, respectively. The main reason for the choice of these pore sizes came from Li et al. [97] where they discussed that when the diameter of the pore is much smaller than the thermal wavelength, the electromagnetic field across the pore is dominated by the near-field radiation, and the combined thermal conductivities of mesoporous Silica decreases gradually with the pore diameter increasing. They report that when the pore's diameter is smaller than 50 nm (mesoporous pores) the enhancement rate is higher than when compared against the porous materials having pore diameters larger than 50 nm. For this reason, we chose the size of the pores (width and height) such that the equivalent diameter would become smaller and larger than 50 nm.

Furthermore, the results here are also compared against those obtained from the equivalent EMT analysis. In order to implement the EMT, the total surface area of the vacuum voids is calculated (in 3D it would be total volume) and is then subtracted from the surface area of the porous SiC material. The result corresponds to an isotropic SiC layer of a reduced thickness and the LDOS is recalculated using the same vacuum gap size and non-emitting SiC layer. The results and our observations are discussed in the next section.

We first investigate the impact of nano-pore sizes of 10, 37 and 57 nm within SiC structure on the LDOS profiles and present the results in Figure 6.3, 6.4 and 6.5, respectively. These results are found at 30 nm above the emitting layer, and are normalized to the peak of the benchmark scenario. Our observations show that when  $D_{eq}$  is either 10 or 37 nm, the near-field thermal emission shows a significantly larger magnitude than the benchmark case or when compared against the case where the non-porous emitting layer is corrugated. Figure 6.3 depicts the results of comparison between

benchmark case against the scenarios in which LDOS results for porous emitting layer is obtained through the FDTD and the EMT simulations. These results are then compared against the case for porous medium. Introducing porosity in SiC emitting layer increases the magnitude of LDOS and produces an additional resonant peak when the pore sizes are small which shows the potential of this structures to produce additional spectral characteristics. The physical mechanism for the appearance of the additional resonance peaks may be associated with the strong coupling of the pores' cavity resonances with those stemming from the surface phonon polaritons. The additional enhancement introduced by the porous emitting layer could be associated with the fact that the dominance of the p-polarized contribution in the near-field regime becomes even greater when having vacuum inclusions. Our studies show that when the horizontal distance between the pores is increased, the magnitude of the peaks decreases and eventually the additional peak vanishes when the pores' horizontal spacing reaches to 150 nm. It is apparent that beyond a given distance, the coupling does not take place. On the other hand, if we replace the emitting smooth layer with a corrugated porous layer, we observe that the enhancement rates are higher. The equivalent EMT analysis for these case studies can neither produce the same enhancement rates nor could show the additional resonant peaks. In Figure 6.3, we compare the results when  $D_{eq}=10$  nm, for porous SiC emitting layer against the benchmark scenario, where the SiC resonant peak occurs at  $1.79 \times 10^{14}$  rad/s. It is important to note that we have 73% spectral enhancement in the LDOS profile here. Similarly, as seen in Figure 6.4, for  $D_{eq} = 37$  nm, the enhancement is 73%, and for the case of  $D_{eq} = 57$  nm, in Figure 6.5, the enhancement is about 66%. The appearance of the second resonant peak at  $1.63 \times 10^{14}$  rad/s is clear for the case of  $D_{eq} = 37$  nm. This pattern is also observed for  $D_{eq}$  of 10 nm; however, in this case two additional peaks are

apparent at  $1.61 \times 10^{14}$  rad/s and  $1.66 \times 10^{14}$  rad/s, respectively. It is also noted that when  $D_{eq}$  of pores is smaller than 37 nm (for instance,  $D_{eq}=20$  nm (not shown) and for  $D_{eq}=10$  nm), the resonance frequency shifts towards smaller frequencies in porous SiC and the resonance peak occurs at  $1.77 \times 10^{14}$  rad/s. If  $D_{eq}$  is 57 nm, no additional resonant peak or shift in resonance frequency are observed. The enhancement due to near-field radiative transfer decreases as the pore diameter increases from 10 nm to 37 nm and then to 57 nm. Another important factor to consider in a porous medium is the impact of the porosity, defined as the ratio of the pore volume to the entire nominal volume of a porous body [98]. Porosity percent for 10, 37, 57 nm effective sizes was found to be 16%, 46% and 40%, respectively.

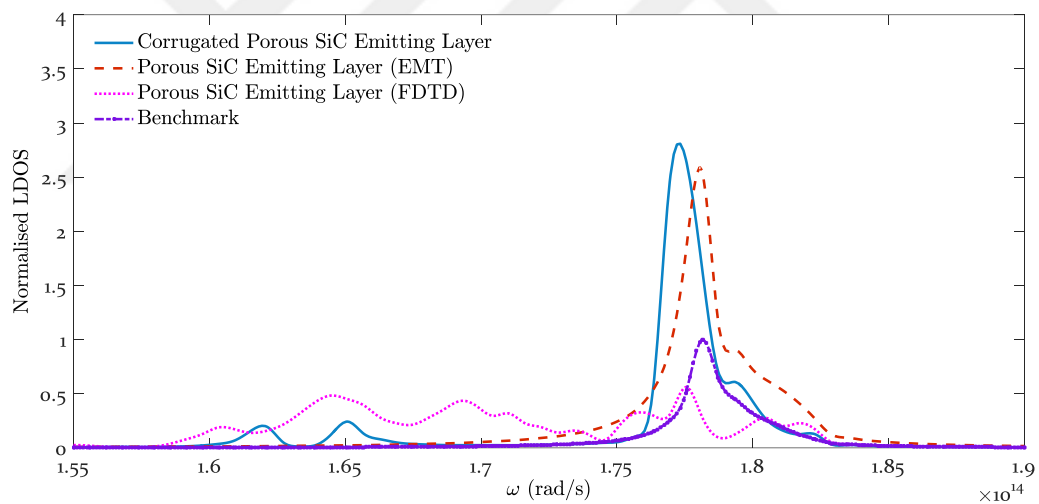
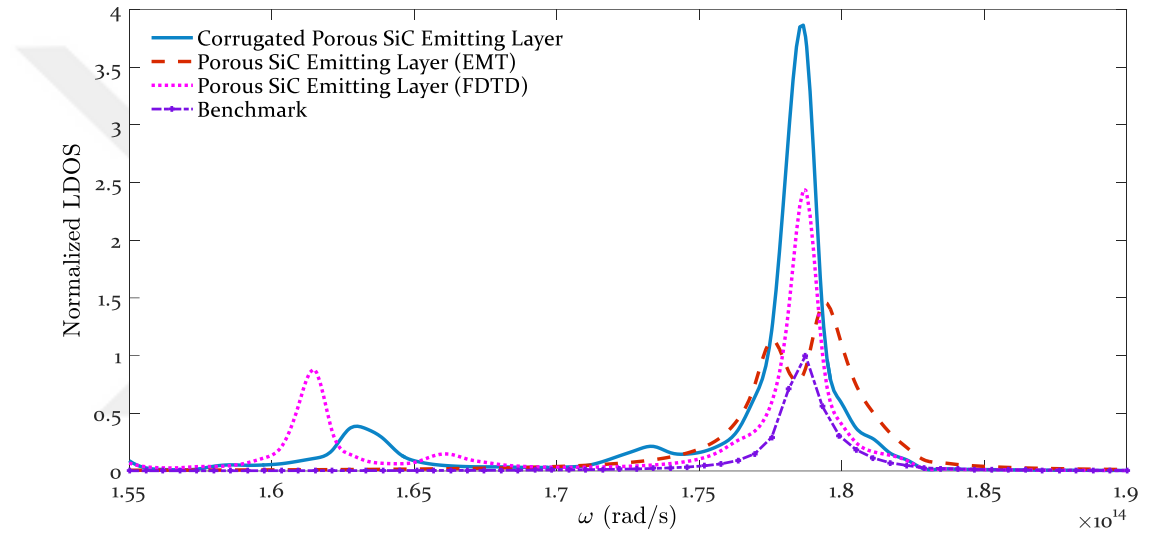


**Figure 6.3** Comparison of LDOS profile for benchmark scenario found through FDTD and EMT analysis for porous SiC emitting layer against corrugated porous emitting layer having  $D_{eq}=10$  nm.

These results clearly reveal the significant deviation between the FDTD and the EMT simulations. It might be concluded that this discrepancy is due to the fact that the conventional EMT is incapable of describing systems where the change in dielectric permittivity from layer to layer is large. This usually happens when the medium is

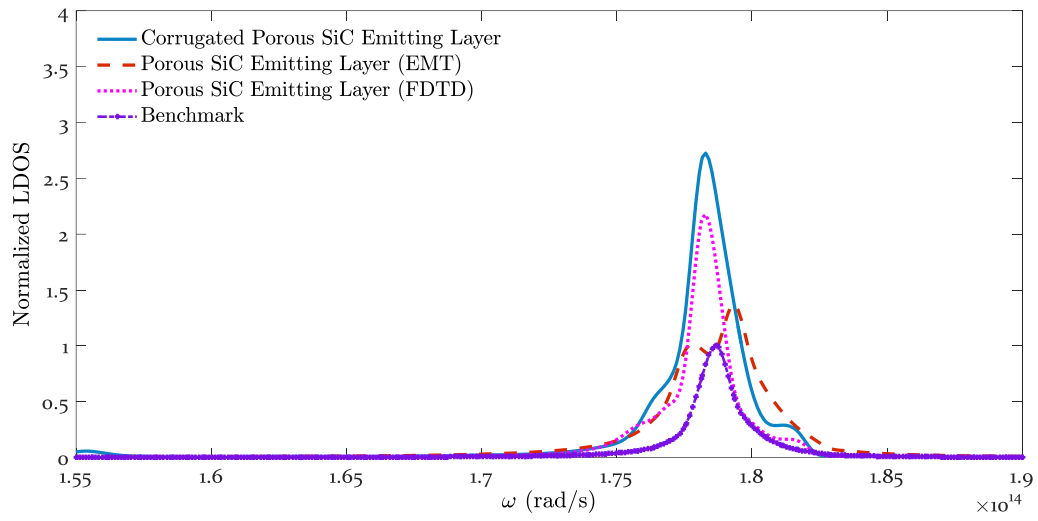
comprised of a metamaterial adjacent to any other medium with a much different permittivity such as vacuum.

Figure 6.6 shows the near-field heat flux profiles at  $T=1000$  K for the benchmark case compared against that where the emitting layer is a corrugated porous SiC with  $D_{eq}=37$  nm. The results are normalized to the peak of the benchmark scenario. We observed that about 75% spectral enhancement can be achieved for near-field heat flux profiles through such configurations.



**Figure 6.4** Comparison of normalized LDOS profiles for benchmark scenario for porous SiC emitting layer against corrugated porous emitting layer having  $D_{eq}=37$  nm as obtained from the FDTD and the EMT simulations.

Figure 6.7 shows the coupling effect of pores which changes the nature of the spectral near-field radiative transfer. As the separation between the nano-pores is changed from 50 nm to 150 nm the second peak diminishes, and at 200 nm separation it becomes invisible. This suggests that the appearance of the secondary and tertiary peaks is due to the coupling of pores' internal cavity resonances with those of surface phonon polaritons due to the nano-gaps between SiC films. Further study of this interaction is needed and being conducted.



**Figure 6.5** Comparisons of the normalized LDOS profiles for the benchmark case and that for the corrugated porous emitting SiC layer with  $D_{eq} = 57$  nm as obtained from the FDTD and the EMT simulations.

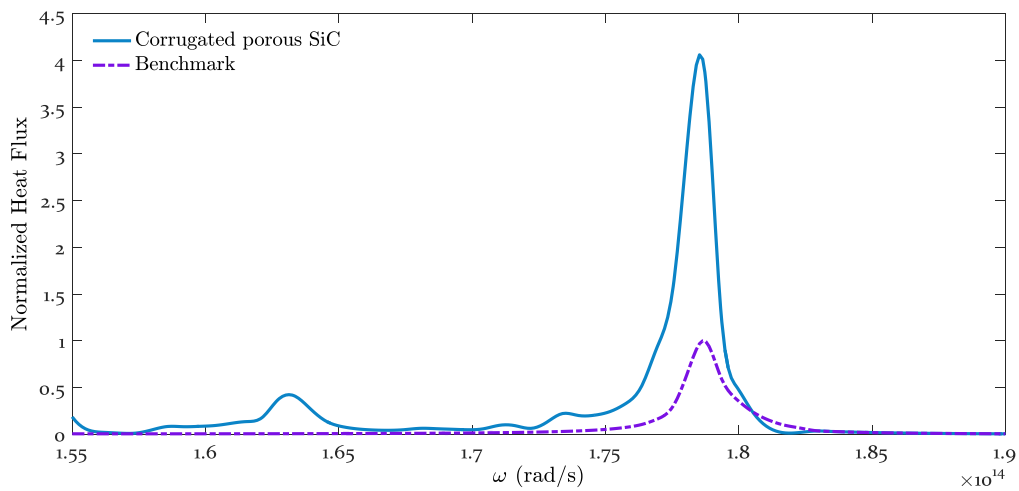


**Figure 6.6** Comparison of normalized heat flux profiles for the benchmark case against that for the corrugated porous SiC emitting layer with  $D_{eq} = 37$  nm.

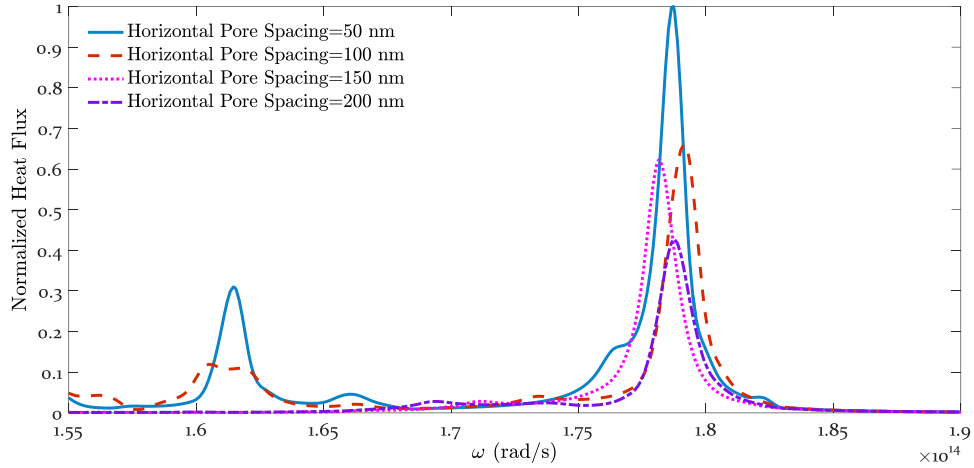


**Figure 6.7** Impact of horizontal pore spacing on normalized heat flux profile ( $D_{eq} = 37$  nm).

## 6.2 Concluding Remarks

In this Chapter, we investigated the behaviors of the LDOS, near-field heat flux and the radiative emission profiles for corrugated, porous as well as both corrugated and porous SiC emitting layers. In our configurations, we considered corrugations by NPs of  $w=500$  nm and  $h=20$  nm and  $D_n=50$  nm. Also pore width  $P_w=50$  nm and pore height  $P_h=30$  nm. These were kept the same everywhere throughout this work. We considered the presence of rectangular corrugations on the surface of thin film and rectangular vacuum inclusions of equivalent diameters of 10, 37 and 57 nm. We report for the first time the presence of additional resonance frequency peaks for corrugated porous SiC emitting layers. The results suggest that mesoporous SiC emitting layer can increase the near-field LDOS and the near-field heat transfer by orders of magnitude. Corrugated mesoporous SiC emitting layers have shown even more enhancement when compared against non-porous SiC used in the same configuration. In addition, they depict an additional resonance peak which can be tuned as a function of pore size and material use. Such mesoporous structures can enhance near-field thermal radiation, which allows the researchers to construct designer mesoporous metamaterials for specific applications for sensing, energy harvesting,



selective nano-scale manufacturing, radiative cooling, heat-assisted magnetic recording, among others.



## CHAPTER VII

### **SPECTRALLY SELECTIVE THERMAL EMISSION BY STRUCTURED SiC-BN MESOPOROUS METAMATERIALS**

In Chapter 6, we presented results for near-field thermal radiation in mesoporous metamaterials. The results showed that when the right combination of pore size and spacing as well as nanoparticle shape and size is used, additional spectral peaks could be observed which could be used in different applications such as thermal sensing. With the insight gained from the work presented in Chapter 6, here we explore a scenario in which we have used the combination of two materials in a double layered structure and have monitored the behavior of LDOS and heat flux from near- to far-field at different local points.

We report here that spectral emission from structured and layered porous metamaterials can be altered by adding a second nano-size layer to the system. The spectral changes are observed in the near- to far-field emission as far as 100  $\mu\text{m}$  above the surface as a function of geometric variations on the films, including nano-size corrugations, pores and layers. The extension of these predictions would allow the researchers to design and construct spectrally selective structures for different sensing and thermal management applications.

#### ***7.1 LDOS in Double Layered Mesoporous SiC-BN Structures***

One of the main inspirations of this work comes from the Nature article by Greffet et al. [73]. They showed that by introducing a periodic microstructure into a polar material (SiC) a thermal infrared source can be fabricated that is coherent over large distances

(many wavelengths) and radiates in well-defined directions. The origin of the coherent emission lies in the diffraction of surface-phonon polaritons (surface waves) by the grating. Surface modes have a wavevector larger than  $2\pi/\lambda$  so that they are evanescent and their effects are not seen in the far-field. However, by ruling a grating on the interface, these surface modes can be coupled to propagating modes.

In [96], Biehs et al. studied the radiative heat flux between nanoporous materials where both layers were air filled porous SiC using EMT-based calculations. In [97], Li et al. showed experimentally that when mesoporous Silica was used for pore sizes between 2-50 nm, the near-field heat flux was enhanced by orders of magnitude compared to non-porous Silica.

In the present study, we report the results for near- field as well as those close-to-far-field spectral radiative emission characteristics of mesoporous SiC-BN metamaterials with nano-scale porosities and corrugations. We explore the impact of both the corrugation and the pore size as well as the porosity (filling factor). Inspired by the work of Greffet et al. [73], we used *NF-RT-FDTD* algorithm to investigate the combined effects of gratings, pores and other structures in detail on near- and far-field thermal emission and heat flux from different materials [88,99-101]. To our knowledge, it is the first time such detailed predictions (based on FDTD method or any other approach) have been reported. Here, this methodology is extended to complex systems, which show promise for further alteration of thermal emission spectra.

The LDOS from a surface at a uniform temperature ( $T=1000$  K, in this work) and radiative flux profiles were given in Chapter 6 for a single SiC emitting film. In the benchmark case, the emitting film is separated by a vacuum gap from a SiC non-emitting layer and the results are compared against those for porous SiC, with nano-size uniform

vacuum inclusions, and corrugated porous SiC emitting layer. Having considered the results of that analysis, we obtained the results for complex structures reported here.

The geometry considered is illustrated in Figure 7.1 (a,b,c). Note that the results for mesoporous double-layer SiC-BN structure with rectangular SiC nanoparticles placed in perfect contact with the top surface are reported the first time. Specific parameters used in the predictions and the results are provided in the following Section.

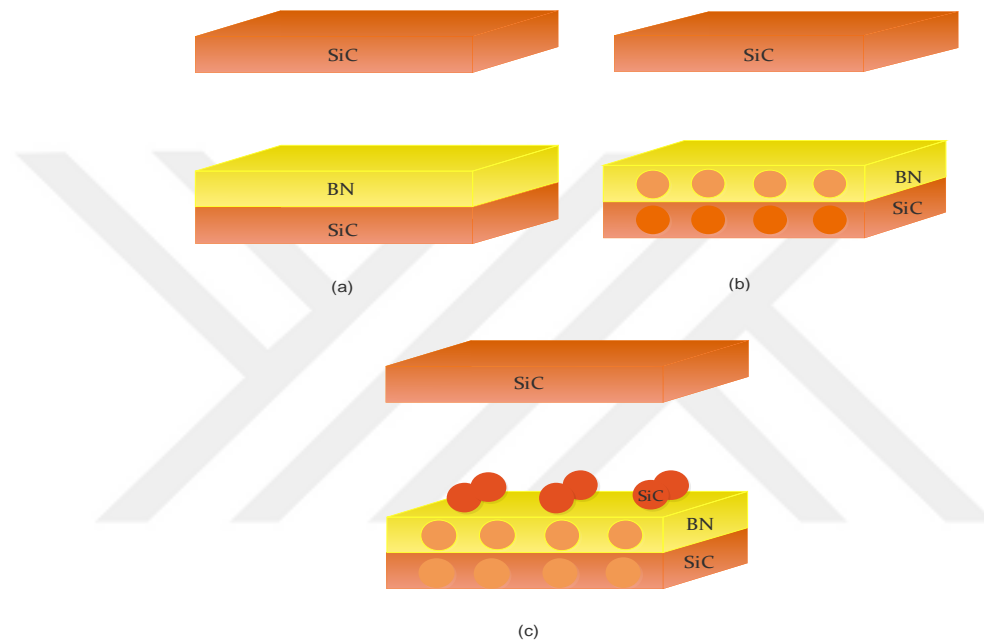


**Figure 7.1** a) Perfectly flat thin double-layer film of SiC-BN. b) Porous SiC-BN double-layer film. c) Corrugated porous SiC-BN double-layer composition with SiC NPs.

Here, we considered structures with the equivalent pore diameters of 33, 50 and 67 nm, where the equivalent diameter was defined as  $D_{eq} = 2ab / (a + b)$ , with  $a$  is the width and  $b$  the height of the pore. As mentioned in Chapter 6, the main reason for this choice of pore sizes is inspired by findings of Li et al. [97]. They discussed that when the diameter of the pore is much smaller than the thermal wavelength, the electromagnetic field across the pore is dominated by the near-field radiation, and the combined thermal conductivities of mesoporous Silica decreases gradually with the pore diameter increasing. Their results and the results we reported in Chapter 6, show that when the

pore's diameter is smaller than 50 nm (mesoporous pores) the enhancement rate is higher than when compared against the case with pore diameters larger than 50 nm. For this reason, we chose the size of the pores (width and height) such that the equivalent diameter would become smaller and larger than 50 nm

In the present calculations, the distance between nanoparticles (NPs) is 50 nm where we assume that they have the width of  $w = 250 \text{ nm}$  and the height of  $h = 250 \text{ nm}$ . Below, we report the results for equivalent pore diameter of 33 nm, for which maximum enhancement was shown, as compared to the results for 50 nm and 67 nm equivalent diameters (not presented here). The horizontal distance between two adjacent pores is assumed 100 nm and the distance between the top of the pores to the interface of the films is considered as 10 nm. We conducted the numerical analysis for flat (benchmark), corrugated and corrugated porous scenarios of a SiC layers and a double-layer composition of SiC-BN, where 50 nm thick BN layer is placed on top of a SiC layer of the same thickness, separated by a nanogap from non-emitting SiC layer. We compared the benchmark results against those for corrugated and porous layer(s). We have used the Drude-Lorentz Permittivity model for SiC and BN in which the longitudinal ( $\omega_{LO}$ ) and transverse ( $\omega_{TO}$ ) optical frequencies of SiC and BN, where  $\omega_{TO} = 1.494 \times 10^{14} \text{ rad/s}$  and  $\omega_{LO} = 1.825 \times 10^{14} \text{ rad/s}$  for SiC and  $\omega_{TO} = 1.97 \times 10^{14} \text{ rad/s}$  and  $\omega_{LO} = 2.44 \times 10^{14} \text{ rad/s}$  for BN.

In Figure 7.2, we provide the results of heat flux comparisons for double-layer SiC-BN composition, at different distances above the surface as well as between adjacent nanoparticles and at the vicinity of the emitting layer. The results show that additional spectral peaks appear when corrugations and pores are added to the structures. As we move from the vicinity of the structure towards the non-emitting layer, the magnitude of the curves drops down. However, the additional peaks are observable even up to 100  $\mu\text{m}$

above the emitting layer. Heat flux is at its maximum value when measured between adjacent NPs and right above the emitting layer (up to 50 nm above the emitting layer) where near-field heat flux exceeds the blackbody limits by three orders of magnitude. However, as we move towards longer distances above the surface, the near-field heat flux values drop below blackbody limit while preserving the additional spectral peaks.

Our main objective here is to identify the most important parameters when tailoring the porous nanostructures in order to obtain spectral enhancement or annihilation of thermal emission for different applications. We have noted several potential contributing factors and their effects on the spectral emission and radiative flux profiles. The choice of the materials is found to be very important since evanescent waves play a crucial role in radiative heat transfer at subwavelength scale when surface waves are excited. We have considered SiC and BN as two polar materials which support surface phonon polaritons. The appearance of the additional resonance peaks and dips as discussed above may be associated with the strong coupling of the pores' cavity resonances with those stemming from the surface phonon polaritons and the fact that the dominance of the p-polarized contribution becomes even greater when having vacuum inclusions.

Our earlier predictions [101] show that when the horizontal distance between the pores is increased, the magnitude of the peaks decreases and eventually the additional peak vanishes when the pores' horizontal spacing reaches and exceeds 150 nm. It is apparent that beyond a given distance, the coupling does not take place, as reported in [101]. Li et al. [97] discussed that when the diameter of pores is much smaller than the thermal wavelength and the electromagnetic field across the pore is dominated by the near-field radiation, the combined thermal conductivity of mesoporous Silica decreases

gradually with the increasing pore diameter. We note that SiC and SiC-BN compositions show a similar behavior in this respect.

Figures 7.2 and 7.3 show the radiative heat flux and LDOS profiles respectively at the vicinity of the emitting layer and at different distances above the surface

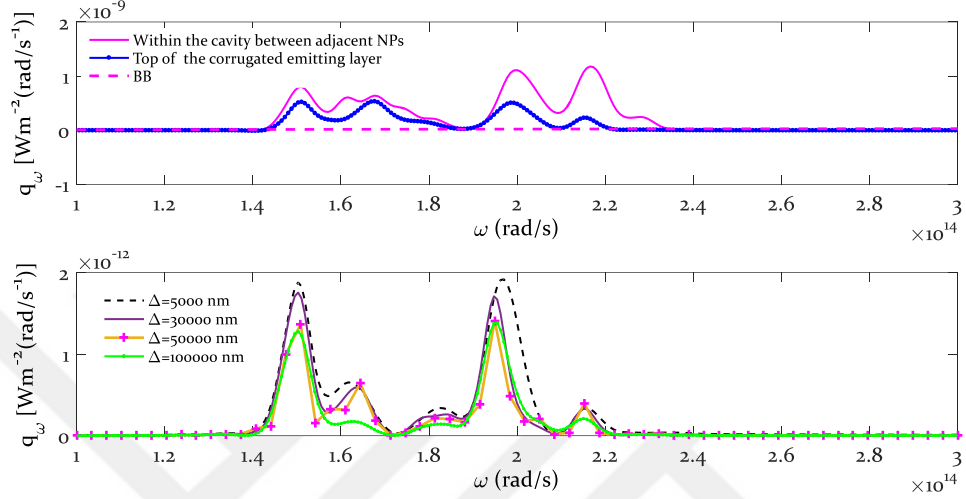


**Figure 7.2** Heat flux profile obtained at different observation points above the emitting layer, for benchmark, porous and corrugated porous SiC-BN layers.

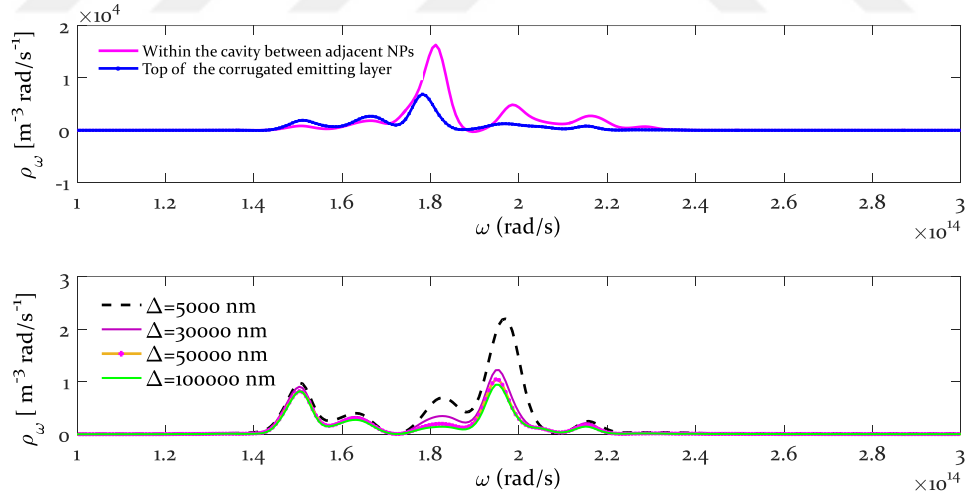


**Figure 7.3** LDOS profile obtained at different observation points above the emitting layer, for benchmark, porous and corrugated porous SiC-BN layers.

Current results show that by modifying the characteristics of the surface profile, it is possible to modify the emissivity of the surface at a given spectrum at distances several wavelengths above the surface (up to 100  $\mu\text{m}$  in our case), as it is possible to

modify the emission spectrum in a given direction [73]. The observed spectral variation seems significant, and can open ways to design metamaterial based new emitters which control and spectrally alter thermal radiation [98, 103-105].

## ***7.2 Concluding Remarks***

In this Chapter, we have investigated the near-to far-field selective thermal emission for a double-layer mesoporous metamaterials. We looked at the spectral behavior of near- to far-field thermal emission in a double-layer thin film of SiC-BN and observed that when corrugations were added to the configuration, additional spectral peaks appear. As we move from the vicinity of the structure towards the non-emitting layer, the magnitude of the curves drops down. However, the additional peaks are observable even up to 100  $\mu\text{m}$  above the emitting layer. Such porous structures can enhance near- to far-field thermal emission, which may allow researchers to design and construct novel nano-porous metamaterials for different applications.



## CHAPTER VIII

### EXTENSION OF THE SOLUTION PROCEDURE TO 3D FDTD

In this Chapter we will discuss into some of the technical details and difficulties of implementation of an FDTD algorithm to 3D geometries using the Matlab (or any other) platform. Most FDTD solutions of electromagnetics problems have been carried out in two dimensions. Our 2D algorithm (e.g. dealing with  $x$  and  $z$  axes, where  $z$  is the direction of propagation) is adequate if we are working on geometries which infinitely repeat in the  $y$  dimension. For instance, when we are analyzing corrugated emitting surfaces, we view their cross-section along the  $xz$  plane. We decided to migrate our Matlab code to 3D in order to express the longer term feasibility of 3D simulations. This exercise was treated as ‘proof of concept’ at this stage due to limited time and resources.

#### ***8.1 The Challenges***

The major challenges with the simulation of a complex 3D structure are (a) the immense memory requirement of representing multiple 3-dimensional arrays and (b) the processing power to deal with the cascade of calculations for every Yee cell of the computational space. While a 500 x 500 cell structure requires an array of 250,000 ‘double’ size numbers in Matlab (or 2 million bytes), the 3D version of this would be a 500x500x500 cell structure i.e. an array of 125,000,000 double precision numbers, taking up 1 billion bytes of memory. In a typical 3D FDTD simulation, upwards of 16 to 18 arrays of this size are needed to hold current and previous field values for the whole geometry, as well as miscellaneous arrays that depend on a specific boundary conditions scheme to be adopted.

Each temporal step -and a simulation could require more than a million steps- will force all of these arrays to be updated.

## ***8.2 The Approach***

For the purpose of this ‘proof of concept’ investigation, we have reduced the problem domain to a manageable size to minimize memory requirements. Furthermore, we explored parallel processing using Matlab’s Parallel Processing Toolbox, as well as GPU (Graphics Processing Unit) code execution.

The system we used is a Hewlett-Packard HP-Z820 workstation, equipped with 2 CPUs of 10 physical and 20 logical cores each. System memory is 32 Gb. Our HP-Z820 is also fitted with a workstation-grade Nvidia GPU, the Quadro K4000 that has 3Gb of very fast internal memory and 768 ‘CUDA’ cores. CUDA (Compute Unified Device Architecture) is a parallel computing platform and programming model created by NVIDIA and implemented by the graphics processing units (GPUs) that they produce.

The GPU cores can be leveraged to undertake processing tasks in parallel. Rather than learning a specialist Nvidia language to achieve this, Matlab has hidden all the technicalities of that behind an accessible set of commands. However, major re-write of our code had to take place in order to take advantage of GPU programming. Using the GPU as opposed to the workstation’s CPU can speed up the running of code by a factor of 6 or 7, depending on the memory requirements. Maximum GPU performance is achieved when all relevant 3D arrays can be accommodated in GPU memory. This way, a complete iteration can take place without the GPU needing to communicate with the computer’s main memory – a slow process. In Figures 8.1 and 8.2 schematics of possible future 3D implementations is given. This effort will define the future efforts.

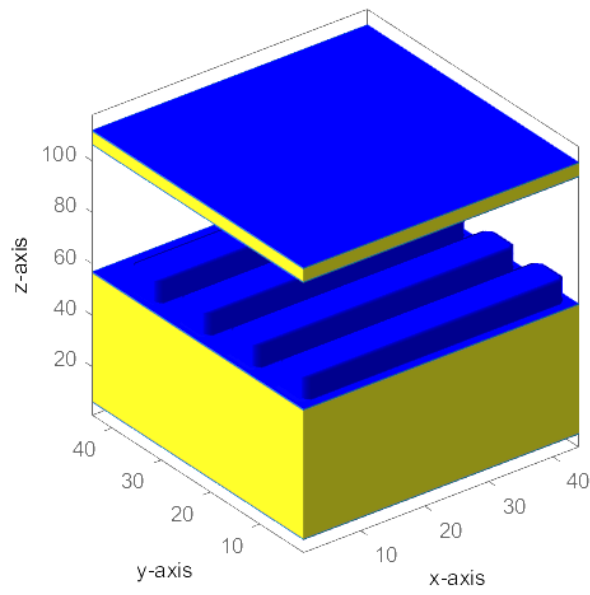


**Figure 8.1** 3D schematics of corrugated bulk emitting layer separated from a thin non-emitting layer

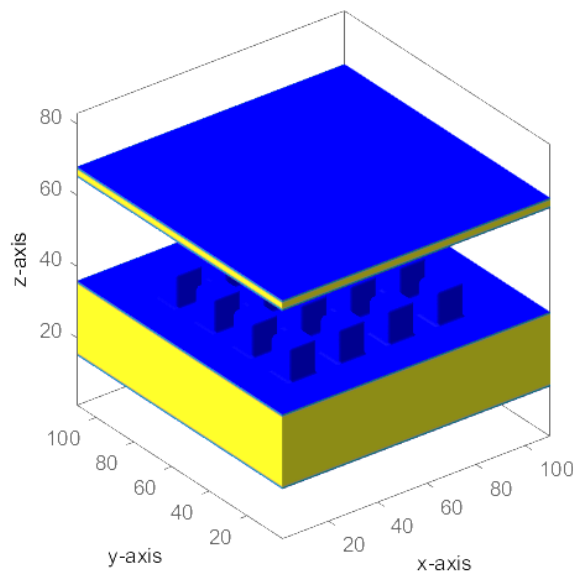


**Figure 8.2** 3D schematics of emitting layers with rectangular nanoparticles separated from a thin non-emitting layer.

## CHAPTER IX

### CONCLUSIONS AND FUTURE WORK

In this dissertation, we have extensively studied the near-field of thermal radiation in metamaterials where the geometric size is much smaller than the wavelength of thermal radiation. In the nano-scale regime, radiation transfer is enhanced when surfaces supporting Surface Phonon Polaritons (SPhPs) are brought into close vicinity of each other. We have explained step by step developed procedures of the *NF-RT-FDTD* algorithm which is a numerical methodology designed specifically for the solutions of near-field thermal radiation problems between structured surfaces separated by nano-scale gaps.

#### ***9.1 Concluding Remarks***

After a literature review in Chapter 1, in Chapter 2, we have provided definitions and formulations of near-field thermal radiation based finite difference time domain analysis (FDTD) method for the calculation of the polariton-enhanced near-field thermal radiation emission based on the local density of electromagnetic states (LDOS). We have shown that the Green tensor function can be obtained using the FDTD method and the LDOS expression can be derived from the Green tensor function. The geometry and the methodology are discussed, and the limitations and advantages of the FDTD method are explained.

In Chapter 3, we observed that when considering the effects of surface phonon polaritons, a time domain computational method such as FDTD needs to be followed for numerical dispersion, absorbing boundary conditions and an accurate permittivity model.

Hence making the simulations very expensive and sometimes impossible; Yet, it is possible to overcome these difficulties.

We observed that when working with plasmonic materials, the permittivity of the material not only had an effect inside the material but also on the grid points adjacent to the material itself. Hence, handling the grid sizes as well as the boundaries in a multilayer structure as the one presented in this work are of vital importance for the robustness of the solution methodology. Comparisons made between the analytical and current FDTD analysis of the Drude-Lorentz permittivity model show an excellent agreement.

Results presented in Chapter 3 suggest that the CPML is the optimum boundary condition in using the FDTD method to analyze more complex geometries (e.g. analysis of near field thermal radiation between a tip and a sphere) for which an analytical solution may not be achievable. This boundary condition hence allows more streamlined simulations to be carried out when working with sub-wavelength structures. The diversity of geometries considered and the physical systems analyzed will be significantly increased with this approach, allowing a clearer impact to the development of novel nano-diagnostics and nano-manufacturing modalities. The exact size of the CPML layers, as well as the CPML parameters, for the different geometries (SiC layer and gap thicknesses) can only be found empirically at this stage.

Future work is to be carried out to identify the causes of the small high-pass/ low-pass discrepancies of the LDOS response around the resonance frequency.

In Chapter 4, we have shown the developed of *NF-RT-FDTD* to model arbitrary shape nanoparticles and have evaluated their impact on LDOS as well as in heat flux profile. The results show an increase in the magnitude of LDOS with an increase in the periodicity of the nano-gratings, when the distance between the gratings is much smaller than the wavelength of interest. In the case of 25 elliptical NPs each 60 nm apart from

each other when each ellipse had a  $w=600\text{ nm}$  and  $h=20\text{ nm}$ , 71% enhancement was observed when compared with the benchmark scenario in which no NPs were present at the surface of the emitting layer. We also observed that when  $d_n < 0.005\lambda$  ( $\lambda = 1059\text{ nm}$ ) we obtained maximum enhancement of LDOS.

We evaluated the impact of the arbitrary shape nano-gratings and observed that rectangles showed the greatest impact on enhancement of LDOS and heat flux value when compared against ellipses and triangles of the same sizes. Enhancement of near-field flux at different temperatures due to the presence of the elliptic NPs could be clearly seen when compared against the benchmark scenario in which no NPs were present.

We extended the FDTD computational approach to describe near-field radiative transfer between corrugated surfaces separated by nano-scale gaps in Chapter 4. The premise of these calculations is that LDOS varies both in normal and lateral directions, making the problem a two, or more correctly, a three-dimensional one even for one-dimensional near-field calculations. This means that LDOS profiles above nanostructure varies along with LDOS profiles to the right or the left of a structure. Depending on the size and shape of the structures the local near field radiative transfer is bound to change. This is expected, as due to the wave nature of the EM energy exchange, interference effects are to come into picture. Our results show that depending on the particle configurations, periodicity, shape and size we see both enhancement and decrease in the local flux profiles.

In Chapter 5, the results presented showed that the presence of NPs on the surface of an emitting layer increases the magnitude of LDOS and the radiative flux, within specific spectral bands by several orders of magnitude. A noticeable amount of discrepancy was also observed when the results obtained with EMT were compared against those obtained with the *NF-RT-FDTD* algorithm in the presence of the NPs. Note

that the methodology presented here to determine NFRT between corrugated surfaces is much more fundamental than a simpler EMT, which does not seem to be accurate at nano-scale resolutions. With the insight gained from these modeling efforts, we should be able to explore corrugated geometries, specifically targeting near-field enhancements or annihilations.

In Chapter 6, we investigated the variations of the LDOS, near-field heat flux and the radiative emission profiles for corrugated, porous as well as both corrugated and porous SiC emitting layers. In our configurations, we considered corrugations by NPs of  $w=500$  nm and  $h=20$  nm and  $D_n=50$  nm. Also, pore width  $P_w=50$  nm and pore height  $P_h=30$  nm. These were kept the same everywhere throughout this work. We considered the presence of rectangular corrugations on the surface of thin film and rectangular vacuum inclusions of equivalent diameters of 10, 37 and 57 nm.

We report, for the first time in the literature, the presence of additional resonance frequency peaks for corrugated porous SiC emitting layers. The results suggest that mesoporous SiC emitting layer can increase the near-field LDOS and the near-field heat transfer by orders of magnitude. Corrugated mesoporous SiC emitting layers have shown even more enhancement when compared against non-porous SiC used in the same configuration. In addition, they depict an additional resonance peak which can be tuned as a function of pore size and material use. Such mesoporous structures can enhance near-field thermal radiation, which allows the researchers to construct designer mesoporous metamaterials for possible applications for sensing, energy harvesting, selective nano-scale manufacturing and radiative cooling.

In Chapter 7, we have investigated the near-to far-field selective thermal emission for a double-layer mesoporous metamaterials. We considered the spectral behavior of near- to far-field thermal emission in a double-layer thin film of SiC-BN and observed

that when corrugations were added to the configuration, additional spectral peaks appear. As we move from the vicinity of the structure towards the non-emitting layer, the magnitude of the curves drops down. However, the additional peaks are observable even up to 100  $\mu\text{m}$  above the emitting layer. Such porous structures can enhance near- to far-field thermal emission, which may allow researchers to design and construct novel nanoporous metamaterials.

In Chapter 8, we discussed possible challenges and our proposed approach to overcome them for the 3D implementation of the *NF-RT-FDTD* algorithm.

## ***9.2 Future Work***

Based on the predictions obtained with the current studies using the 3D *NF-RT-FDTD* algorithm, it would be possible to explore more complicated geometries with variety of applications. In an on-going work, the primary objective has been designing, constructing and fabricating a test sample, which essentially mimics thermophotovoltaic energy conversion principles. The test sample is a sandwich-like structure [22], and it is to be packaged such that it encloses vacuum inside, where the phononic effects will take place and near-field thermal radiation will occur. Fabrication stage involves standard semiconductor processes and they will be performed at the National Nanotechnology Research Center (UNAM) at Bilkent University in Ankara, and EVGroup in Austria. The ultimate objective of this particular project is to end up with a prototype of near-field thermophotovoltaics device, through which the near-field thermal radiation is measurable and differentiable from the heat conduction and convection mechanisms. The numerical part of this project covered the modeling of the near-field radiative heat transfer between two perfectly smooth plates in parallel configuration, and this task has been achieved through the use of the *NF-RT-FDTD* algorithm developed in this dissertation.



Nature has always been the source of inspiration for human beings and biologically inspired models has let scientists to great discoveries in all fields. For instance, *Morpho* butterflies with their blue or light-purple iridescence nature have inspired researchers from different backgrounds to investigate their structure. Different fabrication techniques have been developed to model the structures of *Morpho* butterflies [106–111] with the intention to enhance the efficiency of solar cells [110–112]. Advancing *NF-RT-FDTD* algorithm to model biologically inspired structured for near-field thermal radiation applications would be a possible extension to this dissertation as a future work.



## BIBLIOGRAPHY

- [1] W. Weber, *Elektrodynamische Maasbestimmungen*, Abh. Leibnizens Ges., Leipzig, 1846.
- [2] G. Kirchhoff, “On the motion of electricity in wires,” *Philos. Mag.*, **13**:393-412, 1857.
- [3] J. C. Maxwell, *A Treatise on Electricity and Magnetism, i and ii*, Oxford University Press, 1873.
- [4] A. M. Ampere, *Mathematique Des Phenomenes Electro-Dynamiques, Uniquement Diduite de Lexpirience*, A. Blanchard, Paris, 1883.
- [5] J. Stefan, “Über die Beziehung zwischen der Wärmestrahlung und der Temperatur,” *Sitzungsberichte der mathematisch-naturwissenschaftlichen Classe der kaiserlichen Akademie der Wissenschaften*, vol. 79, no. 2. pp. 391–428, 1879.
- [6] L. Boltzmann, “Über die Eigenschaften Monocyklischer und andere damit verwandter Systeme,” *Crelles Journal*, 98: 68–94; in WA III, paper 73, 1884.
- [7] W. Wien, “Ueber die Fragen, welche die translatorische Bewegung des Lichtäthers betreffen,” *Ann. D. Phys.*, 65, 1898.
- [8] M. Planck, *Vorlesungen Über die Theorie der Warmestrahlung*, Barth, Leipzig, 1906.
- [9] I. Müller, *A History of Thermodynamics*, Springer, 2007.
- [10] S. M. Rytov, *Theory of Electrical Fluctuation and Thermal Radiation*, Academy of Science of USSR Publishing, Moscow, 1953.
- [11] D. Polder, M. Van Hove, “Theory of radiative heat transfer between closely spaced bodies,” *Phys. Rev. B* 4 (10) 3303–3314, 1971.
- [12] G. Chen, *Nanoscale Energy Transport and Conversion*, Oxford University, 2005.
- [13] Z. Zhang, *Nano/Microscale Heat Transfer*, McGraw Hill, 2007.
- [14] J. R. Howell, M. P. Mengüç, R. Siegel, *Thermal Radiation Heat Transfer*, 6<sup>th</sup> Edition, CRC Press, 2016.
- [15] R. S. DiMatteo, P. Greiff, S. L. Finberg, K. A. Young-Waithe, H. K. H. Choy, M. M. Masaki, and C. G. Fonstad, “Enhanced Photogeneration of Carriers in a Semiconductor via Coupling Across a Nonisothermmal Nanoscale Vacuum Gap,” *Applied Physics Letters*, vol. 79, no. 12, pp. 1894–1896, 2001.

- [16] A. Kittel, W. Müller-Hirsch, J. Parisi, S.-A. Biehs, D. Reddig, and M. Holthaus, “Near-Field Radiative Heat Transfer in a Scanning Thermal Microscope,” *Physical Review Letters*, vol. 95, pp. 224301, 2005.
- [17] L. Hu, A. Narayanaswamy, X. Y. Chen, and G. Chen, “Near-Field Thermal Radiation Between Two Closely Spaced Glass Plates Exceeding Planck’s Blackbody Radiation Law,” *Applied Physics Letters*, vol. 92, no. 13, pp. 133106–133106-3, Mar 2008.
- [18] S. Shen, A. Narayanaswamy, and G. Chen, “Surface Phonon Polaritons Mediated Energy Transfer Between Nanoscale Gaps,” *Nano Letters*, vol. 9, no. 8, pp. 2909–2913, 2009.
- [19] A. Narayanaswamy, “Investigation of Nanoscale Thermal Radiation: Theory and Experiments,” Ph.D. Thesis, MIT, Cambridge, 2007.
- [20] A. Narayanaswamy, S. Shen, L. Hu, X. Y. Chen, and G. Chen, “Breakdown of the Planck Blackbody Radiation Law at Nanoscale Gaps,” *Applied Physics A: Materials Science and Processing*, vol. 96, no. 2, pp. 357–362, 2009.
- [21] E. Rousseau, A. Siria, G. Jourdan, S. Volz, F. Comin, J. Chevrier, and J.-J. Greffet, “Radiative Heat Transfer at the Nanoscale,” *Nature Photonics*, vol. 3, no. 9, pp. 514–517, 2009.
- [22] K. D. Webb, Z. Artvin, F. K. Khosroshahi , H. Ertürk , T. Okutucu, and M. P. Mengüç, “Near-Field Radiative Heat Transfer Measurements Between Parallel Plates,” *RAD 13: Seventh International Symposium on Radiative Transfer*, 2013.
- [23] R. S. Ottens, V. Quetschke, S. Wise, A. A. Alemi, R. Lundock, G. Mueller, D.H.Reitze, D. B. Tanner, and B. F. Whiting, “Near-Field Radiative Heat Transfer Between Macroscopic Planar Surfaces,” *Physical Review Letters*, vol. 107, no. 1, Jun 2011.
- [24] K. Joulain, J.-P. Mulet, F. Marquier, R. Carminati, J.-J. Greffet, “Surface electromagnetic waves thermally excited: Radiative heat transfer, coherence properties and Casimir forces revisited in the near field,” *Surface Science Reports* 57 (3) 59-112, 2005.
- [25] K. Joulain, R. Carminati, J.-P. Mulet, J.-J. Greffet, “Definition and measurement of the local density of electromagnetic states close to an interface,” *Phys. Rev. B* 68 (24) 245405, 2003.
- [26] A. Shchegrov, K. Joulain, R. Carminati, J. Greffet, “Near-field spectral effects due to electromagnetic surface excitations,” *Phys. Rev. Lett.* 85 (7) 1548–1551, 2000.

- [27] J. B. Pendry, “Radiative exchange of heat between nanostructures,” *J. Phys. Condens. Matter* 11 (35) 6621–6633, 1999.
- [28] C. Hargreaves, “Anomalous radiative transfer between closely-spaced bodies,” *Phys. Lett. A* 30 (9) 491–492, 1969.
- [29] F. Gervais, B. Piriou, “Temperature dependence of transverse and longitudinal optic modes in the a and b phases of quartz,” *Phys. Rev. B* 11 (10) 3944–3950, 1975.
- [30] E. Rousseau, A. Siria, G. Jourdan, S. Volz, F. Comin, J. Chevrier, J.-J. Greffet, “Radiative heat transfer at the nanoscale,” *Nat. Photon.* 3 (9) 514–517, 2009.
- [31] Y. Kajihara, K. Kosaka, S. Komiyama, “A sensitive near-field microscope for thermal radiation,” *Rev. Sci. Instrum.* 81 (3) 033706, 2010.
- [32] Y.D. Wilde, F. Formanek, R. Carminati, B. Gralek, P. Lemoine, K. Joulain, J. Mulet, Y. Chen, J. Greffet, “Thermal radiation scanning tunneling microscopy,” *Nature* 444 740–743, 2006.
- [33] A. Kittel, U.F. Wischnath, J. Welker, O. Huth, F. Ruting, S.-A. Biehs, “Near-field thermal imaging of nanostructured surfaces,” *Appl. Phys. Lett.* 93 (19) 193109, 2008.
- [34] M. Francoeur, M. P. Mengüç, and R. Vaillon, “Local Density of Electromagnetic States within a Nanometric Gap Formed Between Thin Films Supporting Surface Phonon Polaritons”, *Journal of Applied Physics* 107(3), pp. 034313–034313-8, 2010.
- [35] C. Van Vlack, “Dyadic Green Functions and Their Applications in Classical and Quantum Nanophotonics”, Ph.D. Thesis, Queen’s University, Canada, 2012.
- [36] A. Taflove, and S. C. Hagness, *Computational Electrodynamics: The Finite-Difference Time-Domain Method*, 3rd ed., Norwood, MA: Artech, 2005.
- [37] K. S. Kunz, and R. J. Luebbers, *The Finite-Difference Time-Domain Method for Electromagnetics*, Boca Raton, FL: CRC Press, 1993.
- [38] D. M. Sullivan, *Electromagnetic Simulation Using the FDTD Method*, New York, NY: Wiley–IEEE Press, 2000.
- [39] W. Yu, R. Mittra, T. Su, Y. Liu, and X. Yang, *Parallel Finite-Difference Time-Domain Method*, Norwood, MA: Artech, 2006.
- [40] J. Jin, *The Finite Element Method in Electromagnetics*, 2<sup>nd</sup> ed., New York: Wiley–IEEE Press, 2002.
- [41] K. Yasumoto, ed., *Electromagnetic Theory and Applications for Photonic Crystals*, Boca Raton, FL: CRC Press, 2005.
- [42] S. Rao, D. Wilton, and A. Glisson, “Electromagnetic scattering by surfaces of arbitrary shape,” *IEEE Trans. Antennas and Propagation*, vol. 30, pp. 409–418, 1982.

- [43] K. Umashankar, A. Taflove, and S. Rao, "Electromagnetic scattering by arbitrary shaped threedimensional homogeneous lossy dielectric objects," *IEEE Trans. Antennas and Propagation*, Vol. 34, pp. 758–766, 1986.
- [44] M. Bonnet, *Boundary Integral Equation Methods for Solids and Fluids*, New York: Wiley, 1999.
- [45] W. C. Chew, J.-M. Jin, E. Michielssen, and J. Song, eds., *Fast and Efficient Algorithms in Computational Electromagnetics*, Norwood, MA: Artech, 2000.
- [46] M. Born and E. Wolf, *Principles of Optics*, New York: Pergamon Press, 1975.
- [47] M. G. Moharam and T. K. Gaylord, "Rigorous coupled-wave analysis of planar-grating diffraction," *J. Opt. Soc. Am.*, vol.71, pp. 811-818, 1981.
- [48] Farhad Kazemi Khosroshahi, H. Ertürk, M. P. Mengüç, "spectrally selective Si/SiO<sub>2</sub> based filters for thermophotovoltaic devices," in *Proceedings of the 8th International Symposium on Radiative Transfer, Cappadocia, June 6-10, 2016*.
- [49] E. M. Purcell and C. R. Pennypacker, "DDA Basics," *Astrophys. J.*, vol. 186, pp. 705–714, 1973.
- [50] V. L. Y. Loke, M. P. Mengüç, and T. a. Nieminen, "Discrete-dipole approximation with surface interaction: Computational toolbox for MATLAB," *J. Quant. Spectrosc. Radiat. Transf.*, vol. 112, no. 11, pp. 1711–1725, 2011.
- [51] S. Talebi Moghaddam, H. Ertürk, and M. P. Mengüç, "Enhancing local absorption patterns within gold nanostructures on a dielectric surface under an AFM probe and with evanescent-wave illumination," *J. Quant. Spectrosc. Radiat. Trans.*, Vol 178, page 124 - 133, 2016.
- [52] S. Talebi Moghaddam, H. Ertürk, and M. P. Mengüç, "Effect of silicon AFM probe location on absorption profile of gold nano-structures on a dielectric surface," in *Proceedings of the 8th International Symposium on Radiative Transfer, Cappadocia, June 6-10, 2016*.
- [53] M. A. Yurkin and M. Huntemann, "Rigorous and Fast Discrete Dipole Approximation for Particles near a Plane Interface," *J. Phys. Chem. C*, vol. 119, no. 52, pp. 29088–29094, 2015.
- [54] S. Edalatpour and M. Francoeur, "The Thermal Discrete Dipole Approximation (T-DDA) for near-field radiative heat transfer simulations in three-dimensional arbitrary geometries," *Journal of Quantitative Spectroscopy and Radiative Transfer*, vol. 133, pp. 364-373, 2014.

- [55] S. Edalatpour, M. Cuma, T. Trueax, R. Backman, and M. Francoeur, “Convergence analysis of the thermal discrete dipole approximation,” *Physical Review E*, vol. 91, 063307, 2015.
- [56] V. M. Agranovich and D. L. Mills, ed. *Surface Polaritons: Electromagnetic Waves at Surfaces and Interfaces*, Amsterdam, New York: North-Holland, 1982.
- [57] K. Huang, “Lattice vibrations and optical waves in ionic crystals,” *Nature*, 167:779-780, 1951.
- [58] K. Huang, “On the interaction between the radiation field and ionic crystals,” *Proceedings of the Royal Society of London. Series A, Mathematical and Physical Sciences*, 208 (1094): 352-365, 1951.
- [59] Gang Chen, *Nanoscale energy transport and conversion: a parallel treatment of electrons, molecules, phonons, and photons*. Oxford University Press, USA, 2005.
- [60] Kane Yee, “Numerical Solution of Initial Boundary Value Problems Involving Maxwell's Equations in Isotropic Media”, *IEEE Transactions on Antennas and Propagation*, vol. 14, no. 3, pp. 302–307, 1966.
- [61] C. Van Vlack, “Dyadic Green Functions and Their Applications in Classical and Quantum Nanophotonics,” Ph.D. Thesis, Queen’s University, Canada, 2012.
- [62] J. R. Howell, R. Siegel, and M. P. Menguc, *Thermal Radiation Heat Transfer*, CRC Press, 2011.
- [63] A. Taflove, S. C. Hagness, *Computational Electrodynamics: The Finite-Difference Time Domain Method*, Artech House, 2000.
- [64] J. B. Schneider, *Understanding the Finite-Difference Time-Domain Method*. Available: <http://www.eecs.wsu.edu/~schneidj/ufdtd> , 2012.
- [65] G. Mur, “Absorbing Boundary Conditions for the Finite-Difference Approximation of the Time-Domain Electromagnetic-Field Equations,” *IEEE Transactions on Electromagnetic Compatibility*, vol. EMC-23, no.4, pp.377-382, 1981.
- [66] K. K. Mei and J. Fang, “Superabsorption – a method to improve absorbing boundary conditions,” *IEEE Trans. Antennas and Propagation*, vol. 40, no. 9, pp. 1001-1010, 1992.
- [67] J. Berenger, “A perfectly matched layer for the absorption of electromagnetic waves,” *J. Comput. Phys*, vol. 114, no. 2, pp. 185–200, 1994.
- [68] M. Kuzuoglu and R. Mittra, “Frequency dependence of the constitutive parameters of causal perfectly matched anisotropic absorbers,” *IEEE Microw.* vol. 6, pp. 447-449, 1996.

- [69] S. D. Gedney, *The Perfectly Matched Layer Absorbing Medium, in Advances in Computational Electrodynamics: The Finite Difference Time Domain*, Artech House, Boston, pp. 263-340, 1998.
- [70] C. D. Sarris, “Adaptive Mesh Refinement for Time-Domain Numerical Electromagnetics,” *Synthesis Lectures on Computational Electromagnetics*, vol.1, no. 1, pp. 1–154, 2007.
- [71] H. Mutschke, A. C. Andersen, D. Clément, Th. Henning & G. Peiter, “Infrared properties of SiC particles,” *Astron. Astrophys.* 345, 187-202, 1999.
- [72] Soumyadipta Basu, “Near-field radiative energy transfer at nanometer distances,” Ph.D. Thesis, Georgia Institute of Technology, Georgia, 2009.
- [73] J. J. Greffet, R. Carminati, K. Joulain, J. P. Mulet, S. Mainguy, and Y. Chen, “Coherent emission of light by thermal sources,” *Nature* 416, 61–64, 2002.
- [74] V. M. Shalaev, “Optical Negative-Index Metamaterials,” *Nat. Photonics*, 1, pp. 41–48, 2007.
- [75] M. Noginov, M. Lapine, V. Podolskiy and Y. Kivshar, “Focus Issue: Hyperbolic Metamaterials,” *Opt. Express* 21, pp. 14895–14897, 2013.
- [76] X. L. Liu, and Z. M. Zhang, “Metal-Free Low-Loss Negative Refraction in the Mid-Infrared Region,” *Appl. Phys. Lett.*, 103, p. 103101, 2013.
- [77] J. Yao, Z. W. Liu, Y. M. Liu, Y. Wang, C. Sun, G. Bartal, A. M. Stacy and X. Zhang, “Optical Negative Refraction in Bulk Metamaterials of Nanowires,” *Science* 321, p. 930, 2008.
- [78] Z. Jacob, L. V. Alekseyev and E. Narimanov, “Optical Hyperlens: Far-Field Imaging Beyond the Diffraction Limit,” *Opt. Express* 14, pp. 8247–8256, 2006.
- [79] Z. W. Liu, H. Lee, Y. Xiong, C. Sun, and X. Zhang, “Far-Field Optical Hyperlens Magnifying Sub-Diffraction-Limited Objects,” *Science* 315, p.1686, 2007.
- [80] X. L. Liu, L. P. Wang, and Z. M. Zhang, “Wideband Tunable Omnidirectional Infrared Absorbers Based on Doped-Silicon Nanowire Arrays,” *ASME J. Heat Transfer*, 135(6), p. 061602, 2013.
- [81] T. C. Choy, *Effective Medium Theory: Principles and Applications*, Oxford University, Oxford, UK, 1999.
- [82] B. Liu, and S. Shen, “Broadband Near-Field Radiative Thermal Emitter/Absorber Based on Hyperbolic Metamaterials: Direct Numerical Simulation by the Wiener Chaos Expansion Method,” *Phys. Rev. B*, 87, p. 115403, 2013.

- [83] M. Tschikin, S. A. Biehs, R. Messina, and P. Ben-Abdallah, "On the Limits of the Effective Description of Hyperbolic Materials in the Presence of Surface Waves," *J. Opt.*, 15, p. 105101, 2013.
- [84] S. A. Biehs, P. Ben-Abdallah, F. S. S. Rosa, K. Joulain and J. J. Greffet, "Nanoscale Heat Flux Between Nanoporous Materials," *Opt. Express* 19, pp. A1088–A1103, 2011.
- [85] X. L. Liu, T. J. Bright, and Z. M. Zhang, "Application Conditions of Effective Medium Theory in Near-Field Radiative Heat Transfer Between Multilayered Metamaterials," *Journal of Heat Transfer*, Vol. 136, p. 092703-1/8, 2014.
- [86] A. Didari, M. P. Mengüç, "Near-field thermal emission between corrugated surfaces separated by nano-gaps," in *Proceedings of Nanoscale and Microscale Heat Transfer IV, Eurotherm 103*, 28-31, 2014.
- [87] A. Didari, M. P. Mengüç, "Analysis of near-field radiation transfer within nano-gaps using FDTD method," *Journal of Quantitative Spectroscopy and Radiative Transfer* 146, 214-226, 2014.
- [88] A. Didari, M. P. Mengüç, "Near-Field Thermal Emission between Corrugated Surfaces separated by Nano-Gaps," *Journal of Quantitative Spectroscopy and Radiative Transfer* 158, 43-51, 2015.
- [89] Krishna K. Sharma, Ankush V. Biradar, Sayantani Das, Tewodros Asefa, "Bifunctional mesoporous silica catalyst for C–C bond forming tandem reactions," *Eur. J. Inorg. Chem.*, 3174–3182, 2011.
- [90] Sheng jun Huang, Kenji Hara, Atsushi Fukuoka, "Intrinsic catalytic role of mesoporous silica in preferential oxidation of carbon monoxide in excess hydrogen," *Chem. Eur. J.* 18, 4738–4747, 2012.
- [91] J. Deere, E. Magner, J. G. Wall, B. K. Hodnett, "Adsorption and activity of proteins onto mesoporous silica," *Catal.Lett.* 85,1–2, 2003.
- [92] A. J. Di Pasqua, S. Wallner, D. J. Kerwood, J. C. Dabrowiak, "Adsorption of the PtII anticancer drug carboplatin by mesoporous silica," *Chem. Biodivers.* 6(9) 1343–1349, 2009.
- [93] Zheng Wang, Dongmei Fang, Qing Li, Lingxia Zhang, Rong Qian, Yan Zhu, Haiyun Qu, Yiping Du, "Modified mesoporous silica materials for on-line separation and preconcentration of hexavalent chromium using a microcolumn coupled with flame atomic absorption spectrometry," *Anal. Chim. Acta* 725, 81–86, 2012.



- [94] Min Zhang, Yipan Wu, Xizeng Feng, Xiwen He, Langxing Chen, Yukui Zhang, “Fabrication of mesoporous silica-coated CNTs and application in size-selective Protein separation,” *J. Mater. Chem.* **20** 5835–5842, 2010.
- [95] Dongyuan Zhao, Jinyu Sun, Quanzhi Li, Galen D. Stucky, “Morphological control of highly ordered mesoporous silica SBA-15,” *Chem. Mater.* **12**, 275–279, 2000.
- [96] S. A. Biehs, P. Ben-Abdallah, F. S. S. Rosa, K. Joulain & J. J. Greffet, “Nanoscale heat flux between nanoporous materials,” *Opt. Express* **19** (105), A1088-A1103, 2011.
- [97] J. Li, Y. Feng, X. Zhang, C. Huang and G. Wang, “Near-field radiative heat transfer across a pore and its effects on thermal conductivity of mesoporous silica,” *Phy. B-Condensed Matter* **456**, 237-243, 2015.
- [98] P. Liu and G. F. Chen, *Porous Materials: Processing and Applications*, Elsevier, 2014.
- [99] A. Didari, M. P. Mengüç, “Near-field thermal emission between corrugated surfaces separated by nano-gaps,” *Journal of Quantitative Spectroscopy and Radiative Transfer* **158**, 43-51, 2015.
- [100] A. Didari and M. P. Mengüç, “Near to far-field coherent thermal emission by surfaces coated by nanoparticles: evaluation of effective medium theory,” *Opt. Express* **23** (11), A547-A552, 2015.
- [101] A. Didari and M. Pinar Mengüç, “Near-field thermal radiation transfer by mesoporous metamaterials,” *Opt. Express* **23**, A1253-A1258, 2015.
- [102] S. A. Biehs, P. Ben-Abdallah, F. S. S. Rosa, K. Joulain and J. J. Greffet, “Nanoscale heat flux between nanoporous materials,” *Opt. Express* **19** (105), A1088-A1103, 2011.
- [103] J. Li, Y. Feng, X. Zhang, C. Huang, & G. Wang, “Near-field radiative heat transfer across a pore and its effects on thermal conductivity of mesoporous silica,” *Phy. B-Condensed Matter* **456**, 237-243, 2015.
- [104] L. Zhu, A. Raman, and S. Fan, “Color-preserving daytime radiative cooling,” *Appl. Phys. Lett.* **103**, 223902, 2013.
- [105] E. Rephaeli, A. Raman, and S. Fan, “Ultrabroadband photonic structures to achieve high-performance daytime radiative cooling,” *Nano Lett.* **13**, 1457–1461, 2013.
- [106] A. Saito, Y. Ishikawa, Y. Miyamura, M. Akai-Kasaya, and Y. Kuwahara, “Optimization of reproduced morpho blue coloration,” *Proc. SPIE* **6767**, 676706, 2007.
- [107] M. Asano, T. Kuroda, S. Shimizu, A. Sakihara, K. Kumazawa, and H. Tabata, “Morphotex fiber,” Patent No.US6326094, 2001.

- [108] R. A. Potyrailo, H. Ghiradella, A. Vertiatchick, K. Dovidenko, J. R. Cournoyer, and E. Olson, “Morpho butterfly wing scales demonstrate highly selective vapor response,” *Nature Photonics* 1, 123–128, 2007.
- [109] A. D. Pris, Y. Utturkar, C. Surman, W. G. Morris, A. Vert, S. Zalyubovskiy, T. Deng, H. T. Ghiradella, and R. A. Potyrailo, “Towards high-speed imaging of infrared photons with bio-inspired nanoarchitectures,” *Nature Photonics* 6, 195–200, 2012.
- [110] S. Lou, X. Guo, T. Fan, and D. Zhang, “Butterflies: inspiration for solar cells and sunlight water-splitting catalysts,” *Energy Environ. Sci.* 5, 91–95, 2012.
- [111] B. D. Heilman and I. N. Miaoulis, “Insect thin films as solar collectors,” *Appl. Opt.* 33, 6642–6647, 1994.
- [112] W. Zhang, D. Zhang, T. Fan, and J. Gu, “Novel photoanode structure templated from butterfly wing scales,” *Chem. Mater.* 21, 33–40, 2009.

# CURRICULUM VITAE

## Azadeh Didari

### PERSONAL INFORMATION

**Address:** Center for Energy, Environment and Economy (CEEE),  
Ozyegin University-Çekmeköy Campus  
Nişantepe District, Orman Street, 34794  
Çekmeköy – Istanbul- Turkey

**Email:** Azadeh.didari@gmail.com

### **Languages:**

- Persian (Farsi): Native Language
- English : Fluent (IELTS overall score: 7)
- Turkish (Fair)
- Greek (Elementary)

**Nationality:** Iranian

### EDUCATION

**2011-2016:** Ozyegin University, Istanbul, Turkey  
PhD: Doctorate of Philosophy in Electrical and Electronic Engineering  
Advisor: Prof. M. Pinar Mengüç

**2008-2010:** Eastern Mediterranean University, Famagusta, Northern Cyprus  
MSc: Master of Science in Electrical and Electronic Engineering  
Advisor: Assist.Prof. Rasime Uyguroğlu

**2005-2008:** Eastern Mediterranean University, Famagusta, Northern Cyprus  
BSc: Bachelor of Science in Electrical and Electronic Engineering  
Advisor: Assist.Prof. Rasime Uyguroğlu

### EMPLOYMENT

**August 2011-Present** Research assistant in Center for Energy, Environment and Economy (CEEE), Ozyegin University, Istanbul, Turkey

**Jan 2011-June 2016** Teaching assistant at Electrical and Electronic Engineering Department, Ozyegin University, Istanbul, Turkey

- Calculus I
- Calculus II
- Applied statistics
- Digital systems
- Circuit analysis
- Linear algebra
- Electromagnetic theory I

**Oct 2009-June 2010** Eastern Mediterranean University, Famagusta, N. Cyprus  
Faculty of Engineering  
Alumni of Graduate Students' Assistant

**Oct 2008- Oct 2009** Eastern Mediterranean University, Famagusta, N. Cyprus  
Electrical and Electronic Engineering Department  
Teaching Assistant:

- Fundamental of Electrical Engineering
- Physical Electronics
- Computational Methods in Electrodynamics

**Summer 2007** Eastern Mediterranean University, Famagusta, N. Cyprus  
Internship: Computer Center Department

- I cooperated with System Support and Networking Groups.
- Gained experience in system configuration and IP properties.
- Installation of proxy systems and their applications and requirements.

**Sep 2006-Jun 2007** Eastern Mediterranean University, Famagusta, N. Cyprus  
Electrical and Electronic Engineering Department  
Electronic Simulation Laboratories  
Student Assistant

### **SCHOLARSHIPS AND AWARDS**

- Ozyegin University fellowship and Tuition scholarship, PhD program, 2011-Present
- Eastern Mediterranean University fellowship and Tuition scholarship, M.Sc. program, 2008-2010.

## **PUBLICATIONS**

### **JOURNALS (IN PREPARATION)**

- A. Didari and M. P. Mengüç, “Spectrally selective thermal emission by structured SiC-BN mesoporous metamaterials,” *to be submitted to journal of Optics Express*, June 2016.
- A. Didari and M. P. Mengüç, “Biologically inspired structures for near-field radiative transfer applications,” *to be submitted to journal of Nano Letters*, July 2016.
- A. Didari and M. P. Mengüç, “A Design Tool for Near-Field Radiative Transfer: The Developmental Steps of The NF-RT-FDTD Code,” *Journal of Quantitative Spectroscopy and Radiative Transfer*, September 2016

### **JOURNALS (PUBLISHED)**

- A. Didari and M. P. Mengüç, “Near-field thermal radiation transport by mesoporous metamaterials,” *Optics Express*, **23**(19), A1253-A1258, 2015.
- A. Didari and M. P. Mengüç, “Near to Far-Field Coherent Thermal Emission by Surfaces Coated by Nanoparticles: Evaluation of Effective Medium Theory,” *Optics Express* **23**, (11), A547-A552, 2015.
- A. Didari and M. P. Mengüç, “Near-Field Thermal Emission between Structured Surfaces separated by NanoGaps,” *Journal of Quantitative Spectroscopy and Radiative Transfer*, **158**, 43-51, 2015.
- A. Didari and M. P. Mengüç, “Analysis of Near-Field Radiation Transfer within Nano-Gaps Using FDTD Method,” *Journal of Quantitative Spectroscopy and Radiative Transfer*, **146**, 214-226, 2014.

### **CONFERENCE PAPERS**

- A. Didari and M. P. Mengüç, “A Design Tool for Near-Field Radiative Transfer: The Developmental Steps of The NF-RT-FDTD Code,” *Proceedings of the 8th International Symposium on Radiative Transfer*, RAD-16, Cappadocia, Turkey, June 6-10, 2016 (Paper).
- T. Okutucu-Özyurt, E. B. Elçioğlu , R. Denker , A. Didari and M. Pinar Mengüç, “Towards Nano-Scale Thermophotovoltaic Applications: Discussions for Material Selection and Measuring System” *Proceedings of the 8th International Symposium on Radiative Transfer*, RAD-16, Cappadocia, Turkey, June 6-10, 2016 (Paper).

- A. Didari and M. P. Mengüç, “Far-field thermal emission by metamaterials with nano-scale porosities and corrugations,” *Optics for Solar Energy (OSA)*, Suzhou, China, Nov 2-5, 2015(Paper).
- E. B. Elçioğlu, R. Denker, A. Didari, T. Okutucu-Özyurt, M. P. Mengüç, "Review of Near Field Thermal Radiation Harvesting Studies in Thermophotovoltaic Systems," in Proceedings of the 20th National Thermal Science and Technology Congress, Balıkesir, September 2-5, 2015, paper 2015-270.
- A. Didari and M. P. Mengüç, “Impact of Nanostructures on Near-Field Radiative Heat Transfer: Modeling by Finite Difference Time Domain Method,” *CHT-15, 6th International Symposium on Advances in Computational Heat Transfer*, Piscataway, USA, May 25-29, 2015 (Paper).
- A. Didari and M. P. Mengüç, “Near to Far-Field Thermal Emission by Nanoparticles on a Substrate: Evaluation of Effective Medium Theory,” *Optics for Solar Energy (OSA)*, Canberra, Australia, Dec 2-5, 2014 (Paper).
- A. Didari and M. P. Mengüç, “Near-Field Thermal Emission between Corrugated Surfaces separated by Nano-Gaps,” *Nanoscale and Microscale Heat Transfer IV (Eurotherm 103)*, Lyon, France, October 15-17, 2014 (Extended Abstract).
- A. Didari and M. P. Mengüç, “Effect of Nanoparticles to Near-Field Thermal Emission Calculations by FDTD Method,” *2<sup>nd</sup> International workshop on Nano and Micro Thermal radiation (NanoRad14)*, Shanghai, China, June 6-9, 2014 (Extended Abstract).
- A. Didari and M. P. Mengüç, “Finite Difference Time Domain Method for Analysis of Near Field-Emission within Nano-Gaps,” *14th Electromagnetic and Light Scattering Conference (ELS-XIV)*, Lille, France, June 17-21, 2013 (Abstract).
- A. Didari and M. P. Mengüç, “Analysis of Near-Field Emission within Nano-Gaps Using Finite Difference Time Domain Method,” *Seventh International Symposium on Radiative Transfer (RAD-13)*, Kusadasi, Turkey, June 2-8, 2013 (Paper).
- A. Didari and R. Uyguruglu, "Analysis of Multilayer Microstrip Structures by Using FDTD":*6<sup>th</sup> EEECS'10 International Symposium*, Lefke, N. Cyprus, 2010 (Paper).

### **ORAL AND POSTER PRESENTATIONS**

- A. Didari, M. P. Mengüç, “Near-to Far-Field Emission Characteristics of Mesoporous Metamaterials,” *WE-Heraeus-Seminar: Heat transfer and heat conduction on the nanoscale*, Bad honnef, Germany, April 10-15, 2016 (Poster).

- A. Didari, M. P. Mengüç, “Near-Field Thermal Radiation between Nano-Gaps,” *The Nanotechnology in Manufacturing Workshop*, Istanbul, Turkey, Oct 15-17, 2014 (Oral presentation).
- A. Didari, M. P. Mengüç, “Analysis of Near-Field Emission Within Nano-Gaps Using Finite Difference Time Domain Method,” *Electromagnetic and Light Scattering Conference XIV*, Lille, France, June 17-June 21, 2013 (Poster).
- A. Didari, M. P. Mengüç, “Analysis of Near-Field Emission Within Nano-Gaps Using Finite Difference Time Domain Method,” *RAD 13: Seventh International Symposium on Radiative Transfer*, Kusadasi, Turkey, June 2-June 8, 2013 (Oral presentation).
- A. Didari, M. P. Mengüç, “Analysis of Near-Field Emission Within Nano-Gaps Using Finite Difference Time Domain Method,” *Nanoscale Radiative Heat Transfer School, Physics school Les Houches*, France, May 11-May 17, 2013 (Poster).
- A. Didari, M. P. Mengüç, “Analysis of Near-Field Emission Within Nano-Gaps Using Finite Difference Time Domain Method,” *20<sup>th</sup> European Doctoral School on Metamaterials*, Louvain-La-neuve, Belgium, May 7-May 12, 2012 (Oral presentation).

#### **WORKSHOPS ATTENDED**

- WE-Heraeus-Seminar: Heat transfer and heat conduction on the nanoscale, Bad Honnef, Germany, April 10-15, 2016
- Bremen Workshop on Light Scattering, Bremen, Germany, March 2-3, 2015
- Nano-Micro Heat Transfer Course, Istanbul, Turkey, July 7-1, 2014
- Nanoscale Radiative Heat Transfer Physics School, Les Houches, France, May 12-17, 2013
- EUROMETA 20th European Doctoral School on Metamaterials, Louvain-la-Neuve, Belgium, May 7-11, 2012